

**UNCERTAINTY QUANTIFICATION IN PARTICLE IMAGE
VELOCIMETRY**

by

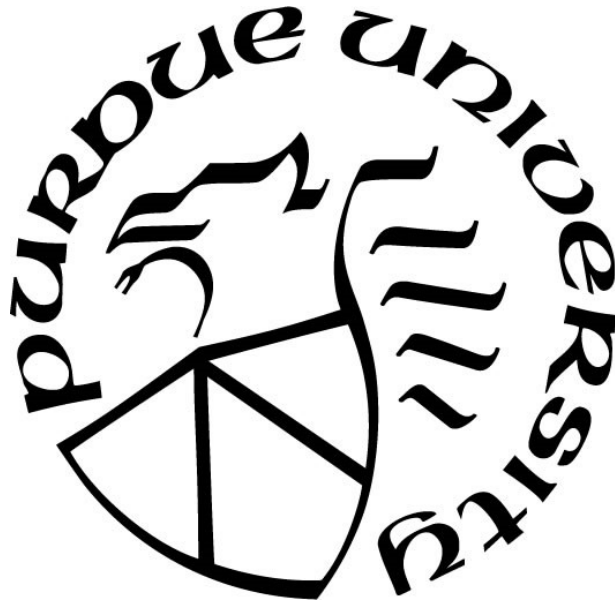
Sayantana Bhattacharya

A Dissertation

Submitted to the Faculty of Purdue University

In Partial Fulfillment of the Requirements for the degree of

Doctor of Philosophy



School of Mechanical Engineering

West Lafayette, Indiana

December 2019

**THE PURDUE UNIVERSITY GRADUATE SCHOOL
STATEMENT OF COMMITTEE APPROVAL**

Dr. Pavlos P. Vlachos, Chair

School of Mechanical Engineering

Dr. Steven T. Wereley

School of Mechanical Engineering

Dr. Charles A. Bouman

School of Electrical and Computer Engineering

Dr. Carson Slabaugh

School of Aeronautics and Astronautics

Approved by:

Dr. Nicole Key

Dedicated to my parents Pritish and Shipra Bhattacharya.

ACKNOWLEDGMENTS

I want to thank my professors, my family, relatives and my friends for their support and positive influence, throughout the journey of my PhD. Firstly, I want to thank my major Professor Pavlos Vlachos for providing me the opportunity to do research with him, for his invaluable guidance and patience, for imparting the wisdom to ask the right questions, and most importantly for his trust and belief in me. I want to thank all my committee members for their help and support, namely, Prof. Steven Wereley for his introductory course in PIV and his strong support during my early days of PhD, Prof. Charles Bouman for the discussions and interactions during the “model-based image processing” course and Prof. Carson Slabaugh, for the insightful discussions during our collaborative meetings.

I want to thank and acknowledge the support of my coauthors, Dr. John Charonko, for his valuable suggestions, feedback and discussions on the topic of PIV uncertainty and Dr. Aaron Boomsma for working with me on the collaborative uncertainty project. I want to thank and appreciate all my lab members, for the professional lab environment, critical feedbacks and cheerful discussions. I want to thank Prof. Vlachos also for the amazing synergy between the different projects and the lab members, making it a productive environment for research.

Finally, I want to thank my friends here at Purdue and elsewhere, for their constant support over the years. Especially, I want to thank Anushila, Sreyashi, Sayan, Aditi, Subhajit, Bigyan, Arindam, Indrani, Prabudhya, Sanchari, Aritra, Sreya, Asesh, Krishnakali, Somrita, Satarupa, Sayan, Esha and my cousins Sukanya, Anusua, Sulogna and Saikat for their unparalleled support, motivation and well wishes. My parents have been the strongest supporter in my journey of pursuing my goals in life. Their love and sacrifice have been the pillar of my success. Lastly, I want to thank and appreciate all the staffs and members of the graduate program in the School of Mechanical Engineering, Purdue University, for giving me this opportunity and for taking care of the administrative responsibilities in a helpful and convenient way.

TABLE OF CONTENTS

LIST OF TABLES.....	8
LIST OF FIGURES	10
ABSTRACT.....	14
1. A COMPARATIVE EXPERIMENTAL EVALUATION OF UNCERTAINTY ESTIMATION METHODS FOR TWO-COMPONENT PIV	17
Abstract.....	17
1.1 Introduction.....	18
1.1.1 Direct Uncertainty Quantification Methods	18
1.1.2 Indirect Uncertainty Quantification Methods.....	19
1.2 Experimental Test Cases, Procedures and Methodologies	20
1.2.1 Cylinder in Cross Flow.....	21
1.2.2 Circular Jet in Quiescent Flow	23
1.2.3 PIV Processing Algorithms	25
1.2.4 Uncertainty Propagation from Reference Solution.....	27
1.2.5 Error Distributions for Low Resolution Measurements	28
1.3 Results & Discussion	29
1.3.1 Low Resolution PIV Uncertainty Quantification	30
1.3.1.1 Contours of Expected and Predicted Uncertainty.....	30
1.3.1.2 Error Uncertainty Histograms	31
1.3.1.3 Expected and Predicted Uncertainties Across a Plane	35
1.3.1.4 Standard Coverages	38
1.4 Discussion and Conclusions	39
1.5 References.....	42
Appendix A.....	44
Appendix B.....	50
2. PARTICLE IMAGE VELOCIMETRY (PIV) UNCERTAINTY QUANTIFICATION USING MOMENT OF CORRELATION (MC) PLANE	52
Abstract.....	52
2.1 Introduction.....	54

2.1.1	Indirect methods	54
2.1.2	Direct methods.....	55
2.2	Methodology.....	57
2.2.1	Definition of uncertainty.....	58
2.2.2	Statistics of PIV correlation plane and uncertainty	58
2.2.3	Moment of Correlation (MC) Algorithm.....	61
2.3	Results.....	65
2.3.1	Variation with elemental error sources.....	65
2.3.2	Evaluation for complex flow fields (simulated and experimental test cases)	67
2.3.2.1	Error and uncertainty histogram	68
2.3.2.2	Predicted vs expected uncertainty	72
2.3.2.3	Spatial variation in RMS error and uncertainty.....	74
2.3.2.4	Uncertainty coverage.....	76
2.4	Conclusion	77
2.5	References.....	79
3.	STEREO-PARTICLE IMAGE VELOCIMETRY UNCERTAINTY QUANTIFICATION	81
	Abstract	81
3.1	Introduction.....	83
3.2	Methodology.....	86
3.2.1	Uncertainty in physical coordinate system	88
3.2.2	Uncertainty in triangulated \mathbf{z} -plane location	89
3.2.3	Uncertainty in mapping function coefficients	90
3.2.4	Uncertainty in stereo angles.....	92
3.2.5	Uncertainty in dewarped camera image cross correlation.....	93
3.2.6	Uncertainty propagation in stereo reconstruction.....	93
3.3	Sensitivity Analysis	95
3.4	Results.....	98
3.4.1	Uncertainty estimation for synthetic flow case	98
3.4.2	Uncertainty estimation for the experimental vortex ring flow case	103
3.5	Conclusion	110
3.6	References.....	112

Appendix A.....	115
4. VOLUMETRIC PARTICLE TRACKING VELOCIMETRY (PTV) UNCERTAINTY QUANTIFICATION.....	117
Abstract.....	117
4.1 Introduction.....	119
4.2 Methodology.....	121
4.2.1 Error propagation through the mapping function.....	122
4.2.2 Estimating uncertainty in particle image location.....	124
4.2.3 Estimating the uncertainty in mapping function coefficients.....	126
4.2.4 Uncertainty propagation in reconstructed positions.....	127
4.2.5 Uncertainty in estimated velocity field.....	128
4.3 Results.....	129
4.3.1 Comparing error and uncertainty histogram for reconstructed particle positions ...	129
4.3.2 Reconstructed position uncertainty for varying particle concentration.....	131
4.3.3 Uncertainty prediction for tracked velocity vectors.....	133
4.3.4 Experimental Validation: Uncertainty prediction for laminar pipe flow.....	135
4.4 Conclusion.....	137
4.5 References.....	139
5. A NEW PARTICLE IMAGE VELOCIMETRY TECHNIQUE FOR TURBOMACHINERY APPLICATIONS.....	142
Abstract.....	142
5.1 Introduction.....	144
5.2 Experimental Setup.....	144
5.3 PIV vector processing.....	147
5.4 Results.....	148
5.5 Conclusion.....	150
5.6 References.....	152
6. CONCLUSION.....	154

LIST OF TABLES

Table 1.1. Cylinder in cross flow experimental apparatus parameters.	22
Table 1.2. Jet flow experimental apparatus parameters.	24
Table 1.3. Processing parameters (number of passes, window sizes, and overlap) for each processing code.	26
Table 1.4. RMS of the magnitude error (pix) for each case and processing code comparing the HR and LR measurements.	28
Table 1.5. Comparing the mean, standard deviation and RMS of the error distributions for both X and Y components to the RMS of IM and CS uncertainty estimates. The values for all three experiments are mentioned in the table. All units are in pixels.	34
Table 1.6. Mean and RMS signal comparisons between the high resolution and LDV measurements as calculated by each processing code for the jet experiment.	46
Table 1.7. RMS absolute error, RMS relative error, and cross-correlation coefficient between high resolution and LDV measurements as calculated by each processing code for the jet experiment.	46
Table 1.8. Mean displacement, RMS absolute error, and cross-correlation coefficient between high resolution and LDV measurements as calculated by each processing code for the cylinder in cross flow experiments.	49
Table 1.9. Variation of RMS error and uncertainties in the jet flow case for PRANA and DaVis processing.	50
Table 1.10. Variation of RMS error and uncertainties in the cylinder flow case (Red = 480) for PRANA and DaVis processing.	50
Table 1.11. Variation of RMS error and uncertainties in the jet and the cylinder flow case (Red = 480) for Insight4G processing.	51
Table 2.1: Description of test cases and processing parameters.	68
Table 2.2. Comparing the RMS error and uncertainty values across different methods for the five test cases.	72
Table 3.1. Expressions for Sensitivity coefficients as a function of stereo angles for stereo uncertainty propagation equations.	95
Table 3.2. RMS of the total error, uncertainty and standard coverage for uniform flow case, with and without self-calibration.	101
Table 3.3. RMS error, uncertainty and standard coverage for vortex ring case with IM and CS methods for planar uncertainty estimation.	106

Table 3.4. Sensitivity coefficients for ν component uncertainty propagation for large stereo angles.	116
Table 4.1. Comparison of RMS error and RMS uncertainty values for the triangulation and IPR based reconstructed particle positions for a range of seeding densities.....	132
Table 4.2. Comparison of RMS error and RMS uncertainty values for the particle tracking displacement estimates using triangulation and IPR based reconstructed particle positions for a range of seeding densities.	134

LIST OF FIGURES

Figure 1.1. a) Experimental setup for the cylinder in cross flow cases. b) Side view photo with reference PIV system in the background. c) Time averaged contours and vectors of particle displacement for both low and high resolution PIV systems for the cylinder in cross flow (**Red = 480**) case. Measurements within the black box are those from the high resolution system. The LDV measurement location is at $X/d=0, Y/d=0$ 22

Figure 1.2. a) Experimental apparatus of the velocity measurement systems. b) Side view photo with the measurement system camera in the background. c) Time averaged contours and vectors of particle displacement for both low and high resolution PIV systems for the jet flow case. Measurements within the black box are those from the high resolution system. The LDV measurement location is at $x/d=0, y/d=0$ 24

Figure 1.3. Instantaneous measurements (from Insight4G) of streamwise velocity from high and low resolution PIV systems and an LDV system. a) Jet experiment. b) Cylinder wake **Red = 480**. c) Cylinder wake **Red = 730**. 27

Figure 1.4. Error magnitude distributions for low resolution measurements. a) Jet experiment. b) Cylinder wake **Red = 480**. c) Cylinder wake **Red = 730**. 29

Figure 1.5. Error and uncertainty spatial contours for each method for the a) jet and b) wake flow experiment (**Red = 730**). 31

Figure 1.6. Error and uncertainty distributions for each uncertainty method for the jet experiment. a) PPR and MI distributions from PRANA. b) PPR distributions from Insight4G. c) IM distributions from PRANA. d) CS distributions from DaVis. 32

Figure 1.7. Error and uncertainty distributions for each uncertainty method for the both cylinder in cross flow experiments (a-d for **Red = 480** and e-h for **Red = 730**). 33

Figure 1.8. RMS error and uncertainty profiles along the spanwise direction across the jet flow. 36

Figure 1.9. RMS error and uncertainty profiles across the wake of the cylinder in cross flow for **Red = 480**. 37

Figure 1.10. Standard coverages for each experiment, where the dashed line denotes the ideal standard coverage of 68.5%. 39

Figure 1.11. a) Inverted high resolution frame without filter showing LDV cross-beams. b) Inverted high resolution frame with filter. 45

Figure 1.12. Representative time history comparison of streamwise velocity between the high resolution PIV and LDV systems for the jet experiment. 46

Figure 1.13. Error distributions between the reference PIV and LDV. 47

Figure 1.14. Representative time history comparisons of streamwise velocity between the high resolution PIV and LDV systems for both cylinder in cross flow experiments. a) Red = 480 . b) Red = 730	48
Figure 1.15. Error distributions between the reference PIV and LDV. a) Red = 480 . b) Red = 730	49
Figure 2.1. Extracting PDF of displacement from PIV image pair cross correlation.	60
Figure 2.2. Algorithm to find standard uncertainty from PDF of displacements.	61
Figure 2.3. Sensitivity of MC method to primary PIV error sources for three different window resolutions (24, 32 and 64).....	66
Figure 2.4. Error and uncertainty histogram comparing MC, IM and CS performance for the five test cases.....	70
Figure 2.5. Comparing RMS error versus RMS of the predicted uncertainty for each method (MC, IM and CS) for the five test cases.	73
Figure 2.6. Comparing the spatial variation in RMS error and the RMS of the estimated uncertainties using MC, IM and CS methods for the different test cases. Column 1: WS1 processing, Column 2: WS2 processing and Column 3: Mean velocity magnitude contours with a dashed line indicating the slice from which the spatial profile is extracted.	75
Figure 2.7. Grouped bar chart for standard uncertainty coverage using MC, IM and CS methods for WS1 and WS2 processing. a) for different flow test cases, b) for all cases combined. The target coverages calculated from the true error distributions are shown as black squares for each case.	77
Figure 3.1. Stereo PIV measurement chain	84
Figure 3.2. Uncertainty propagation flow chart for a stereo-PIV measurement process: (a, b, and c) correspond to how to estimate the uncertainty in physical coordinate system (d and e refer to the uncertainty in triangulated \mathbf{z} location, and (f, g) correspond to the uncertainty in the mapping function coefficients respectively. (h, i) correspond to the uncertainties in the angles and the planar uncertainty for individual camera dewarped images. Finally, the planar uncertainties and angle uncertainties combined to obtain the uncertainty of all three velocity components (j).	87
Figure 3.3. Contour maps of sensitivity coefficients and reconstructed velocity uncertainties as a function of stereo angles are shown for a) u , b) w and c) v components.	97
Figure 3.4. Error and uncertainty histograms for u , v and w components in synthetic uniform flow case with self-calibration.	100
Figure 3.5. Contribution of planar and angle uncertainty to overall stereo field uncertainty for uniform flow case in presence of disparity. Subplots a), b) and c) show the uncertainty histograms for u , w and v components for 1mm laser sheet case. Subplots d) and e) show contribution fraction of different uncertainty components for 1mm and 3mm thick laser sheet cases respectively....	102

Figure 3.6. Schematic of experimental vortex ring set-up. Cam1 is in center and hence shown in dotted line. Cam2 and Cam4 are in horizontal plane with Scheimpflug adapter. Cam3 and Cam5 are in vertical plane without Scheimpflug adapter.	104
Figure 3.7. Vortex ring stereo velocity field error and uncertainty histogram for different camera orientation (Cam1Cam3: Top and Cam2Cam4: Bottom) using CS method for planar uncertainty estimation.	105
Figure 3.8. Planar uncertainty RMS contours for each camera components are shown in a) for IM and b) for CS methods. The RMS error and uncertainty spatial contours for stereo components are shown in c) and d) for IM and CS methods respectively.	107
Figure 3.9. Comparison of RMS error and uncertainty temporal distributions for the vortex ring case. The left column plots are for IM method and right column plots are for CS method. Top row and bottom row subplots correspond to Cam1Cam3 and Cam2Cam4 camera orientations respectively.	109
Figure 3.10. Schematic of stereo PIV camera set up for large camera angles.	115
Figure 4.1. A volumetric PTV measurement chain showing the main steps in the process.	120
Figure 4.2. A schematic showing different steps (a – e) for estimating elemental uncertainties in particle image location X and calibration coefficients a_i and its propagation to the uncertainty in the world coordinate xw	124
Figure 4.3. Histogram of error (e) and uncertainty (σ) distributions for reconstructed particle positions (xw, yw, zw) for the synthetic vortex ring case with 0.05ppp particle concentration for a) triangulation and b) IPR reconstructions. The vertical lines indicate the RMS value for each distribution.	130
Figure 4.4. Comparison of triangulation and IPR reconstructed position error and uncertainty as a function of seeding density for the synthetic vortex ring case. Plot a) compares the RMS error and RMS of predicted uncertainties for seeding densities in the range of 0.01ppp to 0.1ppp and plot b) compares the coverage in each case.	131
Figure 4.5. Error and uncertainty histogram comparison for tracked velocity vectors in the synthetic vortex ring case with seeding density of 0.05ppp for a) triangulation based reconstruction and for b) IPR based reconstruction.	134
Figure 4.6. Schematic of laminar pipe flow set up showing the flow loop and camera arrangement.	135
Figure 4.7. The mean streamwise velocity profile for a 3D PTV measurement of a laminar pipe flow is shown in a). The velocity profile is compared with the true solution in b). The error and estimated uncertainty histogram are shown for triangulation-based reconstruction in c) and for IPR based reconstruction in d).	136
Figure 5.1. (a) Schematic of PIV setup with window, camera and laser positions, (b) Schematic showing flow direction, phase-locked measurement planes covering the blade passage and the expected tip leakage flow.	145
Figure 5.2. Schematic of flow seeding method.	147

Figure 5.3. Volume slices of normalized radial velocity at fixed spanwise locations for stereo reconstructed velocity field..... 149

Figure 5.4. Comparison of PIV results with over-rotor static pressures. Flow is from left to right. (a) Contours of normalized radial velocity near the wall; (b) Over-rotor static pressure contours; (c) Both methods superimposed with PIV normalized radial velocities as colored contours and static pressure contours represented as lines..... 150

ABSTRACT

Particle Image Velocimetry (PIV) is a non-invasive measurement technique which resolves the flow velocity by taking instantaneous snapshots of tracer particle motion in the flow and uses digital image cross-correlation to estimate the particle shift up to subpixel accuracy. The measurement chain incorporates numerous sets of parameters, such as the particle displacements, the particle image size, the flow shear rate, the out-of-plane motion for planar PIV and image noise to name a few, and these parameters are interrelated and influence the final velocity estimate in a complicated way. In the last few decades, PIV has become widely popular by virtue of developments in both the hardware capabilities and correlation algorithms, especially with the scope of 3-component (3C) and 3-dimensional (3D) velocity measurements using stereo-PIV and tomographic-PIV techniques, respectively. The velocity field measurement not only leads to other quantities of interest such as Pressure, Reynold stresses, vorticity or even diffusion coefficient, but also provides a reference field for validating numerical simulations of complex flows. However, such a comparison with CFD or applicability of the measurement to industrial design requires one to quantify the uncertainty in the PIV estimated velocity field. Even though the PIV community had a strong impetus in minimizing the measurement error over the years, the problem of uncertainty estimation in local instantaneous PIV velocity vectors have been rather unnoticed. A typical norm had been to assign an uncertainty of 0.1 pixels for the whole field irrespective of local flow features and any variation in measurement noise. The first article on this subject was published in 2012 and since then there has been a concentrated effort to address this gap. The current dissertation is motivated by such a requirement and aims to compare the existing 2D PIV uncertainty methods, propose a new method to directly estimate the planar PIV uncertainty from the correlation plane and subsequently propose the first comprehensive methods to quantify the measurement uncertainty in stereo-PIV and 3D Particle Tracking Velocimetry (PTV) measurements.

The uncertainty quantification in a PIV measurement is, however, non-trivial due to the presence of multitude of error sources and their non-linear coupling through the measurement chain transfer function. In addition, the advanced algorithms apply iterative correction process to minimize the residual which increases the complexity of the process and hence, a simple data-reduction equation for uncertainty propagation does not exist. Furthermore, the calibration or a

reconstruction process in a stereo or volumetric measurement makes the uncertainty estimation more challenging. Thus, current uncertainty quantification methods develop a-posterior models utilizing the evaluated displacement information and combine it with either image information, correlation plane information or even calibration “disparity map” information to find the desired uncertainties in the velocity estimates.

The first chapter evaluates the existing 2D PIV uncertainty models prior to the ones developed in this dissertation work. The performance of four different methods (Peak to Peak Ratio (PPR), Mutual Information (MI), Image Matching (IM) and Correlation Statistics (CS)) were evaluated for two experimental cases of a cylinder wake and a free jet flow and the prescribed uncertainty was compared against the expected uncertainty or RMS error. The ground truth was established by a high magnification PIV measurement, which in turn was validated against a high frequency LDV measurement. The results indicated that the PPR and MI methods were less sensitive to the RMS error while the IM and CS methods, although had a better response to the variation in RMS error, underpredicted the uncertainty level. This work highlighted the need for further development in the field of planar PIV uncertainty estimation.

The second chapter proposes a novel method to estimate the 2D PIV uncertainty directly from the cross-correlation plane. PIV being a statistical estimate, the evaluated displacement from the cross-correlation peak represents the most probable displacement for the interrogation window. However, individual particles contributing to the correlation peak do not shift by the exact same amount, due to measurement noise and thus the PDF of displacement can be obtained by extracting the phase information from the correlation plane. This idea is used to estimate the standard deviation of the PDF or the standard uncertainty. This method, namely Moment of Correlation (MC), showed a strong sensitivity to the primary error sources in PIV, as well as an improved uncertainty coverage, especially for window resolution of 64 pixels and above, for a wide range of flow fields. However, for synthetic images with very low image noise and for smaller interrogation windows the predicted uncertainty incurred a bias, of the order of 0.02 pixels, due to the resolution limit in estimating the PDF standard deviation.

The next chapter develops the first method to quantify the uncertainty in a stereo-PIV measurement. The uncertainty propagation through the measurement chain involves combining the individual camera planar uncertainty estimates with the uncertainty in the camera angles or rather uncertainty in the camera calibration function. A methodology was developed to estimate

the calibration coefficient uncertainty from the uncertainty in stereo-camera registration or “disparity” and subsequently its propagation through the self-calibration process chain. The results for the 3-component uncertainty showed a strong dependence on the individual camera 2D uncertainty estimates. However, a higher disparity can lead to a higher contribution from the uncertainty in the stereo angles. The sensitivity of the coefficients for the uncertainty propagation equation were also analyzed as a function of the camera angles. Finally, the results were successfully validated for synthetic images as well as for an experimental vortex ring case.

The fourth chapter shifts the focus to volumetric PTV measurements, as such measurements have become increasingly popular over the last few years, especially with the development of highly accurate Shake-The-Box (STB) method. The 3D PTV, although relies on tracking, has some commonalities with stereo-PIV measurement in terms of the calibration process. Here, the experience with stereo-calibration uncertainty was utilized to estimate the error propagation through the calibration mapping function for the 3D reconstruction process. The proposed reconstruction uncertainty model showed a one-to-one correspondence with the reconstructed 3D particle position RMS error for a range of seeding densities. The reconstruction uncertainty directly influenced the uncertainty in the tracked velocity vector. A synthetic vortex-ring case and an experimental laminar pipe flow case were tested using the proposed framework and the results showed a reliable uncertainty prediction for the 3D PTV velocity fields in both cases.

The final chapter is a new experimental method demonstration for PIV in the rotor stage of a multistage axial compressor. This chapter is not related to the uncertainty quantification methodology, the primary topic of this dissertation. In this analysis, instead of using traditional probe traversing techniques and using a periscopic probe for illumination, a new 3D PIV method was proposed with line-of-sight illumination. The time-averaged measurements revealed a region of negative radial velocities which matched with the static-pressure unsteadiness region, indicating tip-leakage vortex region. However, this analysis highlights the necessity of uncertainty bounds in a PIV measurement for precise comparison with measurements using other modalities.

Hence, this dissertation establishes a comprehensive analysis of Particle Image Velocimetry measurement uncertainty spanning across planar PIV, stereo-PIV and 3D PTV.

1. A COMPARATIVE EXPERIMENTAL EVALUATION OF UNCERTAINTY ESTIMATION METHODS FOR TWO-COMPONENT PIV

Aaron Boomsma^{1*}, Sayantan Bhattacharya^{2*}, Dan Troolin¹, Stamatios Pothos¹ and Pavlos Vlachos²

¹ Fluid Mechanics Research Instruments, TSI Incorporated, Shoreview, MN, USA.

² School of Mechanical Engineering, Purdue University, West Lafayette, Indiana, USA.

**A. Boomsma & S. Bhattacharya contributed equally to this work.*

This chapter has been previously published in Measurement Science and Technology, 27 094006.

DOI: <https://doi.org/10.1088/0957-0233/27/9/094006>

Abstract

Uncertainty quantification in planar Particle Image Velocimetry (PIV) measurement is critical for proper assessment of the quality and significance of reported results. New uncertainty estimation methods have been recently introduced generating interest about their applicability and utility. The present study compares and contrasts current methods, across two separate experiments and three software packages in order to provide a diversified assessment of the methods. We evaluated the performance of four uncertainty estimation methods, Primary Peak Ratio (PPR), Mutual Information (MI), Image Matching (IM) and Correlation Statistics (CS). The PPR method was implemented and tested in two processing codes, using in-house open source PIV processing software (PRANA, Purdue University) and Insight4G (TSI, Inc). The MI method was evaluated in PRANA, as was the IM method. The CS method was evaluated using DaVis (LaVision, GmbH). Utilizing two PIV systems for high and low-resolution measurements and a Laser Doppler Velocimetry (LDV) system, data were acquired in a total of three cases: a jet flow and a cylinder in cross flow at two Reynolds numbers. LDV measurements were used to establish a point validation against which the high-resolution PIV measurements were validated. Subsequently, the high-resolution PIV measurements were used as a reference against which the low-resolution PIV

data were assessed for error and uncertainty. We compared error and uncertainty distributions, spatially varying RMS error and RMS uncertainty, and standard uncertainty coverages. We observed that qualitatively, each method responded to spatially varying error (i.e., higher error regions resulted in higher uncertainty predictions in that region). However, the PPR and MI methods demonstrated reduced uncertainty dynamic range response. In contrast, the IM and CS methods showed better response, but under-predicted the uncertainty ranges. The standard coverages (68% confidence interval) ranged from approximately 65%-77% for PPR and MI methods, 40%-50% for IM and near 50% for CS. These observations illustrate some of the strengths and weaknesses of the methods considered herein and identify future directions for development and improvement.

1.1 Introduction

Although the sources of PIV measurement error are well characterized [1], [2], quantifying their corresponding uncertainty bounds continues to be a challenge. This is, in part, due to the high number of sources of error and their interactions. Measurement errors include calibration error, background noise, particle response, non-uniform illumination, strong velocity gradients within windows, peak detection scheme, peak locking, just to name a few. Each of these sources of error can manifest itself as a random or systematic error.

There have been a number of PIV uncertainty quantification methods published, including Uncertainty Surface (US) [3], Primary Peak Ratio (PPR) [4], [5], Mutual Information (MI) [6], Image Matching (IM) [7], and Correlation Statistics (CS) [8]. These methods can be classified into two categories: direct and indirect. Direct methods estimate uncertainty by matching particle images through window shifting. Indirect methods estimate uncertainty through a software-specific calibration of a correlation between the measurement error and either an uncertainty source or a property of the correlation plane. Below, we briefly describe each approach.

1.1.1 Direct Uncertainty Quantification Methods

Image matching (IM) [7] is a direct method that calculates PIV measurement uncertainties by matching individual particle images from a given interrogation window of the correlating image pairs. Particle matching is achieved by continuously shifting the window by the local calculated

displacement vector. For particles that are matched, any spatial disparity between them is recorded as a vector. Using the statistics of the ensemble of the matched particle disparity vectors the uncertainty can be calculated. The correlation statistics (CS) [8] extends the particle matching by matching all the pixel intensities in the correlating image pairs. This method relates the covariance of the intensity difference in a matching image pair to the asymmetry in the cross-correlation plane peak. This covariance term is propagated via three-point Gaussian sub-pixel fit equation to yield the displacement uncertainty. The primary difference between the IM and CS is that the CS method accounts for all the pixels within an interrogation window, not just the matched particles.

1.1.2 Indirect Uncertainty Quantification Methods

Within the indirect classification, there are two approaches: uncertainty surface and correlation plane methods. Uncertainty surface methods [3] utilize a priori knowledge about an error source and its corresponding measurement error (i.e., the response to some error source) to predict uncertainty. This type of uncertainty method is, similar to the works of Kahler et al. [9] and Fincham & Delerce [10]. Using this approach, one selects a number of error sources and creates synthetic images from a defined velocity field while systematically varying the error source. Then, after processing the images, errors can be defined for each velocity vector. In this way, one can isolate error and the error source, and in turn, create an uncertainty response surface for the selected error sources. The primary limitation of this method is that a calibration for individual sources of error is needed, of which there are numerous (see [1]). Timmins et al. [3] have investigated particle image size, seeding density, shear rate, and particle displacement as potential error sources.

Correlation plane methods were developed by Charonko et al. [4] and solely utilize the correlation plane. In Charonko et al. [4], the authors observed that the magnitude of the displacement error is inversely proportional to the Primary Peak Ratio (PPR), or the ratio between primary and secondary correlation peaks. The authors argued that the PPR is the natural choice for uncertainty analysis because the Signal-to-Noise Ratio (SNR) encompasses all possible sources of error. As such, the authors formulated a relation between the PPR and the error, with software-specific fitting coefficients calculated from synthetic data. Later, Xue et al. [5] furthered this work by relating not only the PPR and RMS error, but also other measures of the SNR, such as peak-to-root mean square ratio, peak-to-correlation energy, and cross-correlation entropy. Xue et al. [5]

also formulated a new relation between the SNR and displacement error that does not assume a normal distribution of measurement error.

Xue et al. [6] also proposed uncertainty quantification using a new metric, Mutual Information (MI). The MI is the ratio of the cross-correlation peak to the auto-correlation of an ideal Gaussian particle and denotes the effective amount of correlating information. A higher MI suggests a higher number of particles correlating within the interrogation windows and thus the displacement can be measured with a lower uncertainty.

Sciacchitano et al. [11] compared the following uncertainty estimation methods: US, PPR (from [4]), IM and CS, in a jet flow, for regions with varying shear rate, particle image size, seeding density and out of plane motion. In their comparative analysis, CS uncertainty predictions matched the RMS error and yielded good coverage. IM showed a satisfactory dynamic response and overestimated the RMS error in the jet inviscid core, whereas US and PPR showed low sensitivity to error and predicted significantly lower and higher uncertainty coverage, respectively. In the present work, we build upon Sciacchitano et al. [11] by assessing the performances of new metrics MI and modified PPR [5], along with existing IM and CS algorithms, using PRANA¹ (Purdue University), Insight4G (TSI, Inc) and DaVis (LaVision, GmbH) processing to provide a software-independent generalized comparison of these uncertainty estimation methods. In addition, the present study provides an assessment of the uncertainty estimation methods across two experimental cases: a wake downstream of a cylinder in a water tank, and air jet flow. The following sections describe the experimental configuration, establish the validity of the reference data, evaluate the measurement error and uncertainty and discuss the performance of the uncertainty estimation methods.

1.2 Experimental Test Cases, Procedures and Methodologies

In order to assess the performance of each uncertainty method the measurement error must be known. But in practice the true solution of an experimentally measured flow is unknown. To overcome this challenge we follow the approach of Sciacchitano et al. [11] and utilize two synchronized PIV systems: a low resolution (measurement) and high resolution (reference) PIV

¹ <http://sourceforge.net/projects/qi-tools/>

system. For all experiments the two PIV systems were synchronized with a TSI model# 610036 synchronizer with timing resolution of 250 ps.

To ensure that the high resolution (HR) PIV system has a lower error than the low resolution (LR) system, and thus more closely approximates the true solution, we compared its results with Laser Doppler Velocimetry (LDV) measurements taken at a single point. Neal et al. [12] used hot-wire anemometry to establish a reference solution. However, in the present case LDV is used, primarily because of its non-invasive nature, which also allows for simultaneous PIV and LDV measurement at any grid point within the field of view. The LDV and HR were compared at a single location within the jet and cylinder flows so as to take simultaneous data between all measurement systems, rather than compare statistical quantities. Furthermore, the LDV is utilized to confirm that the HR has a lower error and uncertainty than the LR system. The primary objective is to compare the LR measurements to a ground truth measurement, which is the HR measurements, rather than the LDV measurements.

Each measurement system, whether LDV, LR PIV, or HR PIV will have greatly different spatial resolutions. This is inherently due in part to the difference in technique (i.e., the LDV probe volume size is determined independently from the PIV window size). But it is primarily due to PIV signal strength and the need to create a relatively large difference in magnification for the LR and HR systems. The HR should have as high spatial resolution as possible to compare well with the LDV measurements, but still acquire adequate signal strength. Additionally, the resolution of the LR measurements should be high enough to compare well with the HR measurements, but still maintain a significant magnification ratio. It is with these considerations in mind that led us to select the magnifications and spatial resolutions for each measurement technique and experiment. For all experiments the LDV measurement volume was aligned in the plane of the PIV laser sheet. A 250mm focal distance lens was used, and the LDV measurement volume size was an ellipsoid with dimensions of 88 microns in the PIV streamwise and out-of-plane directions, and 929 microns in the spanwise direction. The LDV measurement was considered to be the ground truth. Appendix A details the process used to validate the reference PIV systems for each experiment.

1.2.1 Cylinder in Cross Flow

The low and high resolution PIV systems each utilized a high-speed camera with a digital resolution of 800×1280 pixels, a pixel pitch of 20 microns and operating at 1,000 frames/sec (500

velocity fields/sec). The cameras were mounted on opposite sides of the test flow, as shown in Figure 1.1a. The magnifications ratio of the two cameras was approximately five. Relevant parameters for each of the PIV systems can be seen in Table 1.1.

Table 1.1. Cylinder in cross flow experimental apparatus parameters.

Measurement System	Lens	f#	Field of View (mm)	Calibration Factor ($\mu\text{m}/\text{pix}$)
Low Resolution	28 mm	22	155 x 97	121.26
High Resolution	105 mm	11	30 x 19	23.81

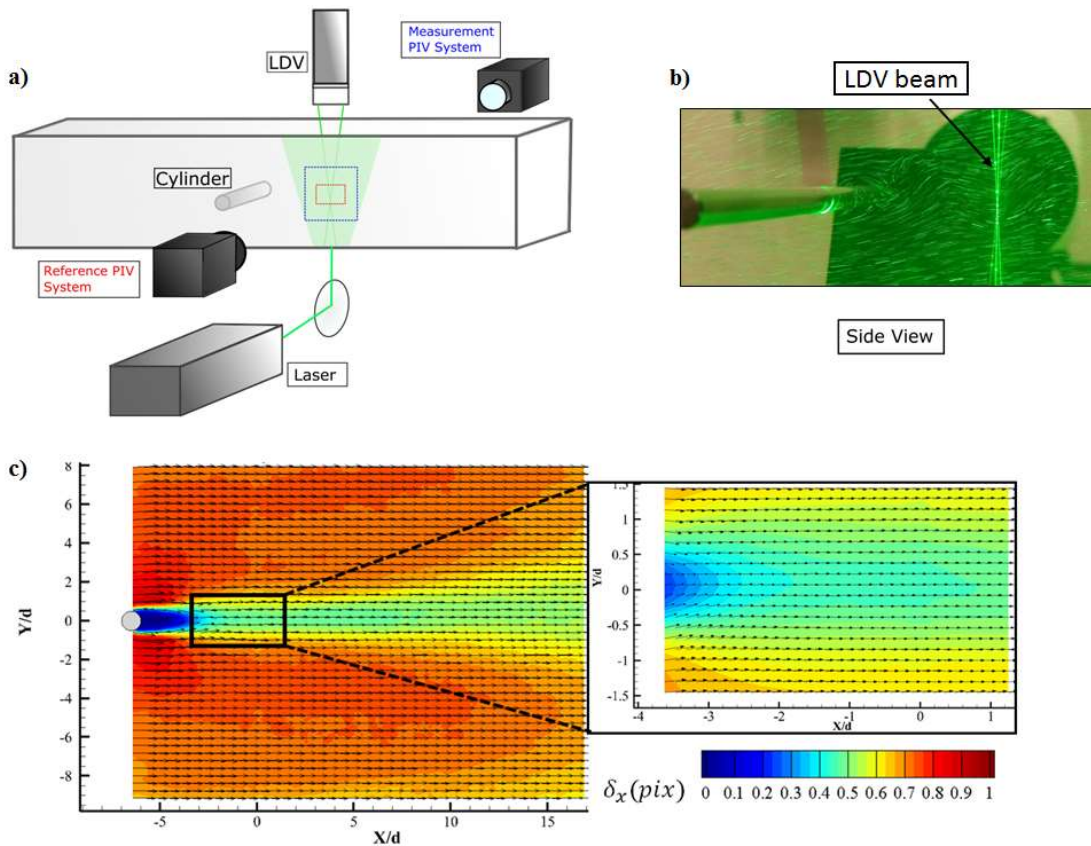


Figure 1.1. a) Experimental setup for the cylinder in cross flow cases. b) Side view photo with reference PIV system in the background. c) Time averaged contours and vectors of particle displacement for both low and high resolution PIV systems for the cylinder in cross flow ($Re_d = 480$) case. Measurements within the black box are those from the high resolution system. The LDV measurement location is at $X/d=0$, $Y/d=0$.

The flow consisted of a cylinder (diameter $D = 5\text{mm}$) in cross flow mounted in a channel with a width of 15.24 cm and half-channel height of 7.62 cm. The channel was filled with water

at room temperature and circulated by a centrifugal pump. During the experiment, the pump was operated at two different speeds, corresponding to Reynolds numbers $Re_d \approx 480$ and $Re_d \approx 730$ based on cylinder diameter and the bulk velocity. The flow was seeded with $12\mu\text{m}$ silver-coated hollow glass spheres with a density of 1.65 g/cc . The Continuum Terra PIV laser (15 mJ/pulse) shown in Figure 1.1a was a dual-head Nd:YLF laser with light-sheet forming optics mounted at the beam exit, consisting of a -25mm cylindrical lens and an adjustable combination of spherical lenses. This enabled us to locate the $\sim 1\text{mm}$ thick beam waist at the center of the measurement volume. The pulse separation time between the laser pulses was 1ms.

In order to verify the accuracy of the high resolution (reference) PIV system, we compared processed reference vectors with measurements from an LDV reference system. The LDV was considered the ground truth measurement and acquired by a TSI Powersight LDV system coupled into a fiber optic transceiver probe mounted above the channel. LDV beams were delivered from the top of the channel through a Plexiglas window and the water level was such that the beams were not projecting through a free surface. The LDV measured the streamwise component of velocity at a location 6.5 diameters downstream of the center of the cylinder. The seeding density was chosen such that it optimized the data acquisition for the PIV measurements. Since the LDV probe volume is smaller than the PIV interrogation window size and because the water channel speed was relatively slow, the resulting data rate for the LDV was approximately 300 Hz. Figure 1.1b shows a photo of the test flow, laser sheet, and LDV measurement volume. See Appendix A for more detailed information regarding the LDV measurement system. Figure 1.1c shows the relative field of view of the low and high resolution measurement system (cylinder case $Re_d = 730$ is not shown for the sake of brevity). The vectors and contours of mean streamwise velocity depict a wake profile symmetric about $X/d=0$. In Figure 1.1c every other vector is plotted in both x and y direction for the LR mean velocity field while all the vectors are shown for the HR case.

1.2.2 Circular Jet in Quiescent Flow

This experiment also utilized a low and high-resolution PIV system, each with the same high-speed camera as mentioned in section 1.2.1, operating at 3,200 frames/sec. In this case, 1,600 velocity fields per second was obtained with a laser pulse separation of 0.3125 ms. The cameras were mounted on either sides of the test flow. Relevant parameters for each of the PIV systems are shown in Table 1.2. The magnification ratio for the two cameras was approximately four.

Table 1.2. Jet flow experimental apparatus parameters.

Measurement System	Lens	$f\#$	Field of View (mm)	Calibration Factor ($\mu\text{m}/\text{pix}$)
Low Resolution	60 mm	5.6	114 x 71	88.41
High Resolution	105 mm	2.8	27 x 17	21.48

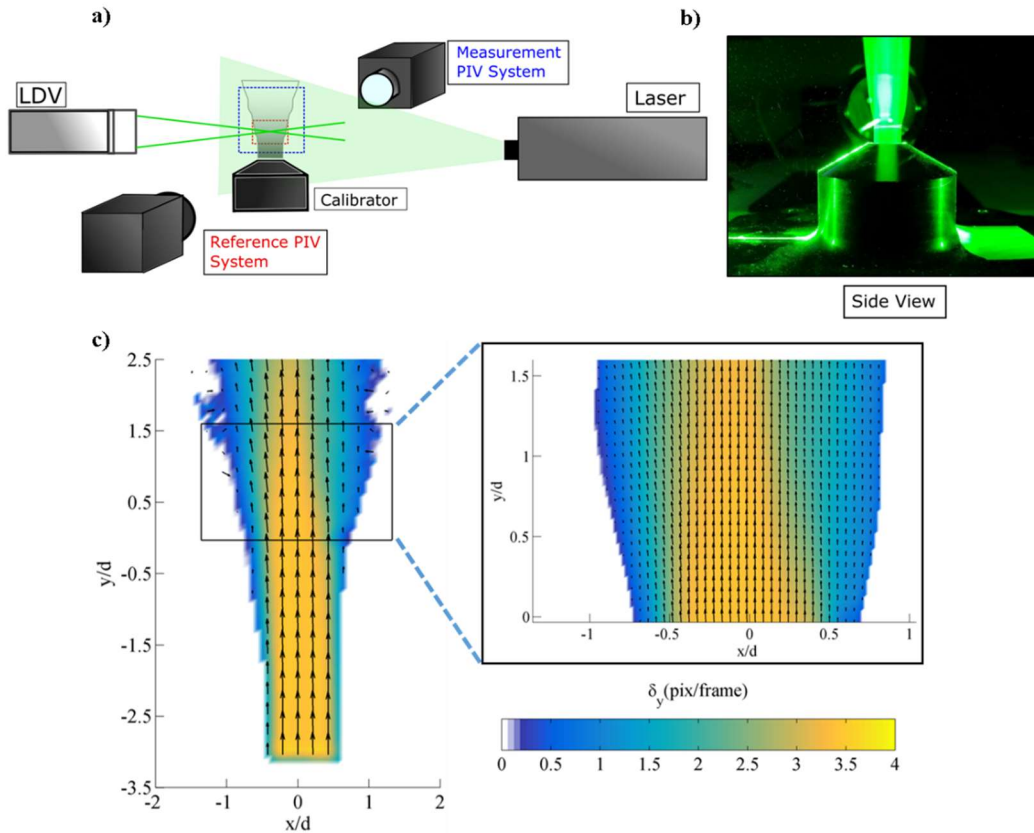


Figure 1.2. a) Experimental apparatus of the velocity measurement systems. b) Side view photo with the measurement system camera in the background. c) Time averaged contours and vectors of particle displacement for both low and high resolution PIV systems for the jet flow case.

Measurements within the black box are those from the high resolution system. The LDV measurement location is at $x/d=0$, $y/d=0$.

The experimental test flow was a three-dimensional (circular orifice) jet in quiescent flow. The air jet was generated using a TSI model# 1128B hotwire calibrator consisting of an upstream nozzle, pressurized settling chamber, flow conditioning screens, and an exit nozzle with a diameter of 10mm. The calibrator was designed to give a highly repeatable and steady flow near the nozzle exit. The exit speed of the jet was such that $Re_j \approx 2,500$ (based on the diameter of the jet). The seed particles were olive oil ($\rho \approx 900 \text{ kg}/\text{m}^3$) droplets (with a nominal mean diameter of 1

micron) generated by a TSI model #9302 atomizer and introduced into the settling chamber. The ambient fluid was not seeded and thus, near the edges of the measurement volume (i.e., shear layers), velocity vector outliers are possible. As such, we have not considered any outliers in the present study.

An illustration of the experimental apparatus is shown in Figure 1.2a. The same Continuum Terra PIV laser was used with a -25mm cylindrical lens and adjustable spherical light sheet optics which produced a light sheet thickness of approximately 1.2mm at the center of the measurement volume.

In order to verify the accuracy of the reference PIV system we again compared processed reference vectors with measurements from TSI Powersight LDV system. The LDV measurement volume was aligned to measure the streamwise velocity component of the jet at a location 3.2 jet diameters downstream of the orifice. The typical LDV data rate was greater than 5 kHz. See Appendix A for more detailed information regarding the LDV measurement system. The LDV beams crossed along the axis of the circular jet as shown in Figure 1.2b. Importantly, Figure 1.2b does not show the LDV measurement location used in the current study. Its actual location is defined as the origin in Figure 1.2c. Figure 1.2c compares the low resolution PIV fields with the high resolution measurement and shows the relative sizes of the respective field of views. Here, three vectors are skipped in each direction for both the LR and the HR mean velocity fields. The mean velocity profile for the jet exhibited a slight asymmetry. This however does not affect the comparisons since both PIV systems are subject to the same effect.

1.2.3 PIV Processing Algorithms

The PIV processing software used in this study include: PRANA (Purdue University), Insight4G (TSI Inc.), and DaVis (LaVision, GmbH). Each was used to process the low and high resolution PIV data sets and throughout this study, we present results from each. Each code utilized a standard cross-correlation (SCC) with multi-pass iterative window deformation, except for the high resolution processing by PRANA, which utilized the Robust Phase Correlation (RPC) method [13], [14], [15] also with iterative window deformation [16]. Validation, universal outlier detection median filtering [17] and smoothing occurred between passes to achieve a converged velocity field. The last pass results were used without any vector validation such that a replaced vector, for which the uncertainty estimate is not valid, is not accounted for in the statistics. To filter out bad

measurements in the last pass, measurement points with absolute error greater than 1 pixel were discarded from the analysis. See Table 1.3 for additional processing details.

Table 1.3. Processing parameters (number of passes, window sizes, and overlap) for each processing code.

<i>Experiment</i>	PRANA		Insight4G		DaVis	
	<i>No. of Passes</i>	<i>Window Size & Overlap</i>	<i>No. of Passes</i>	<i>Window Size & Overlap</i>	<i>No. of Passes</i>	<i>Window Size & Overlap</i>
Jet Low Resolution	2 3	64x64 (50%) 32x32 (75%)	5 3	64x64 (50%) 32x32 (50%)	2 3	64x64 (50%) 32x32 (75%)
Jet High Resolution	2 4	64x64 (50%) 48x48 (83.3%)	5 3	64x64 (50%) 48x48 (50%)	2 4	64x64 (50%) 48x48 (83%)
Cylinder Low Resolution	5 3	32x32 (75%) 16x16 (50%)	5 3	32x32 (50%) 16x16 (50%)	5 3	32x32 (75%) 16x16 (50%)
Cylinder High Resolution	5 3	128x128 (75%) 64x64 (87.5%)	5 3	128x128 (50%) 64x64 (50%)	5 3	128x128 (75%) 64x64 (87%)

The four uncertainty estimation methods assessed in this paper are: 1) PPR uncertainty method of Xue et al. [5] as implemented in *both* PRANA and Insight4G. 2) Mutual information uncertainty method of Xue et al. [6], implemented in PRANA. 3) Particle disparity method of Sciacchitano et al. [7], implemented in PRANA. 4) Correlation statistics method of Weineke [8], implemented in DaVis.

In the present evaluation (Table 1.3) the final pass window sizes are same across the software but window overlap is varied. For LR case, the overlap was same for PRANA and DaVis while it was lesser for Insight4G (in the jet case) due to software limitation. The window overlap in LR case is varied from 50% (for the cylinder case) to 75% (for the jet case) to obtain sufficient vectors for good statistics (Sciacchitano et al. [7] also used 75% overlap in their jet study). However, for HR processing a higher overlap of about 83% is used. Since the HR measurements are interpolated onto the LR system grid points for comparison, a higher overlap for HR yields smoother vector fields which aids in interpolation. To further analyze if increasing overlap and dependent statistics affect the error and uncertainty estimates, final pass velocity vectors are skipped in each direction and resulting error and uncertainty distributions are compared across the software's in Appendix B. The results clearly show that varying the overlap has insignificant effect on the RMS error and uncertainties for both flow cases in all three software.

1.2.4 Uncertainty Propagation from Reference Solution

The primary assumption in treating the high resolution measurement as the reference is based on resolving the same flow field and displacements over a larger number of pixels, compared to the low resolution recordings. Thus, in spite of similar uncertainty levels on sub-pixel displacements for both systems, the high resolution system yields a much lower uncertainty (in physical units) when scaled down by the higher magnification factor [11]. This is further verified by comparing both the measurements to an independent point measurement using LDV system, which has lesser uncertainty.

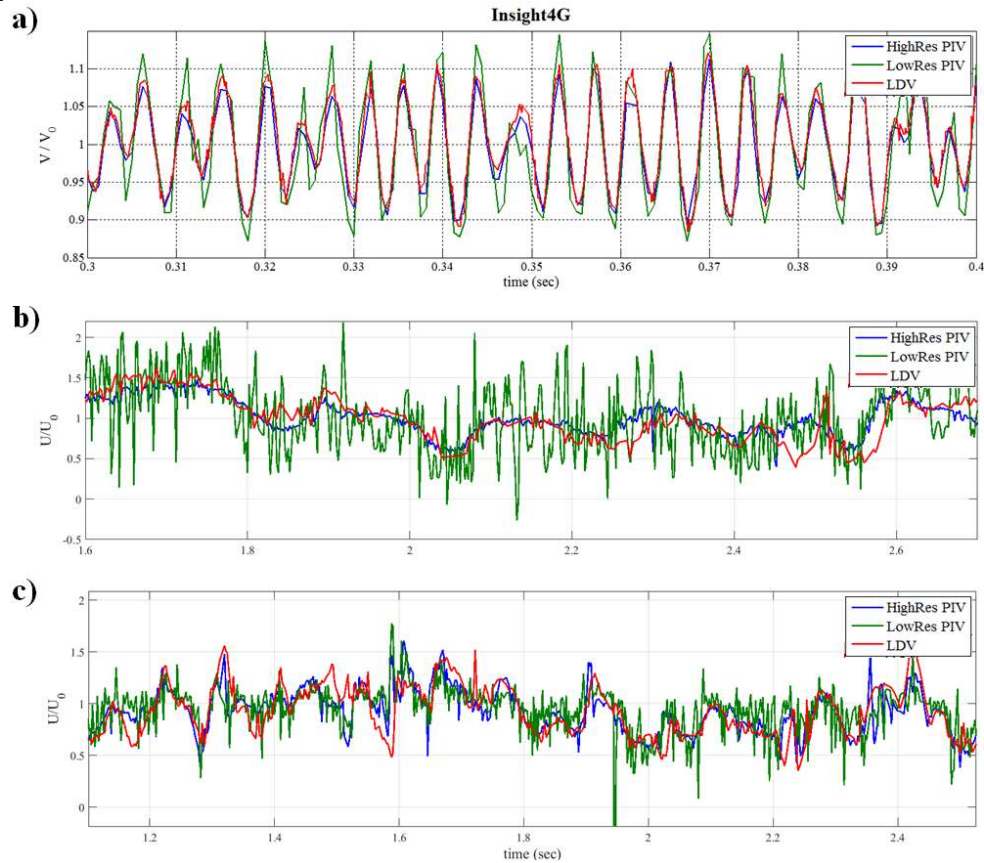


Figure 1.3. Instantaneous measurements (from Insight4G) of streamwise velocity from high and low resolution PIV systems and an LDV system. a) Jet experiment. b) Cylinder wake $Re_d = 480$. c) Cylinder wake $Re_d = 730$.

Figure 1.3 plots a representative streamwise velocity time series from each experiment for the LDV, reference, and measurement systems. The high resolution signal clearly shows better agreement with the LDV signal compared to the low resolution system. However, any errors in

the high resolution measurement, ϵ_{HR} , makes the error between the measurement and reference solution, ϵ_{LR} , deviate from the true error, ϵ_{true} , as given by equation (1) [11].

$$\epsilon_{true} = \epsilon_{LR} - \epsilon_{HR} \quad (1)$$

$$\sigma_{\epsilon_{true}}^2 = \sigma_{\epsilon_{LR}}^2 + \sigma_{\epsilon_{HR}}^2 - 2\rho(\sigma_{\epsilon_{LR}}\sigma_{\epsilon_{HR}}) \quad (2)$$

Following Sciacchitano et al. [11], for zero bias errors, knowing the magnification ratio and the cross correlation coefficient (ρ) between the measurement (LR) and reference (HR) system errors (each calculated with respect to the LDV measurement), one can approximate the deviation from the true RMS error using equation (2). Here σ represents the RMS of the true, LR, or HR error. In this study $\rho_{jet} = 0.15$ and $\rho_{wake} = 0.177$ ($Re_d = 730$). Thus, $\sigma_{\epsilon_{true}}$ underestimates $\sigma_{\epsilon_{LR}}$ by 1% for the jet case and by 2% for the wake case.

1.2.5 Error Distributions for Low Resolution Measurements

To compare the reference and measurement systems, at first the LDV point is taken as the origin and the common field of view between the cameras are determined using the respective magnifications. The reference velocity fields are then linearly interpolated using a two-dimensional scheme onto the measurement grid points in the overlapping fields of view. The overlapping field of view between LR and HR systems is 27mm by 16 mm for the jet case and 30 mm by 18.5 mm for the cylinder cases in x and y directions respectively. The domain of comparison is chosen as 12 mm by 5 mm for the jet case and 24 mm by 15 mm for the cylinder cases. All the error and uncertainty analysis presented herein is evaluated in this subdomain. Figure 1.4 shows the error magnitude histogram normalized by the total number of vectors for all three experiments. For all cases and processing codes the error distributions matched closely. The RMS values of the error magnitude distributions for each case are presented in Table 1.4.

Table 1.4. RMS of the magnitude error (pix) for each case and processing code comparing the HR and LR measurements.

<i>Case</i>	<i>PRANA</i>	<i>Insight4G</i>	<i>DaVis</i>
Cylinder, $Re_d = 480$	0.19	0.19	0.21
Cylinder, $Re_d = 730$	0.19	0.18	0.20
Jet	0.30	0.31	0.29

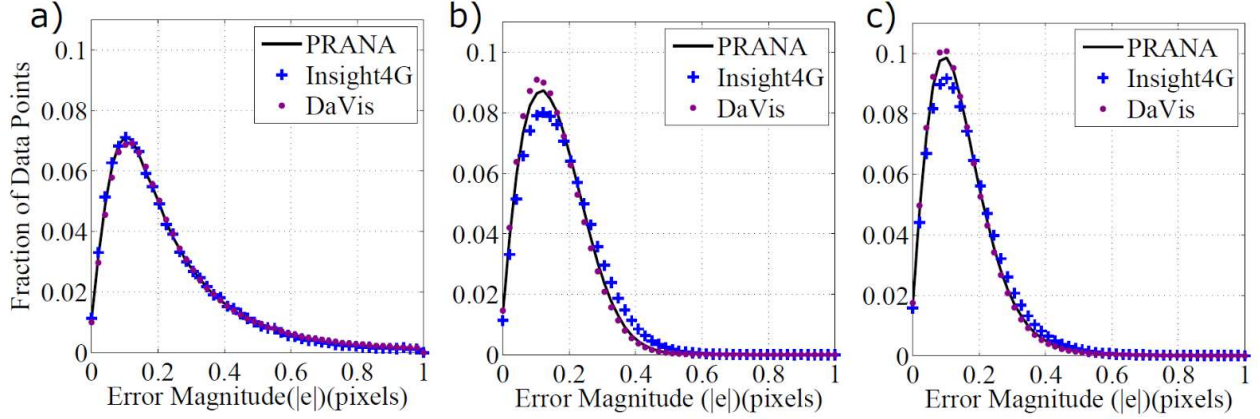


Figure 1.4. Error magnitude distributions for low resolution measurements.
a) Jet experiment. b) Cylinder wake $Re_d = 480$. c) Cylinder wake $Re_d = 730$.

1.3 Results & Discussion

We assess four uncertainty methods, PPR [5], MI [6], IM [7], and CS [8]. The IM and CS methods return independent values of uncertainty for each velocity component, e_x and e_y , whereas the PPR and MI methods return uncertainty values for the error magnitude, $|e| = \sqrt{e_x^2 + e_y^2}$. The PPR and MI methods both predict an Upper and Lower uncertainty Bound (UB and LB) on the error magnitude, but IM and CS return a single value that is assumed to be symmetric about the measurand. In Sciacchitano et al. [11], the PPR uncertainty on error magnitude was equally distributed between X and Y components. Here, for comparative assessment, the RMS of the PPR and MI uncertainty predictions (UB and LB) are directly compared with the 84.25% and 15.75% quantiles of the error magnitude distribution, following [5]. For IM and CS methods, the RMS of uncertainty is compared with RMS of error for X and Y components, following Sciacchitano et al. [11].

The four uncertainty estimation methods are compared using several metrics. Section 1.3.1.1 compares spatial variations of error and uncertainty over the field of view. Section 1.3.1.2 investigates error and uncertainty distributions. Section 1.3.1.3 examines expected and predicted uncertainty profiles across a plane and Section 1.3.1.4 compares standard coverages.

1.3.1 Low Resolution PIV Uncertainty Quantification

1.3.1.1 Contours of Expected and Predicted Uncertainty

For PPR and MI uncertainty estimates, the RMS of uncertainty UB is compared with the 84.25% quantile of error magnitude (denoted by $|e|^{0.84}$). For CS and IM, the RMS error and RMS uncertainty for the streamwise component are compared. The spatial distributions of expected and predicted uncertainties are plotted in Figure 1.5a (jet flow) and Figure 1.5b (wake flow at $Re_d = 730$). In each figure, the left column of plots indicates the expected distributions (either $|e|^{0.84}$ or RMS error) and the right column shows the predicted uncertainty maps.

In Figure 1.5a, the jet error distribution has its minimum within the core region, $-0.3 < x/d < 0.3$. In the shear layer, $x/d < 0.3$ and $x/d > -0.3$, the RMS error increases significantly. Qualitatively, a comparable trend is observed for the predicted uncertainties, but quantitatively, each method under predicts the expected uncertainty in the shear region. In the jet core, PPR method for both PRANA and Insight4G predicts about 0.2 pixels uncertainty which matches $|e|^{0.84}$. In the shear layer, PPR methods predict a maximum of about 0.4 pixels uncertainty compared to 0.55 pixels value for the error magnitude UB. The MI method predicts the same uncertainty range as PPR, with about 0.22 pixels uncertainty in $-0.4 < x/d < 0.4$ range but showing a flatter response to the error. Figure 1.5a also shows a better response by CS to error in the shear region when compared with IM. The RMS error varies from 0.15 to 0.35 pixels from the core to the shear region, whereas the predicted IM and CS uncertainties vary from 0.07 to 0.18 and 0.1 to 0.25 pixels, respectively. Thus, CS and IM under predict the RMS error in *both* the shear layer and jet core region.

The spatial distributions of error and uncertainty are plotted in Figure 1.5b, for the cylinder case with $Re_d = 730$. For the sake of brevity, the spatial distributions for the case $Re_d = 480$ are not shown but are similar. For each processing code, the maximum value of error is observed directly downstream of the cylinder in the region of velocity deficit. We note that for all uncertainty quantification methods, the error and uncertainty maps show a spike in predicted values at the LDV beam location ($X/d = 0$), which is attributed to the interference of the LDV beam with the PIV signal.

Contours for the RMS of uncertainty UB estimates using the PPR method vary from about 0.33 pixels in the wake center to about 0.26 pixels near the free stream, for both PRANA and

Insight4G. The error upper bound quantitatively matches the uncertainty upper bound at $X/d = -3.5, Y/d = 0$, but attains a value of 0.2 pixels near the free stream. The MI upper bound uncertainty prediction also responds well to the error, but predicts values of about 0.42 pixels in the wake center to 0.33 pixels near the free stream, overestimating the $|e|^{0.84}$ contours. IM and CS uncertainty estimates show a sharper decay of uncertainty towards the free stream velocity. For both the methods the estimated uncertainty varies from 0.15 pixels to about 0.1 pixels from the center towards the free stream, whereas the RMS error varies from 0.2 pixels to 0.12 pixels in the same domain. Thus, the magnitudes of the contours indicate an under prediction of uncertainty for both IM and CS, especially in the center of the wake.

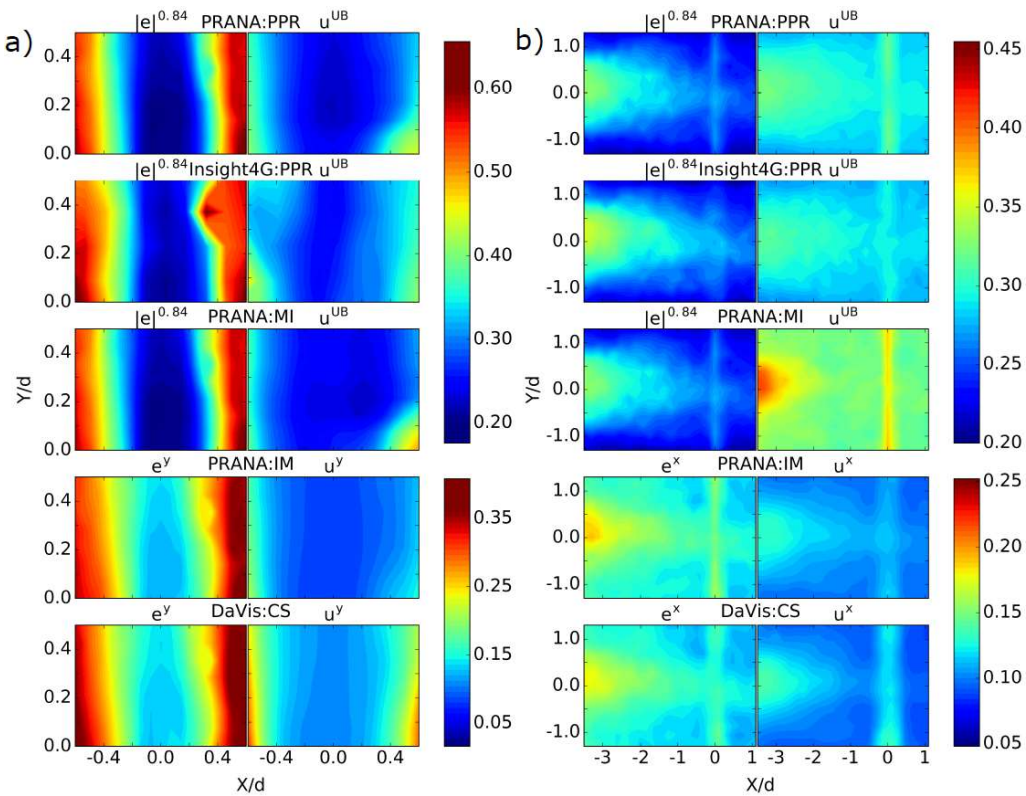


Figure 1.5. Error and uncertainty spatial contours for each method for the a) jet and b) wake flow experiment ($Re_d = 730$).

1.3.1.2 Error Uncertainty Histograms

The uncertainty estimates are further analyzed by comparing the error and uncertainty histograms in Figure 1.6 and Figure 1.7. As an example, Figure 1.6 shows the count of the error and uncertainty values falling within the same bin intervals. The top two plots (Figure 1.6, a and b)

display error magnitude, PPR, and MI uncertainty predictions for PRANA and Insight4G. The bottom two graphs (Figure 1.6, c and d) plot the X and Y velocity component errors and uncertainty estimates using the IM and CS methods. The PPR and MI uncertainty predictions have a lower and upper uncertainty bound, as described in Xue et al. [6], which bounds the error magnitude such that 68.5% of measurement error falls within this bound. For the IM and CS uncertainties a single distribution is plotted, assuming that the upper and the lower uncertainty bounds are symmetric about zero.

Error and uncertainty distribution histograms for the jet experiment are shown in Figure 1.6. We observe that the error distributions for both PRANA and Insight4G are in agreement. In regards to uncertainty, PRANA and Insight4G PPR uncertainties satisfactorily bound the error magnitude with the LB distributed between 0.02 to 0.1 pixels, the UB between 0.15 to 0.6 pixels, and the error magnitude mode is near 0.1 pixels. The MI uncertainty distribution is similar to the PPR uncertainty UB, but the mode of the distribution is at about 0.15 pixels which is closer to the error magnitude peak (0.1 pixels), compared to PPR distribution peak location (0.21 pixels).

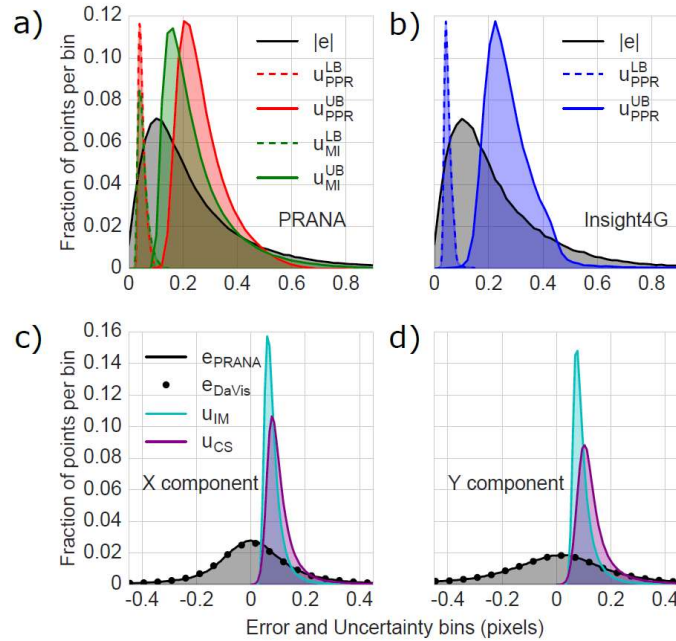


Figure 1.6. Error and uncertainty distributions for each uncertainty method for the jet experiment. a) PPR and MI distributions from PRANA. b) PPR distributions from Insight4G. c) IM distributions from PRANA. d) CS distributions from DaVis.

Referring to Figure 1.6c and d, we observe that the X and Y component error distributions for PRANA and DaVis overlay each other with a slight positive bias in the streamwise (Y)

direction. The IM uncertainty distributions, in both X and Y components, is sharply centered near 0.1 pixels, with the RMS of the distributions at 0.097 and 0.114 pixels, respectively. For the CS method, the corresponding RMS of the uncertainty predictions are 0.13 and 0.16 pixels, which are closer than IM to the RMS values of the error (0.17 pixels and 0.21 pixels) for both components. As was observed in Figure 1.5a, both the IM and CS uncertainty estimates under predict the RMS error.

Figure 1.7 plots the uncertainty and error histograms for the cylinder in cross flow experiments. The $Re_d = 480$ case is shown in Figure 1.7 (a, b, c and d) and the $Re_d = 730$ is shown in Figure 1.7 (e, f, g and h). The PPR uncertainty bounds for PRANA and Insight4G have a similar distribution with the lower and upper bound modal values placed on either side of the

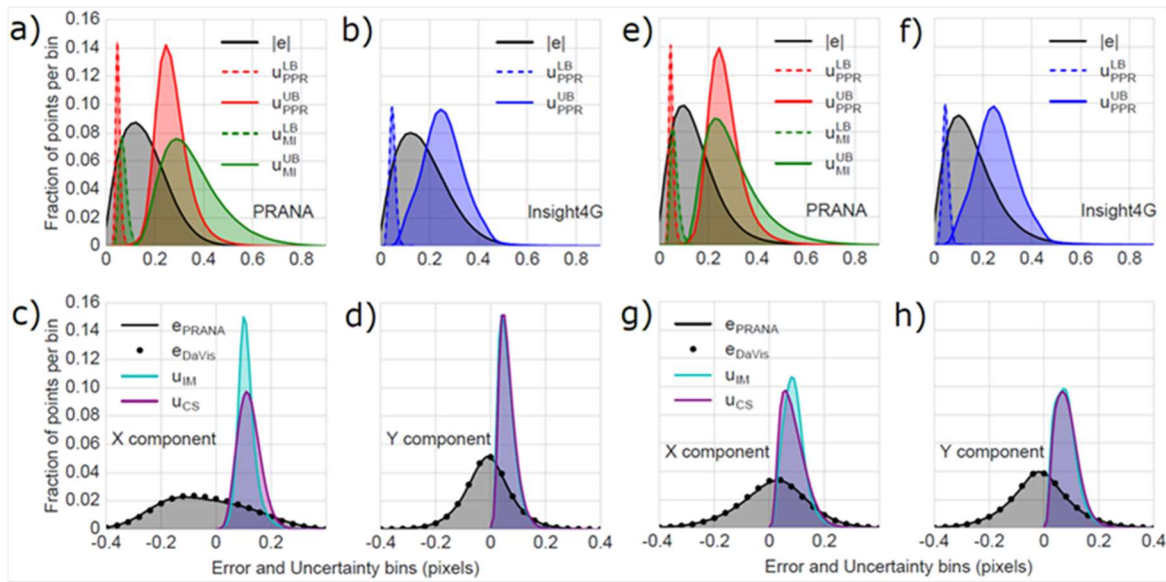


Figure 1.7. Error and uncertainty distributions for each uncertainty method for the both cylinder in cross flow experiments (a-d for $Re_d = 480$ and e-h for $Re_d = 730$).

peak of the error magnitude (in these plots, the LB is plotted with a different bin size to scale the number of counts for ease of visualization). The uncertainty LB is sharply centered on 0.05 pixels. The PPR uncertainty UB distribution has a lesser spread for PRANA compared to Insight4G, which is consistent with the error magnitude histograms in each case Figure 1.7 (a, b, e and f). The MI uncertainty prediction indicates a higher uncertainty with a longer tail, especially for the $Re_d = 480$ case, compared to the PPR uncertainty estimate.

In Figure 1.7 (c, d, g and h), the black dots represent the error distribution obtained from DaVis which closely matches the PRANA error distribution. We observe that the spanwise (Y) component error distribution appears to be symmetric about zero while the streamwise component error distribution for $Re_d = 480$ case is skewed towards the negative values and has a slight positive bias for the $Re_d = 730$ case. The main source of systematic error in Figure 1.7c is not known. However, the error distributions were evaluated for both the Reynolds number cases in an identical way and thus, we would expect that if the bias was a cause of comparison procedure that each Reynolds number case would incur a similar bias, but in fact, the bias for each was much different. We therefore conclude that the presence of the higher bias error in Figure 1.7c is certainly not an artifact of the LR versus HR comparison procedure. The IM and CS uncertainty estimates (u_{IM} , u_{CS}) are distributed between 0 and 0.2 pixels and are nearly identical in the spanwise direction. In contrast, in the streamwise direction the CS distribution for $Re_d = 480$ is wider than the IM distribution and thus predicts a higher RMS value for the X component uncertainty. The

Table 1.5. Comparing the mean, standard deviation and RMS of the error distributions for both X and Y components to the RMS of IM and CS uncertainty estimates. The values for all three experiments are mentioned in the table. All units are in pixels.

IM Method / PRANA

Case	Error Bias		Error Std. dev.		Error RMS		Uncertainty RMS	
	x	y	x	y	x	y	x	y
Jet	0.0129	0.0051	0.1631	0.2091	0.1636	0.2091	0.0968	0.1140
Re=480	-0.0362	-0.0060	0.1593	0.0918	0.1633	0.0920	0.1231	0.0731
Re=730	0.0181	-0.0105	0.1281	0.1177	0.1293	0.1181	0.1048	0.0943

CS Method / DaVis

Case	Error Bias		Error Std. dev.		Error RMS		Uncertainty RMS	
	x	y	x	y	x	y	x	y
Jet	0.0116	0.0038	0.1676	0.2105	0.1680	0.2106	0.1301	0.1570
Re=480	-0.0356	-0.0055	0.1541	0.0893	0.1581	0.0894	0.1328	0.0747
Re=730	0.0161	-0.0103	0.1257	0.1155	0.1267	0.1159	0.1039	0.0985

RMS uncertainty predictions are within 16% to 20% of the RMS errors for both Reynolds numbers except for u_{IM} in the streamwise direction, for $Re_d = 480$, which varies by about 25%.

To assess the contribution of the bias term in the estimated RMS of the error distributions, the statistics of the x and y error distributions for all three experiments are presented in Table 1.5. We first note that in the case of a zero bias error, the error standard deviation will be equal to the

RMS error. And second, if the uncertainty estimates completely account for the random uncertainty in the measurement then the RMS uncertainty should match the error standard deviation. Here, error and uncertainty in both x and y components are separately reported and thus, RMS uncertainty only for IM and CS methods are compared with the respective error standard deviations. Table 1.5 shows that the bias is maximum in the x-direction for the $Re_d = 480$ case, which leads to a 0.004 pixel difference between the error standard deviation and RMS. Thus in all cases, the systematic error does not make a significant difference (less than 0.004 pixels) between the RMS and the standard deviation of error. Also, the RMS of the predicted uncertainty does not match the standard deviation of error for both IM and CS evaluations which indicates that their under predictions of uncertainty is not solely due to the systematic error.

1.3.1.3 Expected and Predicted Uncertainties Across a Plane

The sensitivity of the uncertainty prediction to the variation in error is further analyzed using RMS uncertainty profiles taken spanwise across the jet. The RMS profiles for the jet case are shown in Figure 1.8. The top row (subplots a and b) of this figure graphs $|e|^{0.84}$, $|e|^{0.15}$, and the RMS of the PPR and MI uncertainty bounds for PRANA and Insight4G. The figure illustrates that $|e|^{0.84}$ and $|e|^{0.15}$ are similar for both PRANA and Insight4G. The predicted uncertainty LB shows a flat response to the variation in $|e|^{0.15}$. However, both the PPR and MI predicted uncertainty values (UB and LB) match the expected uncertainty values closely near the jet core region. In the shear layer, the predicted uncertainty UB shows good sensitivity to $|e|^{0.84}$, but with an under prediction in magnitude.

Plots c and d show a one-to-one comparison of IM and CS values of RMS uncertainty with the PRANA and DaVis values of RMS error respectively, for both velocity components. The RMS errors from PRANA and DaVis are in good agreement and show an increasing trend towards the shear layer. When comparing the CS and IM uncertainty predictions, we see that the CS method is slightly more sensitive to the error fluctuations in the shear region. While both IM and CS uncertainty profiles show good response to the RMS error, each suffers from an offset, or bias, that causes the uncertainty profiles to under predict.

Considering now the cylinder in cross flow experiments, we refer to Figure 1.9 (subplots a, b, c and d for $Re_d = 480$ case and subplots e, f, g and h for $Re_d = 730$ case). For the $Re_d = 480$ case, across the wake, the error magnitude UB and LB essentially show a flat profile with a

slight increase at the center ($Y/d = 0$). The uncertainty LB estimated by MI matches the expected uncertainty line exactly, though the uncertainty UB is significantly higher than expected. The PPR uncertainty LB is slightly lower than $|e|^{0.15}$, for both PRANA and Insight4G, while the uncertainty UB is much more sensitive to the variation in the $|e|^{0.84}$ profile. We also observe that the PPR uncertainty UB calculated by Insight4G matches the error UB almost exactly whereas the PPR uncertainty UB from PRANA slightly over estimates the expected uncertainty. Subplots c and d show a comparison for IM and CS. The RMS errors for PRANA and DaVis are in good agreement for each component. Both methods predict similar RMS uncertainties, which show good sensitivity to the variation in RMS error, but under predicts in magnitude.

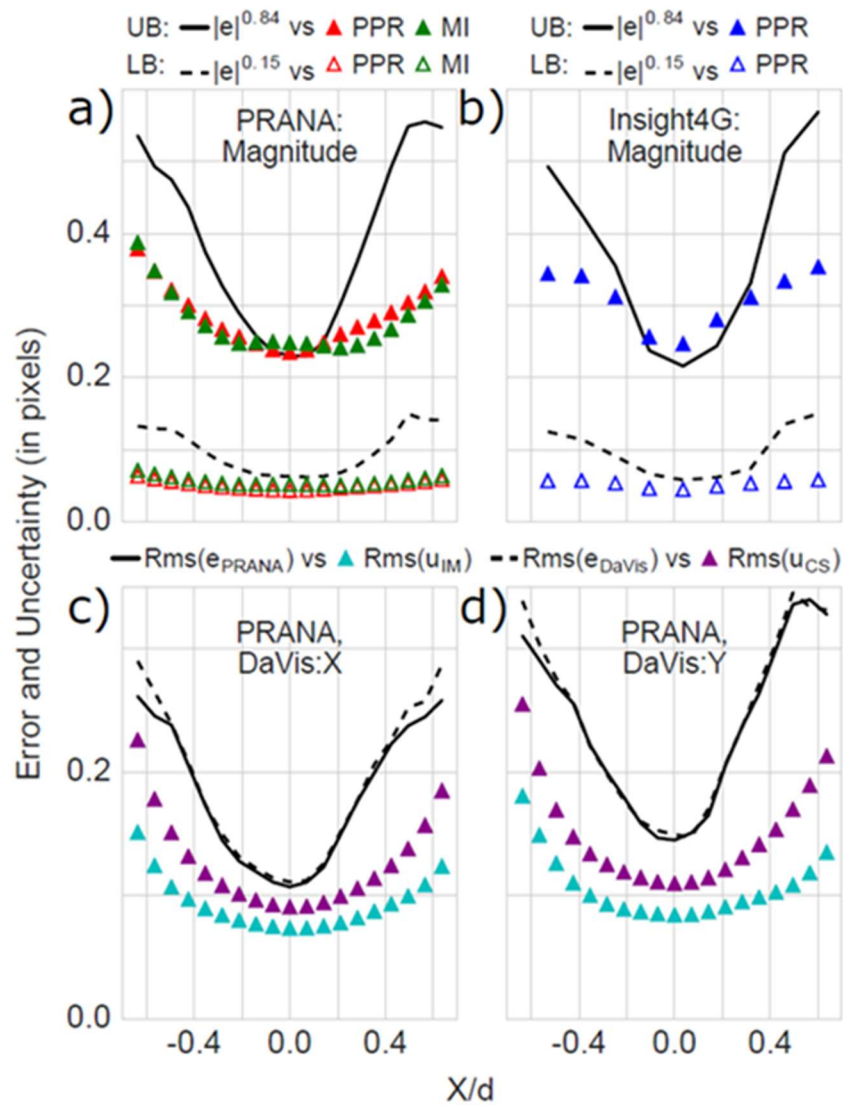


Figure 1.8. RMS error and uncertainty profiles along the spanwise direction across the jet flow.

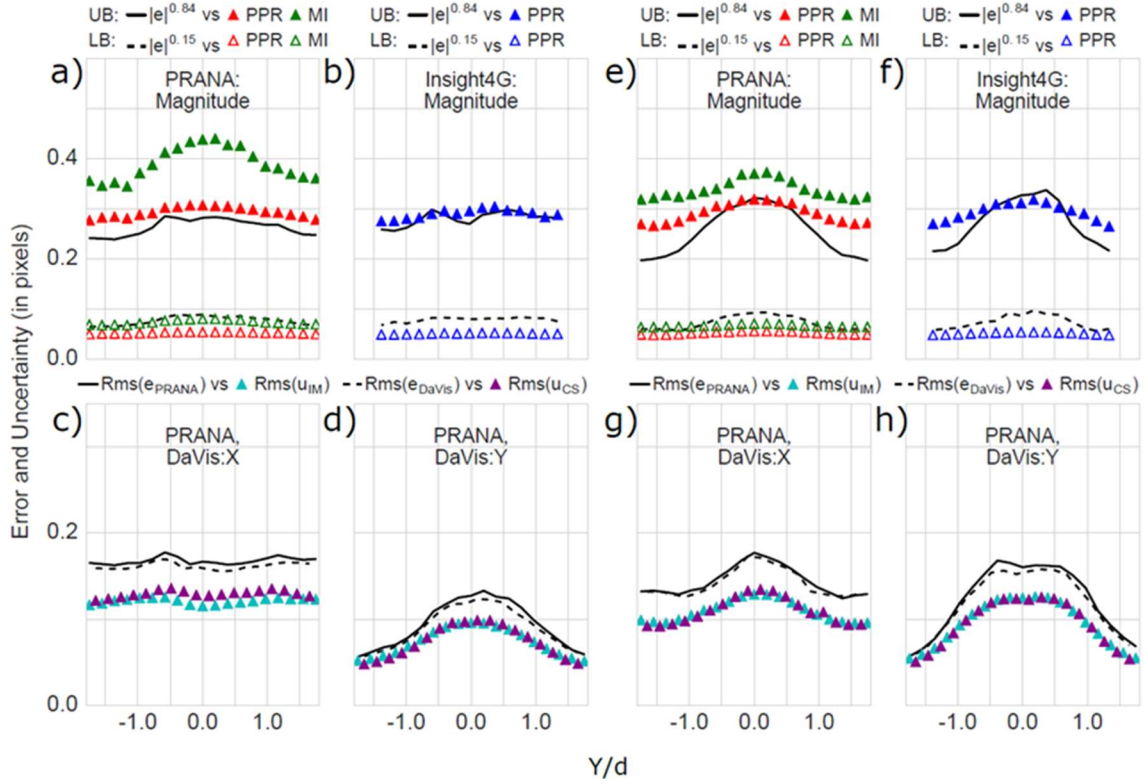


Figure 1.9. RMS error and uncertainty profiles across the wake of the cylinder in cross flow for $Re_d = 480$.

For $Re_d = 730$ case, the error profile in the streamwise (X) and spanwise (Y) directions are of similar magnitude, but in the spanwise direction, we observe a stronger sensitivity through the wake. PRANA and Insight4G UB and LB error magnitude are qualitatively similar. The PPR predictions match the expected uncertainty UB closely near $X/d = 0$, but show a lesser sensitivity towards the edges. Here, PRANA PPR prediction is quantitatively better near the center of the wake compared to Insight4G, although, both show similar response in the free stream region. The PPR uncertainty LB shows poor sensitivity and underestimates uncertainty LB for both PPR and MI metrics. In subplots g and h, the RMS error profiles from PRANA and DaVis match, and likewise the IM and CS RMS uncertainty profiles are almost identical. Both these methods show strong sensitivity to the RMS error across the whole profile. As was with the $Re_d = 480$ case, the IM and CS methods underestimate the expected uncertainty, especially in the wake center. This is consistent with the observations made in the RMS uncertainty spatial contours (Figure 1.5) and the uncertainty histograms (Figure 1.7).

1.3.1.4 Standard Coverages

A final metric to compare the effectiveness of different uncertainty methods is the standard uncertainty coverage. Coverage is defined as the percentage of measurement errors that fall within the uncertainty bound. The coverage should be equal to the level of confidence [18]. That means that at the standard level of confidence, 68.5% of error values should be within the standard coverage. A standard coverage value that is over or under 68.5% implies that either the uncertainty bounds were too large or too small, respectively.

For the jet experiment, Figure 1.10a, the PPR methods produced coverages (~64%) closest to the ideal 68.5% coverage, followed by MI at 54%. CS and IM under predicted the standard coverage in both spanwise and streamwise directions, but better in the spanwise (X) direction. The CS method returned coverage values of 54% in X and 47% in Y, while the IM method produced lower coverages of 45% in X and 38% in Y.

For the cylinder case with $Re_d = 480$ plotted in Figure 1.10b, the PPR method implemented in Insight4G yielded a coverage of 70%, which was closest to the ideal value. The PPR and MI methods in PRANA over predicted the standard coverage with equal values of 77%. CS and IM again under predicted the standard coverage in both spanwise and streamwise directions, but better in the spanwise (Y) direction. The CS method returned coverage values of 52% in X and 55% in Y, while the IM method produced lower coverages of 46% in X and 53% in Y.

Lastly, for the cylinder case with $Re_d = 730$ plotted in Figure 1.10c, the PPR method implemented in Insight4G yielded a coverage of 73%, which was closest among the methods to the ideal value, though over predicted. The PPR and MI methods in PRANA over predicted the standard coverage with values of 79% and 75%, respectively. CS and IM under predicted the standard coverage in both spanwise and streamwise directions, but slightly better in the spanwise direction. The CS method returned coverage values of 50% in X and 54% in Y. The IM method produced similar coverages of 51% in X and 52% in Y. We note that since these uncertainty metrics cannot predict the true bias in the measurement, a non-zero mean in the error distribution may lead to under prediction of uncertainty coverage even when the uncertainty predictions reasonably predict the random uncertainty.

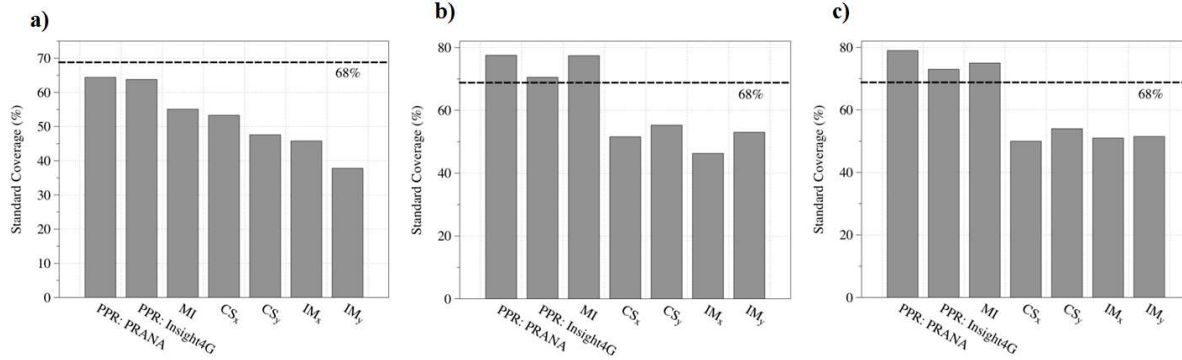


Figure 1.10. Standard coverages for each experiment, where the dashed line denotes the ideal standard coverage of 68.5%.

1.4 Discussion and Conclusions

The performance of four PIV uncertainty estimation methods were assessed in two canonical experiments: a jet in quiescent flow and a cylinder in cross flow (at two Reynolds numbers). Since the true solution is undetermined for an experiment, the measurement error was calculated by comparing two PIV systems: a high resolution (reference) and low resolution (measurement) system. The high resolution reference PIV system was validated by a LDV measurement, which were considered to be the ground truth measurement. Two calibration-based uncertainty metrics (PPR and MI) and two direct uncertainty methods (IM and CS) were evaluated using PRANA, Insight4G, and DaVis. In all cases, error distributions from different processing codes closely matched each other.

While comparing RMS error and uncertainty along a plane, we observed that for the jet experiment, the PPR uncertainties showed to have good sensitivity to the measurement error, matching it in the jet core, but under predicting it in the shear layer. The PPR method obtained a standard uncertainty coverage of about 64% for both implementations in PRANA and Insight4G. The MI method was less responsive than PPR and yielded coverage of about 55%. CS and IM predictions also were responsive but under estimated the RMS error in both the jet core and the shear layer. As such, the CS and IM methods under predicted the standard uncertainty coverage, posting values near 50% and 40%, respectively.

Similar observations were made for the cylinder in cross flow experiments. The PPR and MI predicted uncertainties varied according to the error, matching (in the case of PPR) or nearly matching (for MI) the error directly downstream of the cylinder and over estimating the uncertainty

in the shear layer. The PPR implementations in PRANA and Insight4G obtained standard coverages of about 77% and 72%, respectively. The MI method posted a standard coverage near 75%. The uncertainty lower bounds for both the PPR and MI showed less sensitivity to $|e|^{0.15}$ in all the experimental cases. The CS and IM methods responded well to the spatially varying error, with CS outperforming IM. However, because both CS and IM under predicted the error throughout the field of view, each obtained standard coverage values near 52%.

To compare the present work with Sciacchitano et al. [11], note that we must limit all comparisons to the section detailing the unsteady inviscid core, not including the effects of tilted light sheet or small particle images. The most striking difference in results from the two studies is that the response of the PPR method to the error was significantly improved in the current study. This can be attributed to the improved PPR calibration model of Xue et al. [5] which accounted for any asymmetry in the error distribution and predicted an upper and lower uncertainty bound for 68.3% confidence interval. Further improvement in sensitivity to measurement error may be obtained for PPR by utilizing the robust phase correlation [15], which generates a larger range of PPR values for a given error distribution, compared to SCC [4]. Also, fitting a different distribution between the PPR values and the error magnitude may yield higher sensitivity for this metric, however this is subject to future research.

The IM and CS methods showed good sensitivity to error in the present study, but did not match the RMS error as closely as in Sciacchitano et al.[11]. This could be related to unmatched particle pairs due to out of plane motion for IM method, but the exact reason is unknown. What is known is that the RMS of the uncertainty distributions did not match the standard deviations of the error for both IM and CS methods, indicating that the under predictions were not solely due to the systematic error.

In summary, we observe overall acceptable uncertainty prediction among the different processing codes and methods for both experiments in this study. In conjunction with Sciacchitano et al. [11], this work supports the notion that planar two component PIV uncertainty estimation methods provide good performance and robustness. However, further development is needed to address current limitations and weaknesses.

Acknowledgments

The authors would like to gratefully acknowledge Andrea Sciacchitano for the Image Matching uncertainty estimation code. This work was supported, in part, by a grant for Instrument Development for Biological Research, Grant #106700 – DBI – 1152304.

1.5 References

- [1] H. Huang, D. Dabiri, and M. Gharib, “On errors of digital particle image velocimetry,” *Meas. Sci. Technol.*, vol. 8, no. 12, pp. 1427–1440, 1997.
- [2] M. Raffel, C. Willert, and J. Kompenhans, *Particle Image Velocimetry*. 2007.
- [3] B. H. Timmins, B. W. Wilson, B. L. Smith, and P. P. Vlachos, “A method for automatic estimation of instantaneous local uncertainty in particle image velocimetry measurements,” *Exp. Fluids*, 2012.
- [4] J. J. Charonko and P. P. Vlachos, “Estimation of uncertainty bounds for individual particle image velocimetry measurements from cross-correlation peak ratio,” *Meas. Sci. Technol.*, vol. 24, no. 6, p. 065301, Jun. 2013.
- [5] Z. Xue, J. J. Charonko, and P. P. Vlachos, “Particle image velocimetry correlation signal-to-noise ratio metrics and measurement uncertainty quantification,” *Meas. Sci. Technol.*, vol. 25, no. 11, p. 115301, 2014.
- [6] Z. Xue, J. J. Charonko, and P. P. Vlachos, “Particle image pattern mutual information and uncertainty estimation for particle image velocimetry,” *Meas. Sci. Technol.*, vol. 26, no. 7, p. 074001, 2015.
- [7] A. Sciacchitano, B. Wieneke, and F. Scarano, “PIV uncertainty quantification by image matching,” *Meas. Sci. Technol.*, vol. 24, no. 4, p. 045302, Apr. 2013.
- [8] B. Wieneke, “PIV uncertainty quantification from correlation statistics,” *Meas. Sci. Technol.*, vol. 26, no. 7, p. 074002, 2015.
- [9] C. J. Kähler, S. Scharnowski, and C. Cierpka, “On the uncertainty of digital PIV and PTV near walls,” *Exp. Fluids*, vol. 52, no. 6, pp. 1641–1656, 2012.
- [10] A. Fincham and G. Delerce, “Advanced optimization of correlation imaging velocimetry algorithms,” *Exp. Fluids*, vol. 29, pp. S13–S22, 2000.
- [11] A. Sciacchitano, D. R. Neal, B. L. Smith, S. O. Warner, P. P. Vlachos, B. Wieneke, and F. Scarano, “Collaborative framework for PIV uncertainty quantification: comparative assessment of methods,” *Meas. Sci. Technol.*, vol. 26, no. 7, p. 074004, 2015.
- [12] D. R. Neal, A. Sciacchitano, B. L. Smith, and F. Scarano, “Collaborative framework for PIV uncertainty quantification: the experimental database,” *Meas. Sci. Technol.*, vol. 26, no. 7, p. 74003, 2015.

- [13] A. C. Eckstein, J. Charonko, and P. Vlachos, “Phase correlation processing for DPIV measurements,” *Exp. Fluids*, vol. 45, no. 3, pp. 485–500, 2008.
- [14] A. Eckstein and P. P. Vlachos, “Assessment of advanced windowing techniques for digital particle image velocimetry (DPIV),” *Measurement Science and Technology*, vol. 20. p. 075402, 2009.
- [15] A. Eckstein and P. P. Vlachos, “Digital particle image velocimetry (DPIV) robust phase correlation,” *Measurement Science and Technology*, vol. 20. p. 055401, 2009.
- [16] F. Scarano and M. L. Riethmuller, “Iterative multigrid approach in PIV image processing with discrete window offset,” *Exp. Fluids*, vol. 26, no. 6, pp. 513–523, 1999.
- [17] J. Westerweel and F. Scarano, “Universal outlier detection for PIV data,” *Exp. Fluids*, vol. 39, no. 6, pp. 1096–1100, 2005.
- [18] H. W. Coleman and W. G. Steele, *Experimentation, Validation, and Uncertainty Analysis for Engineers*. Hoboken, NJ, USA: John Wiley & Sons, Inc., 2009.
- [19] R. D. Gould and K. W. Loseke, “A Comparison of Four Velocity Bias Correction Techniques in Laser Doppler Velocimetry,” *J. Fluids Eng.*, vol. 115, no. 3, p. 508, Sep. 1993.
- [20] TSI Inc, “Powersight Solid State Laser-Based LDV System, LDV Data Taken on a Rotating Disk.” Application Note-Powersight-001.

Appendix A

A.1 Simultaneous PIV and LDV Measurements.

To ensure valid PIV measurements from the high resolution (reference) flow, we established the error using an LDV system at a certain location in the test flow. The primary disadvantage of LDV is non-synchronized data sampling. LDV measurements acquire a velocity data point every time a particle passes through the measurement volume. For this reason, LDV measurements are not evenly sampled and are inherently random, with the sampling rate dependent upon the seeding density and the local velocity. To account for the differences in time between PIV and LDV signals we first ensured the highest possible LDV data sampling rate, then utilized a Piecewise Cubic Hermite Interpolating Polynomial (PCHIP) interpolation scheme to synchronize the LDV and PIV measurements.

In regard to spatial resolution of the LDV measurement, in each experiment, the LDV measurement consisted of a 50mm beam separation and a focusing lens with a 250mm focal distance which produced a measurement volume that was an ellipsoid with dimensions of 88 microns in the PIV streamwise and out-of-plane directions, and 929 microns in the spanwise direction. For the jet case, the reference PIV measurement utilized a final-pass window size of 48x48 pixels (1.03 x 1.03 mm). Therefore, in the streamwise direction, the LDV volume is 9% of the window size and 90% in the spanwise direction. For the cylinder experiments, the final-pass window size is 64x64 pixels (1.52 x 1.52 mm). In this case, the LDV volume is just 6% of the window size in the streamwise direction and 61% in the spanwise direction.

LDV measurement statistics such as the mean can suffer from velocity bias due to the fixed measurement time and particles of different velocities entering the measurement volume. Inherently, faster moving particles will be over-sampled. This effect was mitigated through the use of transit time weighting (Gould and Loseke [19]). Each velocity data point was normalized (weighted) with its own gate time. Slower particles have longer gate times and, therefore, more weight. With this weighting, the calculated mean velocity is closer to the actual mean. The LDV accuracy on a single measurement basis was 0.5%. In order to verify this, a verification of the LDV accuracy was performed using a rotating disk. Details of the verification can be found in [20]. There are two critical advantages of LDV: 1) LDV is a non-intrusive technique, and 2) LDV is unaffected by the PIV laser light sheet. This is important because in Neal et al. [12], a hot-wire was used for reference validation. Although very high frequency measurements are capable with

a hot-wire, they pose two problems in conjunction with simultaneous PIV measurements. The first is that the seeding particles can have an adverse effect on the analog signal. Second, hot-wires rely on convective cooling for velocity measurement and as such, cannot be placed in a laser light sheet due to artificial heating. Therefore, Neal et al. [12] placed the hot-wire *near the high resolution reference flow*. To account for this offset, the authors utilized Taylor's frozen flow hypothesis to essentially translate turbulent flow in time. The use of LDV enabled us to overcome both of these limitations and as such, we were able to measure velocities at any point within the light sheet, and so match any location of the high resolution measurements without the need for Taylor's frozen flow hypothesis.

A.2 Jet Flow Validation.

The LDV system utilized a light wavelength of 561nm. This wavelength was chosen to be different from the PIV laser, so that laser light from the LDV beams could be fully filtered out of the PIV images using camera filters, as is demonstrated in Figure 1.11. The LDV sampling rate was approximately 3.5 times the high resolution PIV data frequency. A representative time history of the comparison between streamwise velocity from the LDV and high resolution PIV is shown in Figure 1.12.

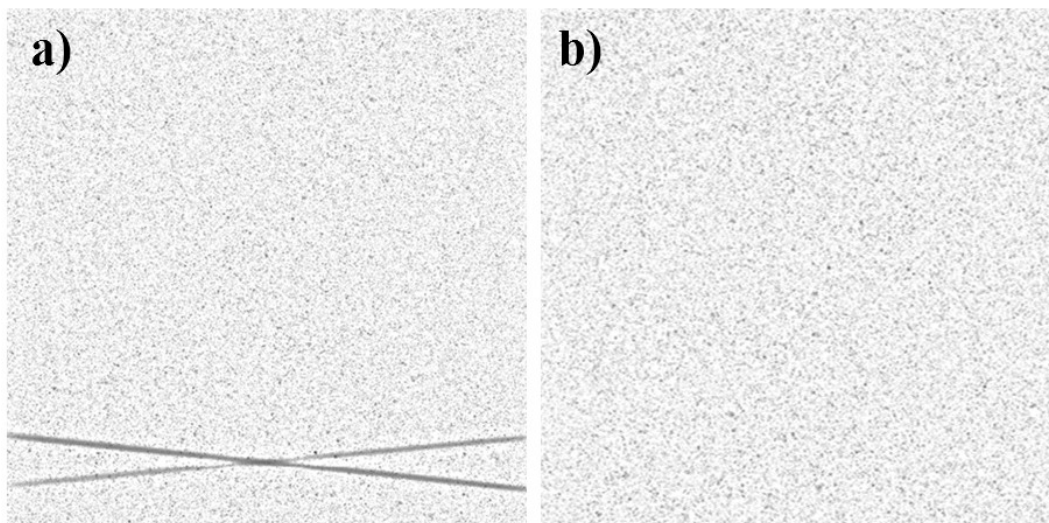


Figure 1.11. a) Inverted high resolution frame without filter showing LDV cross-beams. b) Inverted high resolution frame with filter.

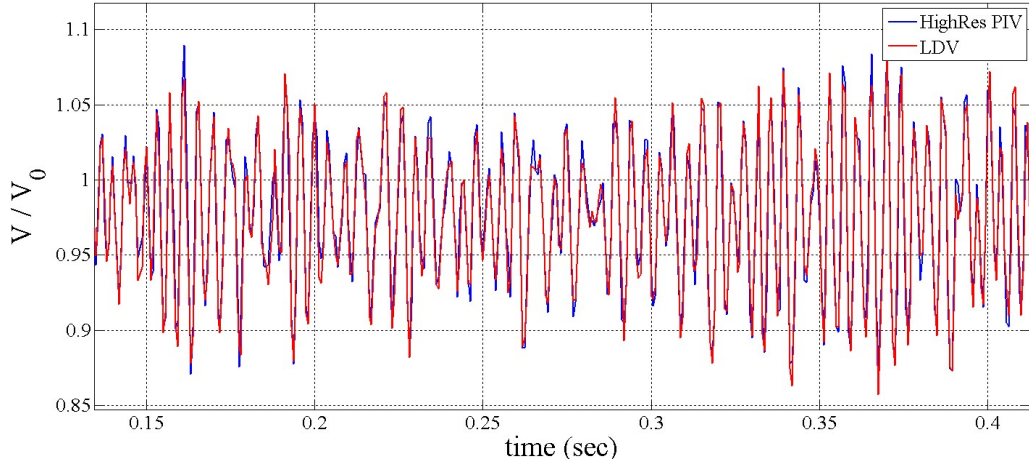


Figure 1.12. Representative time history comparison of streamwise velocity between the high resolution PIV and LDV systems for the jet experiment.

Table 1.6. Mean and RMS signal comparisons between the high resolution and LDV measurements as calculated by each processing code for the jet experiment.

<i>Code</i>	<i>Mean Streamwise Velocity (m/s)</i>	<i>RMS Streamwise Velocity (m/s)</i>
LDV	3.88	0.19
PRANA	3.88	0.19
Insight4G	3.88	0.19
DaVis	3.88	0.19

Table 1.7. RMS absolute error, RMS relative error, and cross-correlation coefficient between high resolution and LDV measurements as calculated by each processing code for the jet experiment.

	<i>RMS Absolute Error (pix/frame)</i>	<i>RMS Relative Error</i>	<i>Cross correlation Coefficient</i>
PRANA	0.11	0.7%	98.7%
Insight4G	0.12	0.8%	98.5%
DaVis	0.12	0.8%	98.6%

Table 1.7 details the absolute error, relative error, and cross-correlation coefficient between LDV and high resolution measurements for each processing code. Figure 1.13 shows the distribution of displacement error between the LDV and high resolution PIV measurements for all processing

codes. The error was obtained by mapping the LDV signal onto the high resolution grid by using the uniform calibration specified in Table 1.2. All processing codes returned remarkably similar error distributions and as seen in Table 1.7, the cross-correlation was high and the relative error was less than 1%. Therefore, we considered the high resolution PIV system as a validated reference solution.

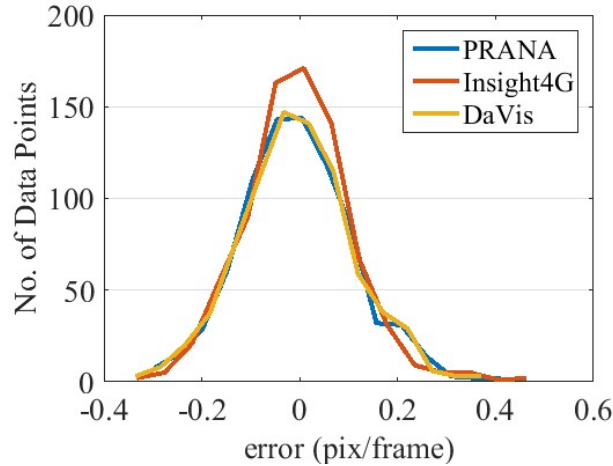


Figure 1.13. Error distributions between the reference PIV and LDV.

A.3. Cylinder in Cross Flow Validation.

In the cylinder experiments, the LDV system again utilized a light wavelength of 561nm. Unlike the jet flow experiment though, this wavelength was not different than the wavelength of the PIV laser. As a result, the LDV beams were not filtered from the PIV images. To remove the beams from the PIV images, an average intensity image was calculated and subtracted from the raw data images. This technique eliminated most effects from the LDV beams—however, a remnant did remain. This remnant manifested itself by occasionally illuminating individual seed particles that were capable of fouling the cross-correlation. Furthermore, in the cylinder in cross flow experiments, the seeding densities in water were lower than the densities in air (for the jet flow experiment), as were the mean velocities. Therefore, the data rate of the LDV was approximately 300Hz, which was lower than the PIV data rate of 500Hz. To account for the differences in time, we again utilized a PCHIP interpolation scheme to synchronize the LDV and PIV measurements. For the present analysis, we interpolated the LDV measurements onto the uniform PIV capture times. For completeness' sake we also completed an analysis with PIV measurements down

sampled onto the random LDV measurement times, but saw a negligible difference between the two procedures.

A representative time history of the comparison between streamwise velocity from the LDV and high resolution PIV is shown in Figure 1.14, and the error distribution shown in Figure 1.15. In Figure 15, less than 0.2% vectors had an error greater than a pixel for the $Re_d = 480$ case. About 5% vectors had an error greater than two pixels for the $Re_d = 730$ case.

Table 1.8 details the mean and Root-Mean Square (RMS) statistics between the high resolution and LDV measurements for each PIV processing code. It's apparent from Table 1.8 that the discrepancies between the PIV and LDV are larger for the cylinder experiments than for the jet experiment. We attribute this discrepancy to the low LDV sampling rate. Even so, the cross correlations are reasonably high for all processing codes. It is to be noted that the errors indicated in Table 1.8 are calculated using high resolution system magnification whereas the low resolution system errors are reported in pixels using LR magnification in Table 1.4. Since the magnification ratio is about 5, the errors in HR system with respect to LDV measurement when calculated with low resolution magnification yields values in the range $0.3 / 5 = 0.06 \text{ pix}$ to $0.8 / 5 = 0.16 \text{ pix}$. This error level is lower than the corresponding low resolution measurement error with respect to LDV, which establishes the high resolution PIV system to be a valid reference solution.

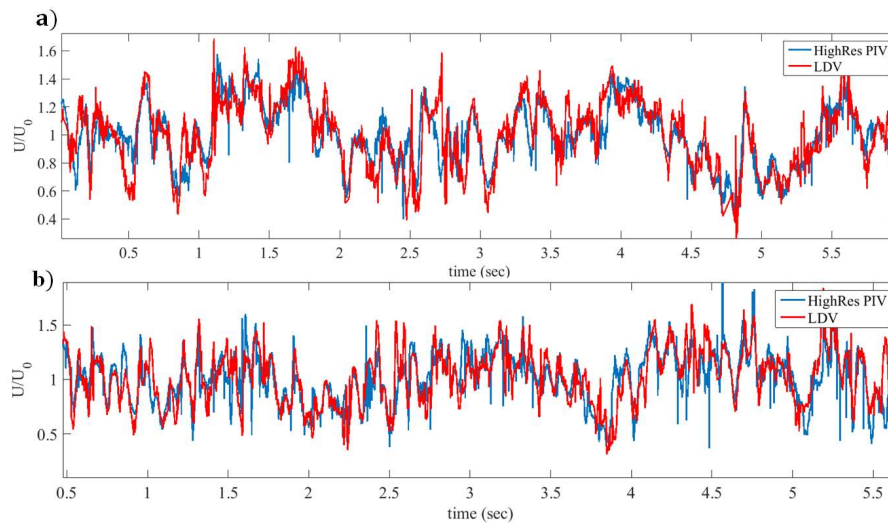


Figure 1.14. Representative time history comparisons of streamwise velocity between the high resolution PIV and LDV systems for both cylinder in cross flow experiments. a) $Re_d = 480$. b) $Re_d = 730$.

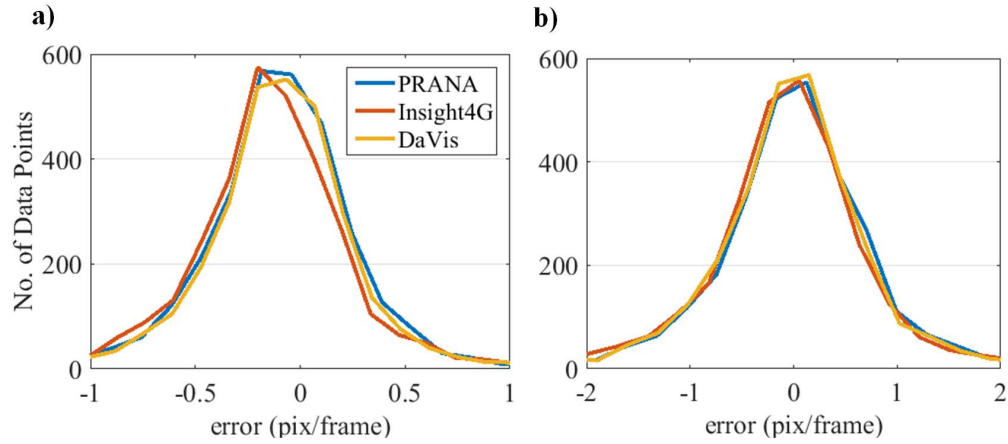


Figure 1.15. Error distributions between the reference PIV and LDV.
a) $Re_d = 480$. b) $Re_d = 730$.

Table 1.8. Mean displacement, RMS absolute error, and cross-correlation coefficient between high resolution and LDV measurements as calculated by each processing code for the cylinder in cross flow experiments.

Measurement	$Re_d = 480$			$Re_d = 730$		
	Mean Streamwise Velocity (m/s)	RMS Absolute Error (pix/frame)	Cross correlation coefficient	Mean Streamwise Velocity (m/s)	RMS Absolute Error (pix/frame)	Cross correlation coefficient
LDV	0.058	Not Available	-	0.11	Not Available	-
PRANA	0.056	0.32	80%	0.11	0.81	70%
Insight4G	0.055	0.33	81%	0.10	0.77	68%
DaVis	0.056	0.31	82%	0.10	0.80	72%

Appendix B

The effect of window overlap on the error and uncertainty statistics are tested by skipping the final pass velocity field vectors in each direction (X and Y) for the Jet case and the Cylinder case (for $Re_d = 480$). The results are presented for all three software. For an initial overlap of 75%, skipping 1 vector leads to 50% overlap and 2 vectors leads to 25% overlap. For 50% overlap processing, choosing alternate vectors leads to 0% overlap. RMS error and uncertainty values and the RMS of the error magnitudes indicate negligible variation with percentage window overlap in all cases. Thus, choice of window overlap in this document does not affect the results.

Table 1.9. Variation of RMS error and uncertainties in the jet flow case for PRANA and DaVis processing.

PRANA (Jet)	Number of valid vectors (%Overlap)	RMS Error Magnitude	RMS Error		RMS Uncertainty (IM)	
			X	Y	X	Y
Skip=0	496349 (75)	0.2997	0.1636	0.2091	0.0968	0.1140
Skip=1	144204 (50)	0.3066	0.1676	0.2125	0.1005	0.1183
Skip=2	59925 (25)	0.3106	0.1695	0.2155	0.1052	0.1243
DaVis (Jet)	Number of valid vectors (%Overlap)	RMS Error Magnitude	RMS Error		RMS Uncertainty (CS)	
			X	Y	X	Y
Skip=0	494775 (75)	0.3090	0.1680	0.2106	0.1301	0.1570
Skip=1	143672 (50)	0.3183	0.1727	0.2147	0.1357	0.1627
Skip=2	59685 (25)	0.3244	0.1749	0.2182	0.1426	0.1698

Table 1.10. Variation of RMS error and uncertainties in the cylinder flow case ($Re_d = 480$) for PRANA and DaVis processing.

PRANA (Cylinder Re=480)	Number of valid vectors (%Overlap)	RMS Error Magnitude	RMS Error		RMS Uncertainty (IM)	
			X	Y	X	Y
Skip=0	1765488(50)	0.1925	0.1633	0.0920	0.1231	0.0731
Skip=1	479590(0)	0.1915	0.1632	0.0906	0.1228	0.0722

DaVis (Cylinder Re=480)	Number of valid vectors (%Overlap)	RMS Error Magnitude	RMS Error		RMS Uncertainty (CS)	
			X	Y	X	Y
Skip=0	1673727 (50)	0.1859	0.1581	0.0894	0.1328	0.0747
Skip=1	431929(0)	0.1857	0.1578	0.0895	0.1323	0.0744

Table 1.11. Variation of RMS error and uncertainties in the jet and the cylinder flow case ($Re_d = 480$) for Insight4G processing.

Insight4G (Jet)	Number of valid vectors (%Overlap)	RMS Error Magnitude	Insight4G (Cylinder Re=480)	Number of valid vectors (%Overlap)	RMS Error Magnitude
Skip=0	107315 (50)	0.2906	Skip=0	1168049 (50)	0.2056
Skip=1	31541 (0)	0.2893	Skip=1	311556(0)	0.1988

2. PARTICLE IMAGE VELOCIMETRY (PIV) UNCERTAINTY QUANTIFICATION USING MOMENT OF CORRELATION (MC) PLANE

Sayantana Bhattacharya¹, John J. Charonko², Pavlos P. Vlachos¹

¹ School of Mechanical Engineering, Purdue University, USA.

² Physics Division, Los Alamos National Laboratory, USA.

This chapter has been previously published in Measurement Science and Technology, 29 115301.

DOI: <https://doi.org/10.1088/1361-6501/aadfb4>

Abstract

We present a new uncertainty estimation method for Particle Image Velocimetry (PIV), that uses the correlation plane as a model for the probability density function (PDF) of displacements and calculates the second order moment of the correlation (MC). The cross-correlation between particle image patterns is the summation of all particle matches convolved with the apparent particle image diameter. MC uses this property to estimate the PIV uncertainty from the shape of the cross-correlation plane. In this new approach, the Generalized Cross-Correlation (GCC) plane corresponding to a PIV measurement is obtained by removing the particle image diameter contribution. The GCC primary peak represents a discretization of the displacement PDF, from which the standard uncertainty is obtained by convolving the GCC plane with a Gaussian function. Then a Gaussian least-squares-fit is applied to the peak region, accounting for the stretching and rotation of the peak, due to the local velocity gradients and the effect of the convolved Gaussian. The MC method was tested with simulated image sets and the predicted uncertainties show good sensitivity to the error sources and agreement with the expected RMS error. Subsequently, the method was demonstrated in three PIV challenge cases and two experimental datasets and was compared with the published image matching (IM) and correlation statistics (CS) techniques. Results show that the MC method has a better response to spatial variation in RMS error and the predicted uncertainty is in good agreement with the expected standard uncertainty. The uncertainty

prediction was also explored as a function of PIV interrogation window size. Overall, the MC method performance establish itself as a valid uncertainty estimation tool for planar PIV.

Nomenclature

$\pm \mathcal{U}$: General uncertainty bounds

σ : Standard deviation

σ_x : Standard uncertainty in variable x

\vec{V} : Velocity vector

V_x : x component of velocity

V_y : y component of velocity

e : Error in velocity evaluations

$\langle R \rangle$: Ensemble averaged cross correlation plane

\mathcal{F} : Forward Fourier transform

R^* : Spectral cross-correlation

P_I : Particle image shape information

$G(x)$: Generalized Cross correlation (GCC)

$p(x)$: PDF of displacement.

I_{XX} : Second order moment about x - axis

I_{YY} : Second order moment about y -axis

R_{conv} : Gaussian convolved PDF plane

N_{eff} : Effective number of pixels contributing to correlation

e_{Prana} : Error in velocity measurements obtained using Prana processing

e_{DaVis} : Error in velocity measurements obtained using DaVis processing

σ_x^{MC} : Standard x uncertainty estimate using MC method

σ_y^{MC} : Standard y uncertainty estimate using MC method

σ^{MC} : Standard uncertainty estimate using MC method

σ^{IM} : Standard uncertainty estimate using IM method

σ^{CS} : Standard uncertainty estimate using CS method

2.1 Introduction

Particle Image Velocimetry (PIV) is a non-invasive quantitative fluid velocity measurement technique in which tracer particles are illuminated by a laser sheet, imaged by a high-speed camera, and the displacement of the particle patterns within an image sequence is estimated to resolve the velocity field. An overview of the development of PIV over the past 20 years is given by Adrian [1], and a comprehensive history can be traced in recent publications [2], [3]. Currently, the term PIV is used to encompass the extensive family of methods that are based on evaluating the particle patterns displacement using statistical cross-correlation of consecutive images with high number density flow tracers [2].

However, despite detailed investigation of potential error sources, the development of PIV methods did not involve simultaneous rigorous quantification of uncertainty for a given measurement. As a result, there is currently no widely accepted framework for reliable quantification of PIV measurement uncertainty. The situation is exacerbated by the fact that PIV measurements involve instrument and algorithm chains with coupled uncertainty sources, rendering quantification of uncertainty far more complex than most measurement techniques. Also, knowing the uncertainty bound on each PIV vector is crucial in comparing experimental results with numerical simulations. Therefore, developing a fundamental methodology for quantifying the uncertainty for PIV is an important and outstanding challenge.

Recent developments in this field have led to several uncertainty estimation methods which can be broadly classified into indirect and direct uncertainty estimation algorithms.

2.1.1 Indirect methods

The indirect methods use pre-calculated calibration information to predict the measurement uncertainty. In the first such method published, Timmins et al. constructed an “Uncertainty Surface” (US) by mapping the effects of selected primary error sources such as shear, displacement, seeding density, and particle image diameter to the distribution of the true errors for a given measurement [4]. This approach is analogous to a traditional instrument calibration procedure for standard experimental instruments. Ultimately, in order to comprehensively quantify the uncertainty, all possible combinations of displacements, shears, rotations, particle image diameters, and other

parameters must be exhaustively tested which can make this method computationally expensive. Moreover, many of the relevant parameters may not be easily obtained from a real experiment.

Charonko and Vlachos proposed an uncertainty quantification method based on the ratio of the primary peak height to the second largest peak (PPR) [5] in the correlation plane. Using this method, the uncertainty of PIV measurement can be predicted without a priori knowledge of image quality and local flow conditions. Reliable uncertainty estimation results using a phase-filtered correlation (RPC)[6] were shown, however for standard cross-correlation (SCC) techniques the uncertainty estimates were not as good. Also, the approach depends, like the uncertainty surface method, on calibration of the peak ratio to the expected uncertainty. Xue et al.[7] used an analogous approach to calibrate the measurement uncertainty with various other correlation plane signal to noise ratio (SNR) metrics. The uncertainty coverage, which denotes the probability of measurement errors falling between the uncertainty bounds is used as a metric to compare the different uncertainty predictions. The SNR based uncertainty methods developed by Xue et al. showed an improved uncertainty coverage for both RPC and SCC. In another effort, the effective information contributing to the cross correlation plane primary peak was named the “Mutual Information (MI)”[8] and used to predict the PIV measurement uncertainty. The MI between a correlated image pair is an estimate of the effective number of correlating particles and thus higher MI should correspond to a lower uncertainty on the measured velocity. Xue et al. successfully used MI as an indirect metric to predict the uncertainty in a PIV measurement.

2.1.2 Direct methods

The uncertainty in a measurement can also be extracted directly from the image plane using the estimated displacement as a prior information. Sciacchitano et al. proposed a method to quantify the uncertainty of PIV measurement based on particle image matching (IM) or particle disparity [9]. The uncertainty of measured displacement is calculated from the ensemble of disparity vectors, which are due to incomplete matching between particle pairs within the interrogation window. This method accounts for random and systematic error; however peak-locking errors and truncation errors cannot be detected. In addition, the disparity can be calculated only for particles that are paired within the interrogation window, thus this method cannot account for the effects of in-plane and out-of-plane loss of particles. Finally, particle image pair detection can introduce

additional sources of error and the method can be computationally expensive for high resolution images with higher seeding density.

Wieneke in his “Correlation Statistics” (CS) method computed the measurement uncertainty by relating the asymmetry in the correlation peak to the covariance matrix of intensity difference between two almost matching interrogation windows [10]. This is a more generalized image matching technique where the random error is estimated by the variance of pixel wise intensity difference and linked to the correlation function shape using the uncertainty propagation for a 3-point Gaussian fit. Due to pixel-wise matching, any loss of correlation due to out of plane motion or other possible error sources are taken into account. However, the method is limited statistically in case of smaller window size and bigger particle image size.

In a comparative assessment of the methods, Sciacchitano et al. [11] compared these four methods for an experimental jet case. Four different cases were tested, each one having a dominant primary error source (shear, out-of-plane motion, particle size and seeding density). The authors established that for zero bias the RMS of the error distribution should match the RMS of the predicted uncertainty distributions and this was used as the basis of comparison. The results indicated a better uncertainty prediction and sensitivity to RMS error variation for the direct methods (CS and IM) in all four cases. Both the calibration-based methods underperformed. The PPR method showed less sensitivity, especially in the shear region, while the US method exhibited a flat response for the case with out-of-plane motion. In another comparative study using jets and wakes, Boomsma et al. [12] showed that indirect methods can yield a better uncertainty prediction with a better calibration using a distinct upper and lower bound for prediction. The analysis also revealed higher sensitivity for direct methods, although, it was shown that IM and CS methods can under-predict the standard uncertainty even when the systematic error is negligible.

Recently, Scharnowski et al. [13] proposed an uncertainty estimation method based on the loss-of-pairs due to out-of-plane motion. They quantified the loss-of-pairs as a ratio of the volume of the cross-correlation function to the volume of the autocorrelation function and proposed an uncertainty estimate based on the estimated loss-of-pairs. Optimizing this uncertainty prediction model for real experiments showed minimum error is achieved when loss of correlation due to out-of-plane motion is less than one.

In this work, we adopt an alternative approach and seek to quantify PIV measurement uncertainty directly from the information contained within the cross-correlation plane. The cross-

correlation plane represents the distribution of probabilities of all possible particle image pattern displacements between consecutive frames, combined with the effect of the number of particles, mean particle image diameter and effects that contribute to loss of correlation. In other words, the correlation plane is a surrogate of the combined effects of the various sources of error that govern the accurate estimation of a particle pattern displacement. The primary peak or the highest peak in the cross-correlation plane denotes the most probable displacement for a given particle image pattern. For an ideal shift between the particle image patterns, a perfect cross-correlation peak can be represented by a convolution between a Dirac function (at the location of the shift) and the autocorrelation of particle image diameter. However, any deviation in the peak shape is a manifestation of the errors influencing the measurement. The particle image diameter information can be removed from the cross-correlation plane to obtain a Generalized Cross-Correlation (GCC) plane, which contains only the phase information of the correlation plane. The concept of GCC has been previously introduced by Wernet[14] and Thomas et al[15]. Here we show that the PDF (Probability Density Function) of displacements in a PIV interrogation window is directly related to the GCC plane. Since, the standard uncertainty is typically defined as the standard deviation of the PDF of all possible measurement values, we believe it is possible to directly estimate the uncertainty of each PIV measurement by the second order moment of the correlation plane. Hence, in this work we introduce a new method, the Moment of Correlation (MC), and establish the appropriate processing steps to extract the standard uncertainty from the cross-correlation plane. We demonstrate the sensitivity of the MC method to elemental error sources and compare its performance with existing methods (CS and IM) for synthetic and experimental data. This method has the benefit over those previously proposed in that limited additional pre- or post-processing is required, and it is not necessary to perform extensive processing-dependent calibration steps beforehand.

2.2 Methodology

The standard uncertainty is defined in section 2.2.1. We then derive the PDF of the displacement from the cross-correlation plane in section 2.2.2 and finally describe the methodology to extract the standard uncertainty from the PDF in section 2.2.3.

2.2.1 Definition of uncertainty

Uncertainty ($\pm\mathcal{U}$) is the estimate of a range of values around the measurement that contain the true result and bounds the true error. Usually, the uncertainty is provided at a defined “confidence interval”, this means a certain percentage of data points will stay within the provided range. For example, the confidence interval within one standard deviation (σ) range for a Gaussian error distribution is 68% and within $\pm 2\sigma$ range is 95%. Standard uncertainty (σ_x) is defined as the one standard deviation (σ) level for the parent population of the variable x [16], which is not required to be a Gaussian distribution. Therefore, the equation to calculate standard uncertainty can be written as follows (equation (3)):

$$\sigma_x^2 = E\left[(X - \mu)^2\right] = \int_x (x - \mu)^2 p(x) dx \quad (3)$$

Where μ is the mean or expected value for x , and $p(x)$ is the probability distribution function (PDF).

2.2.2 Statistics of PIV correlation plane and uncertainty

Scharnowski et al. [17] showed that for an ensemble PIV correlation, the PDF of observed displacements in that ensemble, $p(d)$, can be calculated by deconvolving the contribution of the average particle image, P_I , from the ensemble averaged correlation ($\langle R \rangle$) [21] (equation (4)):

$$\langle R \rangle = p(d) \otimes P_I \quad (4)$$

We propose that for an instantaneous measurement, the PDF of possible displacement matches can be also computed by removing the particle image shape information (P_I). If image a_2 is obtained by shifting image a_1 by displacement d , as shown in equation (5), then using the Fourier shift theorem, the Fourier Transform (FT) (\mathcal{F}) of image a_2 can be written as shown in equation (6):

$$a_2(x) = a_1(x - d) \quad (5)$$

$$A_2(r) = \mathcal{F}\{a_2\} = \mathcal{F}\{a_1(x - d)\} = A_1 \exp(-ird) \quad (6)$$

In PIV, typically the displacement d is estimated using Standard Cross Correlation (SCC) technique ($R = a_1 \otimes a_2$), which is evaluated in the Fourier domain using equation (7) as shown in Figure 2.1. Here, R^* denotes the FT of the cross-correlation plane (R). The average particle image information P_I can be estimated from the magnitude part of the cross correlation, in the frequency domain ($|R^*|$), as shown in equation (8), where $\overline{A_1}$ denotes the complex conjugate of the FT of the image a_1 i.e. $A_1 = \mathcal{F}(a_1)$.

$$R^* = \mathcal{F}\{R\} = \overline{A_1(r)} \cdot A_2(r) = \overline{A_1} \cdot A_1 \exp(-ird) \quad (7)$$

$$P_I \approx \mathcal{F}^{-1}\{|R^*|\} = \mathcal{F}^{-1}\{|\overline{A_1} \cdot A_2|\} \quad (8)$$

So, P_I can be removed by dividing R^* by its magnitude ($|R^*|$) in the frequency domain and the Inverse Fourier Transform (IFT) of that ratio forms a Generalized Cross Correlation (GCC), plane, denoted by $G(x)$, as shown in equation (9).

$$G(x) = \mathcal{F}^{-1}\left(\frac{R^*}{|R^*|}\right) = \mathcal{F}^{-1}\left(\frac{\overline{A_1} \cdot A_2}{|A_1 \cdot A_2|}\right) = \mathcal{F}^{-1}(\exp(-ird)) \quad (9)$$

Since the FT is a linear operation, the remaining part is the summation of all possible matching shifts as described by equation (6), and therefore the GCC plane represents the PDF of candidate displacements. However, we consider the location of the primary peak (highest peak) as the most probable displacement, and given the displacement, the spread of the primary peak region is considered as the PDF of interest for our case. Therefore, the primary peak region in $G(x)$ (as shown in Figure 2.1) is the PDF ($p(x)$) of all possible matches in the correlated image pair that contribute to evaluation of the most likely displacement, multiplied by some constants having to do with the intensity level of the images correlated. It is to be noted that even though any distortion or warping in the particle image shape directly affects the cross-correlation peak shape, the underlying PDF is not influenced by that distortion as the particle image shape information is removed from the PDF as described in equation (9).

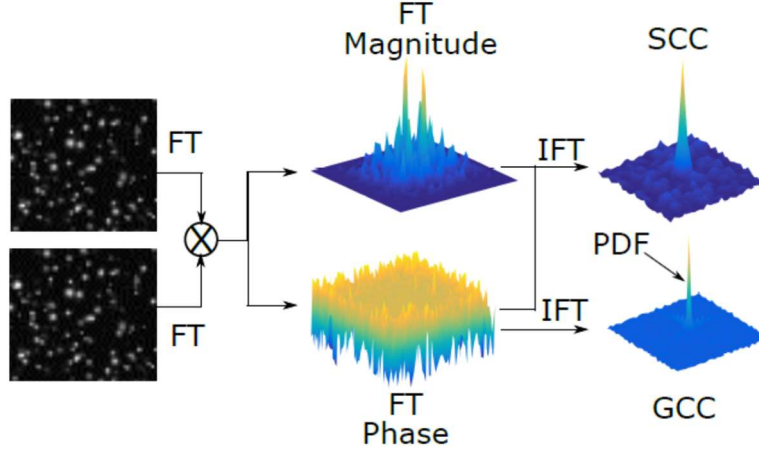


Figure 2.1. Extracting PDF of displacement from PIV image pair cross correlation.

Once the PDF of possible displacements is obtained, the second order moment about the primary peak, X_p , can be calculated as:

$$I_{xx}^2 = \int_X (x - X_p)^2 p(x) dx = \int_X (x - X_p)^2 G(x) dx \quad (10)$$

Comparing equation (10) and (3), it is obvious that the standard uncertainty for a given PIV correlation can be expressed as $\sigma_x = \sqrt{\int (x - X_p)^2 p(x) dx} = I_{XX}$. Therefore, the expected relationship between I_{XX} and σ_x should be one-to-one.

However, calculating I_{XX} directly is subject to large bias and random errors due to limited resolution in resolving the sharp primary peak in the normalized GCC plane. To compensate, we compute I_{XX} by performing a Gaussian least square fit on the GCC plane convolved with a Gaussian function. Convolution of the GCC plane with a Gaussian low-pass filter to estimate peak location with subpixel accuracy is an established practice in the PIV community[6][18]. The diameter of the convolving Gaussian is typically the diameter estimated from the primary peak of the cross-correlation plane. In case the particle image size is less than a pixel and the cross-correlation peak subpixel estimate is subjected to peak locking, a diameter of 3 to 4 pixels, based on the autocorrelation width for an ideal PIV particle image size, can be used as the convolution kernel diameter. The algorithm to find the standard uncertainty is described in the following section.

2.2.3 Moment of Correlation (MC) Algorithm

The Moment of Correlation algorithm, as described in Figure 2.2, extracts the standard PIV measurement uncertainty from the GCC plane. As a first step (Figure 2.2a) we convolve the GCC plane or the PDF with a 2d Gaussian function with a zero mean and an average diameter (\bar{D}), which is estimated from the SCC plane primary peak using a least squares elliptic Gaussian fit. Here, we define the diameter of a Gaussian to be 4 times its standard deviation. The convolved GCC plane R_{conv} is given by

$$R_{conv} = G(x, y) \otimes \exp \left[-8 \left(\frac{x^2}{\bar{D}^2} + \frac{y^2}{\bar{D}^2} \right) \right], \quad (11)$$

where $\bar{D} = (D_x + D_y)/2$ and D_x, D_y are the estimated least square fit diameters in the x and y directions respectively. For a large number of particles in an interrogation window the PDF ($G(x, y)$) can be reasonably approximated by a Gaussian distribution. Consequently R_{conv} should also be a Gaussian. It is to be noted that an arbitrary non-Gaussian PDF will be a limitation for estimating the PDF standard deviation (equation (13)). However, a Gaussian PDF is a common assumption and is also used directly in the IM method and indirectly in the CS method through 3-point Gaussian fit uncertainty propagation equation.

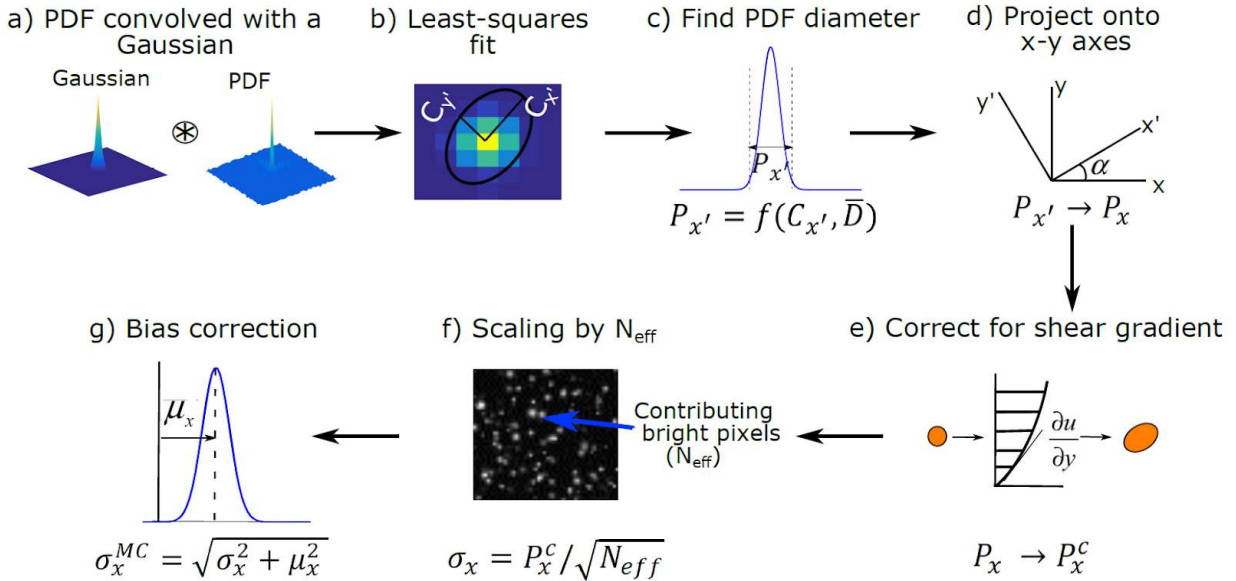


Figure 2.2. Algorithm to find standard uncertainty from PDF of displacements.

In the next step, Figure 2.2b, a Gaussian least squares fit is performed on the peak region of R_{conv} to estimate the peak location (X_c, Y_c) and its spread $(C_{x'}, C_{y'})$. The general possibility of the R_{conv} peak shape being elliptic Gaussian due to velocity gradients or the covariance of σ_x and σ_y is considered and thus the major axis $C_{x'}$, minor axis $C_{y'}$ and orientation α are estimated using the least squares fit (equation (12)).

$$\sum_{\text{minimize}} \left(R_{conv} - C_0 \exp \left[-8 \left\{ \frac{\left(\frac{\cos \alpha (X - X_c) - \sin \alpha (Y - Y_c)}{C_{x'}} \right)^2}{+ \left(\frac{\sin \alpha (X - X_c) + \cos \alpha (Y - Y_c)}{C_{y'}} \right)^2} \right\} + C_1 \right] \right)^2 \quad (12)$$

In equation (12), C_0 and C_1 are arbitrary constants accounting for the peak height and noise floor. Once $C_{x'}$ and $C_{y'}$ are known, equation (13) is used to evaluate the PDF major axis $P_{x'}$ and minor axis $P_{y'}$ (Figure 2.2c):

$$\begin{aligned} P_{x'} &= \sqrt{C_{x'}^2 - \bar{D}^2} \\ P_{y'} &= \sqrt{C_{y'}^2 - \bar{D}^2} \end{aligned} \quad (13)$$

This relation (equation (13)) follows from the definition of convolution between two Gaussian functions. For a bivariate Gaussian convolution, the resulting Gaussian covariance matrix can be expressed as a sum of the covariance matrix of the convolving Gaussian functions, which reduces to equation (13), if one of the convolving Gaussian functions is a circular Gaussian function (the Gaussian kernel in equation (11)). In the present analysis of the methodology and the results we have used D_x and D_y as different diameters in x and y directions. However, the diameters D_x and D_y are x and y axis projections of the cross-correlation peak width estimated using least square elliptic gaussian fit and are almost similar even if the cross-correlation peak is rotated. A further analysis with average diameter $\bar{D} = (D_x + D_y)/2$ has shown negligible changes with respect to the present result. Hence in equations (11) and (13), we use \bar{D} as the preferred diameter of the convolving Gaussian function.

In step d (Figure 2.2d), the estimated $P_{x'}$ and $P_{y'}$ are projected from x', y' on to x and y axis. The uncertainty or standard deviation (P_x, P_y) is obtained by dividing the pdf diameter by 4 (equation (14)).

$$\begin{aligned} P_x &= \frac{1}{4} \sqrt{\cos^2 \alpha P_{x'}^2 + \sin^2 \alpha P_{y'}^2} \\ P_y &= \frac{1}{4} \sqrt{\sin^2 \alpha P_{x'}^2 + \cos^2 \alpha P_{y'}^2} \end{aligned} \quad (14)$$

Westerweel [19] has shown that distribution of non-uniform displacements within a correlation window in a shear flow stretches the cross-correlation peak and adds a bias error. The stretch in the estimated standard deviation due to velocity gradient is corrected using equation (15) as mentioned in Scharnowski et al.[17] (Figure 2.2e):

$$\begin{aligned} P_x^c &= \sqrt{P_x^2 - \frac{D_p^2}{16} \left(\frac{\partial V_x}{\partial y} \right)^2} \\ P_y^c &= \sqrt{P_y^2 - \frac{D_p^2}{16} \left(\frac{\partial V_y}{\partial x} \right)^2} \end{aligned} \quad (15)$$

Here D_p represents an equivalent particle image diameter which is obtained by dividing the mean of the estimated cross-correlation peak diameter (\bar{D}) by $\sqrt{2}$ and is consistent with the formulation defined in Scharnowski et al[17]. The corrected standard uncertainty (P_x^c, P_y^c) estimate thus obtained is much higher than the true uncertainty and requires a scaling factor. Assuming a Gaussian distribution for the PDF of displacements, the mean of the distribution represents the estimated velocity for the correlating interrogation windows. Since we are trying to estimate the standard uncertainty of the mean statistic, it is expected to be scaled down by the square root of the number of samples contributing to the distribution, conforming with the definition of standard error of a statistic. In this case the uncertainty is found to be appropriately scaled by the effective number of pixels (N_{eff}) correlating to produce the primary peak (Figure 2.2f). This factor is calculated by estimating the Mutual Information or MI [8] between the correlating windows. The MI is defined as the ratio of the cross correlation plane peak magnitude to the autocorrelation peak magnitude of one ‘‘average’’ particle and is equivalent to $N_I F_I F_O N_\Delta$ (product of N_I : number of particles in the window, F_I : fraction of particles lost due to in plane

motion, F_0 : loss of correlation due to out of plane motion and N_Δ : loss of correlation due to local velocity gradients), which is just the number of particles contributing to the correlation. The “average” particle is constructed as a 2D Gaussian with maximum intensity equal to the geometric mean of the maximum intensities in the correlating interrogation windows. Also, the diameter in x and y direction for constructing the particle is taken as the geometric mean of the particle image diameter, in each of x and y direction, estimated using a 3-point Gaussian subpixel fit of the auto-correlation of the first and second interrogation windows. Thus, once MI is estimated, assuming a circular particle with area of $\frac{\pi}{4}D_p^2$, we define $N_{eff} = MI * \frac{\pi}{4}D_p^2$. Equation (16), then represents the standard uncertainty in x direction.

$$\sigma_x = \frac{P_x^c}{\sqrt{N_{eff}}} = \frac{P_x^c}{\sqrt{MI * \frac{\pi}{4}D_p^2}} \quad (16)$$

The estimated D_p can be influenced by the same error sources affecting the estimated PDF diameter P_x^c . However, an uncertainty propagation of equation (16) shows an order of magnitude less influence of any variance in D_p ($\sigma_{D_p}^2$), compared to the variance in P_x^c ($\sigma_{P_x^c}^2$). Hence, the normalization with N_{eff} is much less sensitive to any variation in D_p and therefore this variation can be ignored in the scaling term. In the last step (Figure 2.2g), we add a bias correction term to the random uncertainty estimate to get the overall standard uncertainty. In a multi-pass converged PIV processing, the shift between the two images should ideally be zero, which implies the estimated PDF distribution should have a peak at zero. Thus, a non-zero peak location at X_c, Y_c is considered a bias in the uncertainty estimate and can be attributed any source of systematic error, namely velocity gradient, loss of pair etc. Hence, bias in x direction is calculated as $\mu_x = X_c$ and the final MC method standard uncertainty, σ_x^{MC} is given by equation (17).

$$\sigma_x^{MC} = \sqrt{\sigma_x^2 + \mu_x^2} \quad (17)$$

Similarly, σ_y^{MC} can be estimated. To incorporate a PDF that is non-Gaussian because of velocity gradients, further analysis of the convolution of a skew-normal distribution and a normal distribution can be performed to analytically estimate the bias. However, this is not included in the current methodology. It is important to note that the final uncertainty estimate of the velocity is in

turn a function of the gradient of the velocity field through equation (15). Thus, a higher order differencing scheme may be preferred if the gradient correction term makes a significant difference to the uncertainty evaluation. However, for the wide range of experimental and synthetic cases tested in here, the 4th order noise optimized compact Richardson scheme[20] did not show any difference compared to a second order central difference scheme. Hence the latter is used as a best compromise between simplicity and reduction in bias and random error.

2.3 Results

The methodology was first tested with synthetic images with varying magnitudes of several common error sources (section 2.3.1). The framework was also compared with IM and CS methods for more challenging flow cases in section 2.3.2. The details of the performance are given in the following sections.

2.3.1 Variation with elemental error sources

To evaluate sensitivity of the proposed algorithm to the primary PIV error sources, a set of artificial images were generated for a range of varying parameters. For the baseline conditions, images of 1024 by 1024 pixels size were generated with a seeding density of 0.05 particles per pixel (ppp) and particle image size of 2.6 ± 0.13 pixels. The particle images were rendered within a 30 pixels wide uniform light-sheet, with 1% background noise, zero out-of-plane motion and uniform x and y displacements of 0.3 and 0.6 pixels respectively. For the individual cases, one parameter was varied at a time. The range of the parameters are as follows: displacement from 0 to 2 pixels in steps of 0.1 pixel, particle image diameter from 0.5 to 8 pixels in steps of 0.5 pixels, the y -shear rate was varied from 0 to 0.15 pixels/frame/pixel in steps of 0.025, background noise from 0.5 to 15% of maximum intensity with an increment of 1%, seeding density in the range of 0.005 to 0.15 ppp and the out-of-plane motion was varied from 0 to 40% of the light sheet thickness. For the shear case the image size was chosen as 256 by 4096 pixels to avoid large displacements at the edges in y -direction and to have same total number of vectors as in other cases.

The images were processed using in-house open source code Prana [21], with three different window sizes of 48x48, 64x64, and 128x128 pixels. In each case the windows were masked by a 50% Gaussian filter [22], such that the effective window resolutions (WR) were 24,

32, and 64 pixels respectively. For processing multi-pass iterative window deformation was used with a Standard Cross-Correlation (SCC). For each case the RMS error was compared to the RMS of the standard uncertainty estimate, obtained using the MC method. For each value of the varying parameter a pair of images were correlated, and the velocity vectors obtained for each grid point were used as samples to generate the statistical comparison of error and uncertainty. Each RMS value was calculated over 4096 samples for WR 32 and WR 64 cases, and over 7225 samples for WR24 case to ensure a minimum of 50% window overlap.

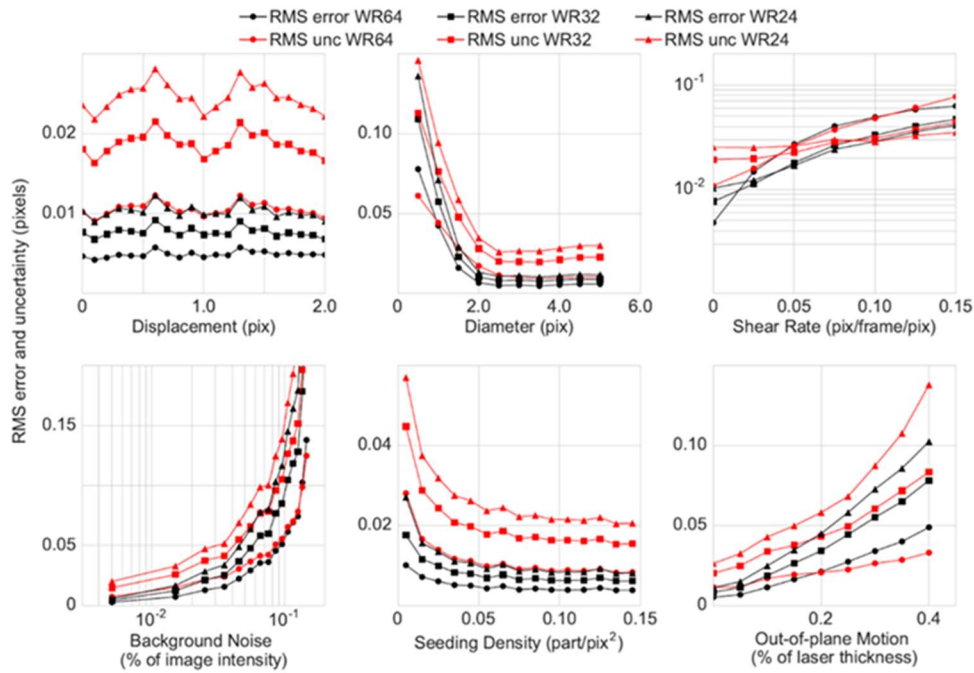


Figure 2.3. Sensitivity of MC method to primary PIV error sources for three different window resolutions (24, 32 and 64).

Figure 2.3 shows the variation of the MC uncertainty estimate with primary PIV error sources. In each case the RMS error is denoted by the black line and the predicted uncertainty by the red line. The triangular, square, and circular symbols denote the WR24, WR32 and WR64 cases respectively. For ideal prediction the RMS values of the error and predicted uncertainty should match perfectly. In this case, the MC method predicted uncertainty faithfully follows the RMS error trend and shows good sensitivity to the elemental PIV error sources. However, a bias of the order of 0.01 to 0.02 pixels is noticed in each case. For a given window resolution, the magnitude of the bias does not increase with an increase in the RMS error (even up to 0.1 pixels) as observed in the case of smaller particle image size or diameter, higher background noise and

out-of-plane motion. The bias remained about 0.02 pixels for each of the smaller window resolution cases (WR24 or WR32), while the degree of bias is slightly smaller for WR64. This can be attributed to some bias in the estimate of the normalization factor N_{eff} in the MC algorithm. Also, for bigger windows there are more effective correlating pixels, which statistically reduces the uncertainty on the sample mean. However, the level of overprediction in the MC uncertainty did not increase significantly between WS32 and WS24 cases. Although, previous studies with CS and IM methods have shown a similar trend of increasing bias with a smaller window resolution, the absolute magnitude of the bias for the MC method is relatively higher compared to the CS and IM predictions shown in the literature. The degree of bias is worse for the synthetic flow fields with small levels of RMS error compared to the various flow cases presented in section 2.3.2. Overall, the response of the predicted uncertainty to the different error sources and its close agreement with the RMS error validates the MC method as a planar PIV uncertainty measurement tool.

2.3.2 Evaluation for complex flow fields (simulated and experimental test cases)

The MC framework was further tested for complex flow cases and the uncertainty estimates were compared with IM and CS predictions for each case. A total of five datasets were used. Two synthetic datasets, namely the Turbulent boundary layer (TBL) images from 2nd PIV Challenge (2003, Case B) [23] and the Laminar Separation Bubble (LSB) flow images with varying signal to noise ratio from 3rd PIV Challenge (2005, Case B) [24], were evaluated. Also, three experimental datasets of canonical flows were used for this analysis (cases C to E in Table 2.1). The details about the Stagnation Flow (SF) data can be found in Charonko et al. [5]. The Vortex Ring (VR) data is the central camera images of the case E in fourth PIV challenge [25]. Finally, the Jet Flow (JF) image set is taken from the same experiment as described in the “unsteady inviscid core” case of the collaborative uncertainty framework by Sciacchitano et al. [11]. The details of the experiment can be found in the description of the experimental database by Neal et al.[26]. In each case the error analysis was done using a true solution, the details of which can be found in respective publications.

The images were processed using SCC with iterative window deformation for two different settings of window resolutions, WS1 and WS2, as described in Table 2.1. WS1 setting refers to a bigger final pass window resolution compared to WS2 setting. The PIV processing was done using

Prana and DaVis 8.2, with MC and IM methods implemented in Prana and CS estimates obtained through DaVis. The number of passes and window overlap setting for each case are mentioned in Table 2.1.

Table 2.1: Description of test cases and processing parameters

	Case A	Case B	Case C	Case D	Case E
	Turbulent boundary layer (TBL)	Laminar separation bubble (LSB)	Stagnation flow (SF)	Vortex ring (VR)	Jet flow (JF)
WS1 (% Overlap, No. of passes)	64x64 (75%,2) (87.5%,2)	64x64 (75%,4)	64x64 (75%,4)	64x64 (75%,1) (87.5%,3)	32x32 (87.5%,4)
WS2 (% Overlap, No. of passes)	64x64 (87.5%,1) 32x32 (75%,3)	64x64 (75%,1) 32x32 (50%,3)	64x64 (75%,1) 32x32 (50%,3)	64x64 (87.5%,1) 32x32 (75%,3)	32x32 (75%,1) 16x16 (75%,3)

The final pass was processed without any validation or smoothing. Also, measurements with absolute error greater than 1 pixel were considered invalid and removed from any statistical analysis presented in the results. The following sections describe the overall error and uncertainty histogram, the agreement of the RMS error and uncertainty prediction, spatial variation of predicted uncertainties, and the uncertainty coverage obtained for each case in the test matrix using MC, IM and CS methods.

2.3.2.1 Error and uncertainty histogram

Figure 2.4 shows the error and uncertainty histogram analysis for all the test cases. The error (\vec{e}) is defined as the deviation of the velocity evaluations (\vec{V}^{est}) from the true solution (\vec{V}^{true}) as shown in equation (18), where i goes from 1 to total number of measurements N_T .

$$\frac{1}{e} = \frac{1}{V^{est}} - \frac{1}{V^{true}} \Rightarrow e_i = V_i^{est} - V_i^{true} \quad (18)$$

For each case, all the x and y measurement error values are lumped into a single error vector of length N_T . The total number of elements (N_T) in the error vector is the product of total number of grid points in x and y ($N_x \times N_y$) times the number of frames (N_f), which is again multiplied by 2 to account for x and y values i.e. $N_T = 2N_xN_yN_f$. The root mean squared (RMS) error is defined by equation (19) as:

$$RMS(e) = \frac{1}{N_T} \sqrt{\sum_{i=1}^{N_T} e_i^2} \quad (19)$$

Similarly, for each case, the standard uncertainty values (σ_i^{MC}) evaluated using MC method is lumped into a vector of length N_T and the RMS of the uncertainty vector is evaluated as

$$RMS(\sigma^{MC}) = \frac{1}{N_T} \sqrt{\sum_{i=1}^{N_T} (\sigma_i^{MC})^2} \quad (20)$$

Equation (20) can be written for IM and CS method in an analogous way. The error and uncertainty vectors are divided into 40 and 60 bins respectively, for each case, and the percentage of measurements falling within each bin is evaluated. The percentage count of measurements in each error bin is plotted as an error histogram in Figure 2.4a and similarly an uncertainty histogram is shown in Figure 2.4b.

In Figure 2.4a, the error distribution is shown for cases A to E and for both WS1 and WS2 processing. The solid and the dashed black lines denote the errors obtained using Prana (e_{Prana}) and DaVis (e_{DaVis}) respectively. Figure 2.4b shows the uncertainty histogram for MC, IM and CS methods, overlaid on each other and are denoted by σ^{MC} , σ^{IM} and σ^{CS} respectively. Uncertainty distributions are plotted only on the positive x-axis, assuming a symmetric uncertainty curve bounds the error histogram on the negative x-axis. This assumption is correct for these cases, as the error histogram is symmetric about zero with a maximum bias of -0.015 pixels observed for case D. Ideally, the predicted uncertainties should be a delta function at the RMS error value. However, because of the inherent uncertainty in the estimation process due to limited number of correlating pixels, and the variation of the underlying uncertainty distribution of the parent population for each new measurement, the estimated uncertainties show a distribution with its peak

near the RMS error value and its spread being inversely proportional to the number of pixels or window size. The uncertainty histogram for MC, IM and CS methods are plotted together with red, cyan and violet colors respectively. The CS uncertainty distribution for the laminar separation bubble (case B) shows multiple peaks, which may be an effect of the decreasing signal to noise ratio in those images. However, the error distribution does not show multiple peaks in its distribution and likewise the MC uncertainty prediction also shows a single peak in the histogram. For the stagnation flow case (case C), all three methods show two distinct peaks in their distribution, owing to the different x and y systematic uncertainty values plotted together. The systematic uncertainties in this case are introduced due to fitting the true solution to the measurement grid, as mentioned in Charonko et al.[5]

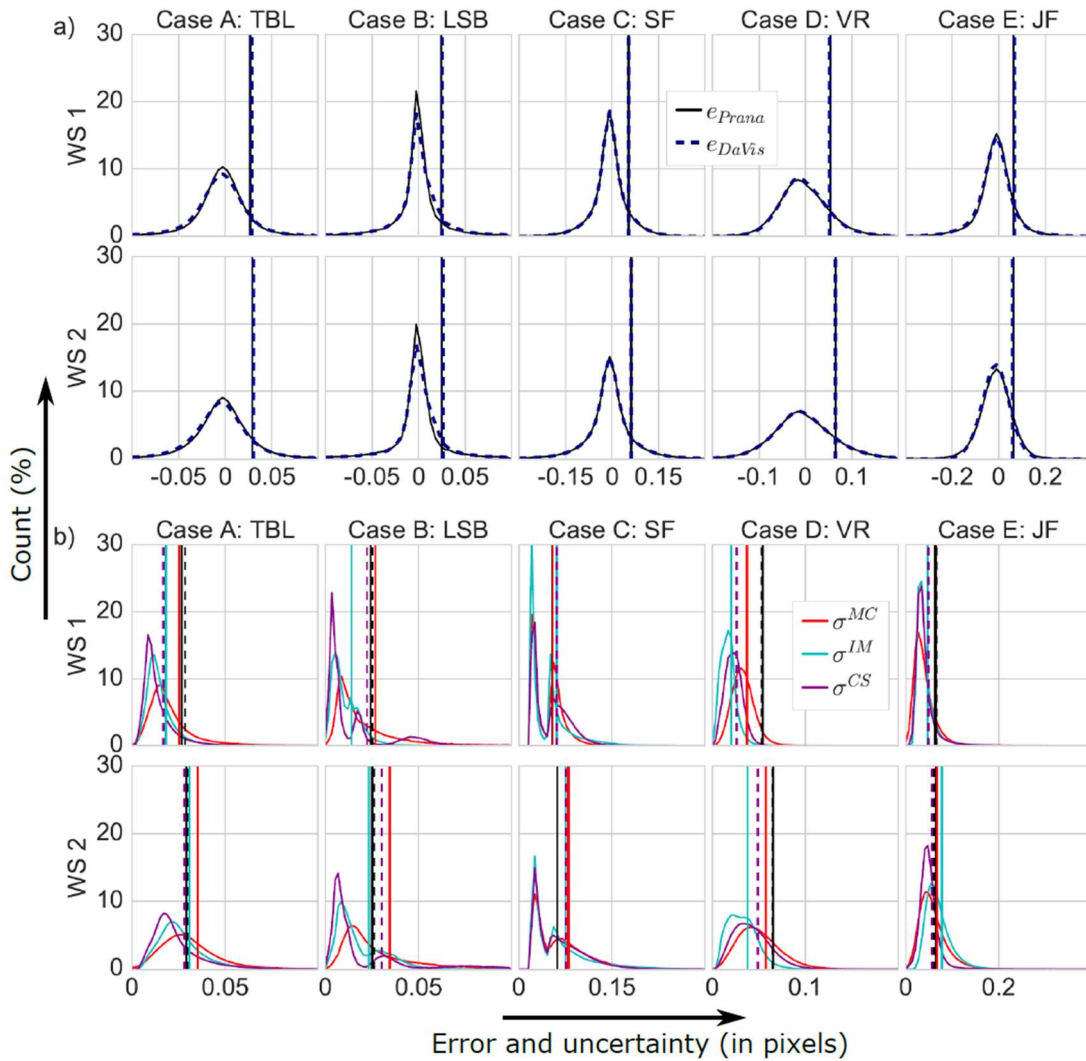


Figure 2.4. Error and uncertainty histogram comparing MC, IM and CS performance for the five test cases.

The vertical lines show the RMS values of the error and uncertainty distributions. The basis of comparison is that, for an ideal prediction, the RMS of error and uncertainty distributions should match each other [11]. Thus, the RMS error lines in Figure 2.4a are repeated in Figure 2.4b for ease of comparison. The vertical RMS error lines for Prana and DaVis match each other nearly perfectly with a maximum difference of less than 0.01 pixels. The violet dashed line (RMS of σ^{CS}) should be compared to the black dashed line (RMS of e_{DaVis}), while the solid red (MC) and the cyan (IM) vertical lines should be compared to the Prana RMS error (solid black). However, since the RMS errors are almost identical, the RMS uncertainties can be compared with respect to each other as well. For ease of comparison, Table 2.2 lists the RMS values of error and uncertainty distributions for all test cases. The predicted uncertainties reasonably match the RMS error with a maximum deviation of about 0.02 to 0.03 pixels for the experimental cases (SF, VR and JF). For the synthetic cases (TBL and LSB) the RMS uncertainties are within ± 0.01 pixels of the RMS error values. The RMS of e_{Prana} and e_{DaVis} are about 0.03 pixels for cases A and B, while it is higher (0.05 to 0.07 pixels) for the experimental cases (case C, D and E). For the vortex ring (case D), all the methods under predict the standard uncertainty while in other four cases, depending on the processing, the RMS uncertainties are seen to both underestimate and overestimate the RMS error (Table 2.2). Since the reference solution for the VR case was obtained using a multi-camera tomographic reconstruction, the planar (front on) camera image processing may incur some bias error with respect to the “true” solution. Such a systematic error can influence the consistent underprediction of the estimated uncertainties.

The methods show differences in their predictions for the WS1 and WS2 settings (Figure 2.4). With the WS1 setting, the RMS error and the RMS uncertainty predicted using MC method closely match each other for cases A, B, and C, but the RMS estimation under predicts the true errors for cases D and E. In contrast, for this window resolution the CS and IM methods under predict the RMS error in cases A and D and match the MC estimates in other cases. For the WS2 setting, however, MC method over predicts the RMS error for cases A, B, and C but matches the RMS error closely for cases D and E. In this window resolution, the CS and the IM estimates match the RMS error closely for case A and E. Generally, the IM and CS distributions show a better agreement with each other compared to MC, however, if the basis of comparison is the agreement between RMS error and RMS of uncertainty values, the MC method successfully predicts the velocity uncertainty. Overall, all three methods closely predict the correct standard

uncertainty with MC method doing a better job in cases A, C, and D for the WS1 setting and cases D and E with the WS2 processing.

Table 2.2. Comparing the RMS error and uncertainty values across different methods for the five test cases.

	RMS (Pixels)	Case A: TBL	Case B: LSB	Case C: SF	Case D: VR	Case E: JF
WS1	e_{Prana}	0.027	0.024	0.053	0.054	0.064
	σ^{MC}	0.025	0.027	0.055	0.037	0.047
	σ^{IM}	0.018	0.014	0.061	0.020	0.047
	e_{DaVis}	0.028	0.025	0.053	0.053	0.065
	σ^{CS}	0.017	0.022	0.061	0.026	0.048
WS2	e_{Prana}	0.029	0.025	0.062	0.065	0.064
	σ^{MC}	0.035	0.034	0.079	0.057	0.067
	σ^{IM}	0.031	0.023	0.075	0.038	0.077
	e_{DaVis}	0.030	0.026	0.062	0.065	0.060
	σ^{CS}	0.028	0.030	0.075	0.049	0.056

2.3.2.2 Predicted vs expected uncertainty

The predicted uncertainties have a distribution and not a single value due to an inherent uncertainty in the PIV uncertainty estimation. This is attributed to the degree of overlap between correlating particles [10]. Thus, to analyze the distribution of uncertainty the uncertainty values are divided into 8 bins, and for measurements falling in each bin the RMS error and uncertainty values are plotted. Figure 2.5 shows a direct comparison between the RMS error or the expected uncertainty

versus the predicted uncertainty for each method. For an ideal prediction the graph should be a line with slope equal to 1. The deviation from black dashed line in the plots is indicative of the amount of failure in each prediction. Hence, when the predicted uncertainties lie below and to the right of the 1:1 reference line, the predicted uncertainty estimate is under-predicting the true error distribution, and when it is above and to the left the true errors are smaller than the prediction. For the WS1 processing, the MC method closely follows the dashed line, especially for cases A to C. However, the deviation increases for higher uncertainty bins. For the first two cases the σ^{IM} and σ^{CS} under predict the 1:1 line for the lower uncertainty values but do a better job for WS2 processing. For case C, all three methods show perfect agreement in the lower uncertainty bins as opposed to the higher uncertainty bins, where σ^{MC} prediction is better compared to the other methods. In case D, all the methods under predict the true error distributions line. Thus, Figure 2.5 shows that the predicted uncertainty distributions match the RMS error closely over the whole range, except for some deviation in the higher uncertainty bins. Comparing these results to Figure 2.4a, it can also be seen that the regions of greatest deviation between the predicted uncertainty and true errors lie in the tails of the error distribution where there are much fewer samples to draw from, and thus the statistical estimates are more sensitive to outliers.

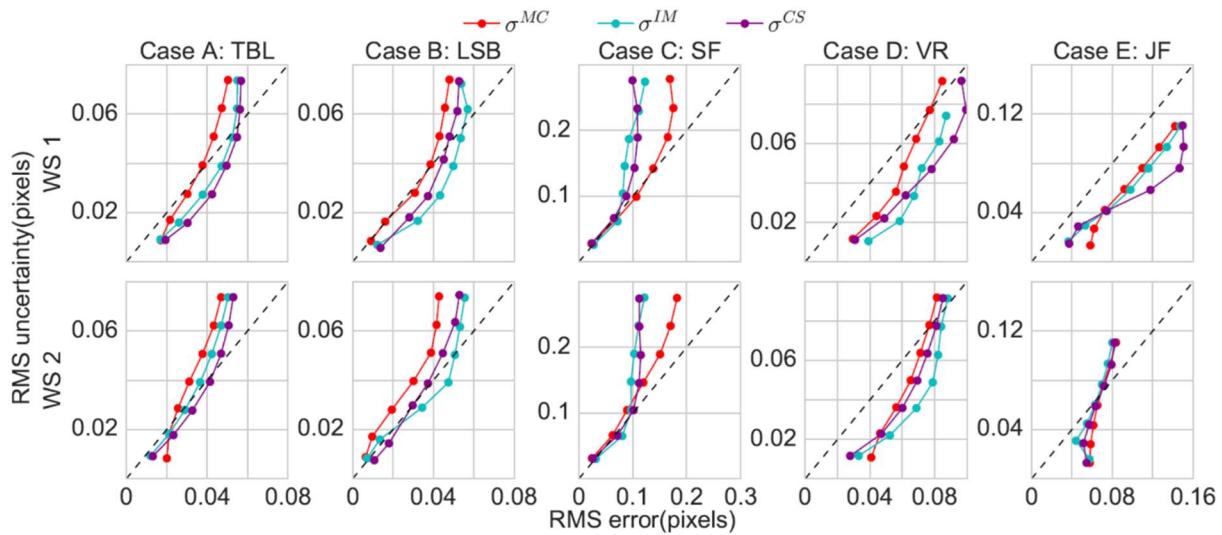


Figure 2.5. Comparing RMS error versus RMS of the predicted uncertainty for each method (MC, IM and CS) for the five test cases.

2.3.2.3 Spatial variation in RMS error and uncertainty

The spatial variation in RMS error and RMS uncertainty for a specific location in the flow field is analyzed. A specific x or y grid coordinate value is used to select a vertical or horizontal line cutting across the flow field and then the RMS of the error and uncertainty values (for x -component of velocity) across the time series is plotted along that line as shown in Figure 2.6. In each RMS value calculation, any measurement with error greater than 1 pixel is considered as invalid and not taken into account. In Figure 2.6, the left column represents the spatial profiles for WS1 processing and the middle column shows the WS2 processing results for each of the five test cases. The rightmost column depicts the mean velocity magnitude contours, obtained using Prana WS2 processing, with an overlaid dashed line indicating the spatial slice location for the RMS profiles. The numbers (0,1) or (-1,1) correspond to the normalized spatial coordinates shown in the abscissa of the RMS profiles in the first two columns. For cases A to C, a vertical line (x value set equal to the midpoint) along the middle of the grid of vectors is selected. Specifically, for case B, the lowest SNR case is not included as it increased the noise level in the RMS spatial profiles without adding any significant trend in the comparison.

For case D, a horizontal line through the top vortex core is selected. For the jet flow case, a vertical line cutting across the horizontal jet and towards the right-hand edge (downstream of the jet at $x=380$ pixel of the true solution grid) is selected. For case A, higher error and uncertainty values are noted near the wall (normalized coordinate 0). In this case the MC method is seen to be more sensitive to the spatial variation in the RMS error. For the laminar separation bubble case (case B), the RMS is taken across the decreasing SNR cases. The MC method shows better sensitivity to the spatial variation but over predicts the standard uncertainty for the WS2 processing (smaller windows). For the stagnation flow (case C), due to 3D flow and high shear rates near the wall, at near wall normalized coordinate 1 the error and uncertainty values reach about 0.1 pixels. The vortex ring case (case D), shows high fluctuations in error values near the vortex core at location 0.5. For both cases C and D, all three methods show reasonable variation corresponding to the error curves, however, the MC method clearly shows higher sensitivity to the error peaks. Finally, for the case E, the uncertainty curves show poor response for all methods in the shear layer region for WS1 processing with larger final interrogation windows. For the smaller window resolution (WS2) the IM and the MC method matches the RMS error curve and shows good sensitivity to variation in spatial error, but CS method shows lesser response to the error peaks in

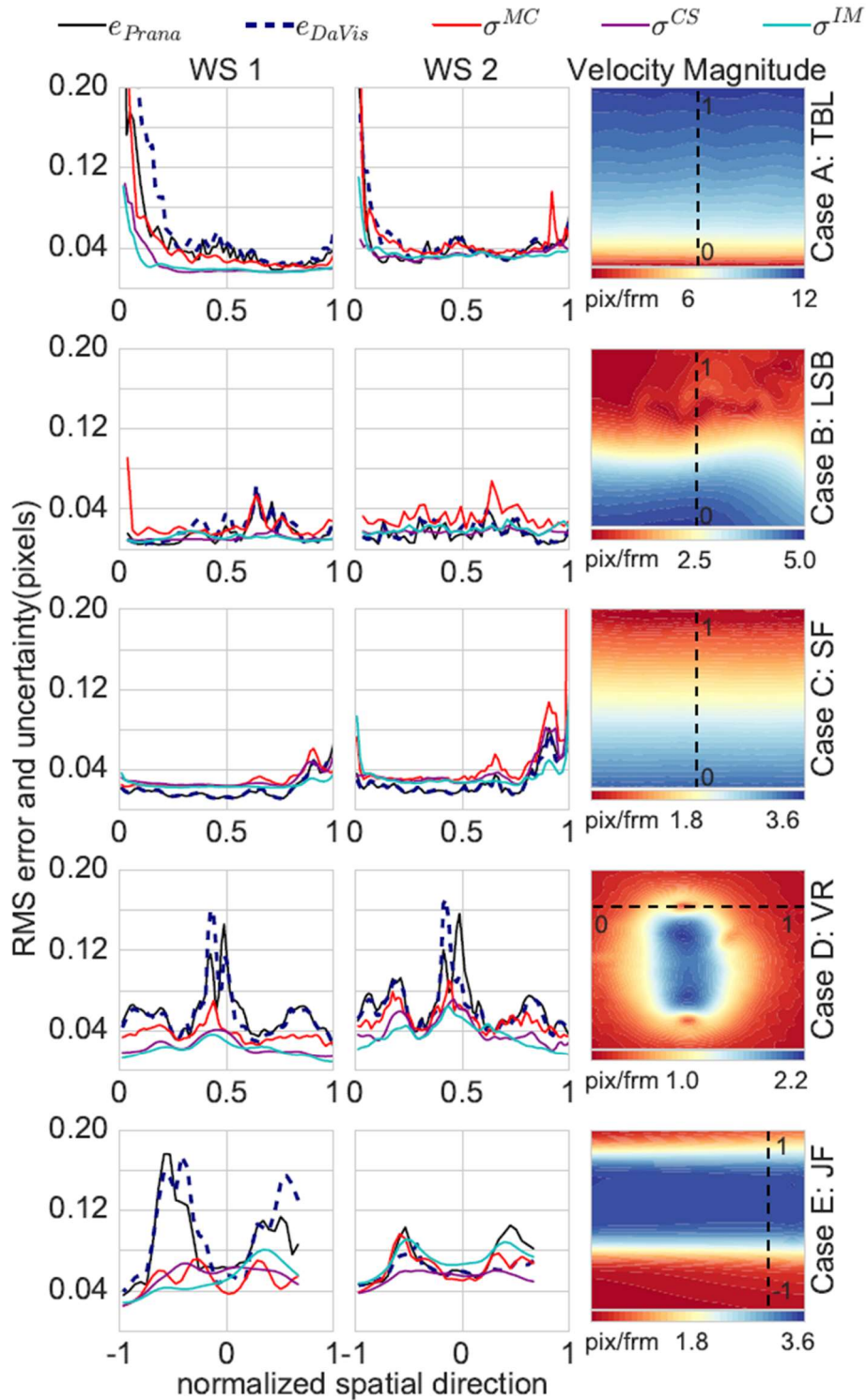


Figure 2.6. Comparing the spatial variation in RMS error and the RMS of the estimated uncertainties using MC, IM and CS methods for the different test cases. Column 1: WS1 processing, Column 2: WS2 processing and Column 3: Mean velocity magnitude contours with a dashed line indicating the slice from which the spatial profile is extracted.

the shear-layer. Overall, the MC method shows better sensitivity to the spatial variation in the RMS error for all the cases.

2.3.2.4 Uncertainty coverage

Another measure of successful uncertainty prediction is the uncertainty coverage, which denotes the percentage of measurements for which the error lies within the uncertainty bound. For a Gaussian error distribution, this should be ideally 68.5%. However, the error distribution can deviate from a Gaussian distribution and since coverage by definition is the fraction of measurement errors falling within $\pm\sigma$ (standard deviation) of the error distribution, such a measure is independent of any specific type of distribution for the error. The target coverages are thus calculated from the true error distributions without the assumption of normality and are shown as small black squares in Figure 2.7. Figure 2.7a) demonstrates the coverage values for each method and for all the different flow cases separately, while Figure 2.7b) shows the expected and predicted coverage bars combined across all the different flow cases, for WS1 and WS2 processing. The expected or target coverage for all cases is between 69% and 81%, with the VR case expected coverage (square markers) being closest to the 68.5% mark. Expected values higher than 68.5% indicate that the true error distributions are less compact than Gaussian and have longer tails. The WS2 processing is denoted by the hatched bars for each method. In general, the WS1 processing shows a lower coverage for all cases except for the case C, meaning the uncertainty is being underestimated. For the vortex ring case (case D), all the methods show a reduced coverage of about 26% to 55%, with MC performing better compared to IM and CS. This could indicate a failure of the uncertainty estimate or suggest a systematic bias in the reference solution which was derived from an auxiliary tomographic PIV measurement. For the cases A and B, the IM and CS methods under predict the coverage for WS1 processing, whereas MC method predicts a coverage of around 62% and 78%, respectively, the latter almost matching the true target coverage of 81%. For TBL and LSB cases with WS2 processing, MC method perfectly matches the expected coverage of 75% for the first case and over-predicts the expected coverage of 81% by about 9% for the second case. In contrast, IM and CS methods yield a coverage of 68% and 60% for case A (expected coverage 73%) and 73% and 63% for case B (expected coverage 81%), with WS2 processing. For the jet case (case E) the, the predictions for WS2 show better coverage compared to the WS1 processing, with IM method predicting the closest coverage match (71%). For the

stagnation flow case, all the methods successfully predict a coverage of about 72% to 77%, which is at worst within 4% of the expected coverage (76%).

Figure 2.7b) compares the uncertainty coverage over all the measurement points, irrespective of any particular flow characteristics, emphasizing on the statistical performance. The plot clearly brings out that for each window size processing, the MC method predicts the target coverage the closest as well as the fact that, WS2 processing in general yielded higher coverage compared to WS1 processing. It should be noted that the coverage does not capture the local variation in uncertainty prediction that was discussed earlier, however in an overall statistical sense better coverage usually indicates a better prediction and is a useful benchmark.

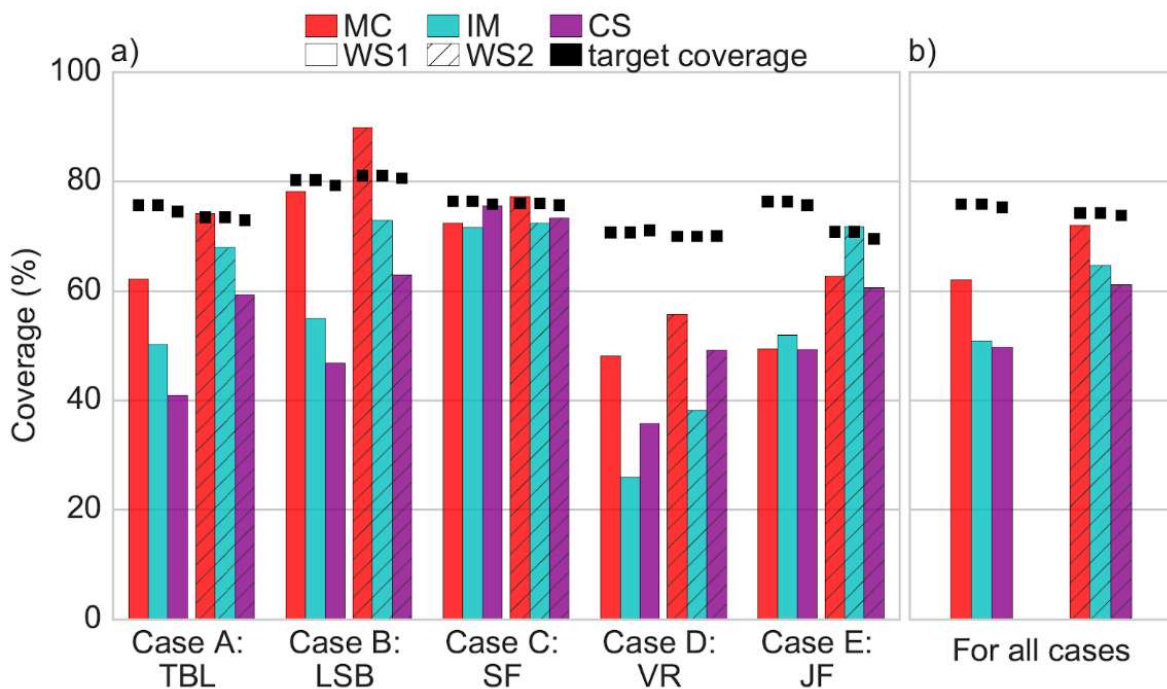


Figure 2.7. Grouped bar chart for standard uncertainty coverage using MC, IM and CS methods for WS1 and WS2 processing. a) for different flow test cases, b) for all cases combined. The target coverages calculated from the true error distributions are shown as black squares for each case.

2.4 Conclusion

A framework to extract the PIV uncertainty directly from the cross-correlation plane is provided herein. The PDF of all possible displacements that influence the final velocity prediction is first extracted from the instantaneous PIV correlation plane; this PDF is then convolved with a suitable

Gaussian to reliably estimate the PDF diameter. The standard uncertainty is then determined using a least-squared Gaussian fit on the primary peak region of the convolved Gaussian plane accounting for any peak stretching or rotation. The final estimate is normalized by the effective number of pixels contributing to the cross-correlation peak. The present method shows strong agreement with the RMS error trends for each primary PIV error source. Further analysis with more complex flows revealed good agreement with the expected uncertainty distributions. For test cases A, B, C and D, with WS1 processing, the proposed method gave a better prediction of the RMS error compared to the existing IM and CS methods. However, for lower window sizes (WS2 processing) the MC method over-predicted the standard uncertainty for the first two cases compared to the IM and CS estimates. The MC method showed better sensitivity to spatial variation in error compared to IM and CS methods for all cases. The standard uncertainty coverage predicted by the MC method was higher than the IM and CS method coverage, for most of the cases. A bias error of about 0.02 pixels was noticed for the MC method in the simulated cases. This bias error may be related to any bias in the estimated number of correlating pixels or in difficulty in sizing extremely small PDF peaks. Overall, after analyzing a wide range of test cases and the sensitivity of the predicted uncertainty to the variation in error sources, the MC method establishes itself as successful planar PIV uncertainty prediction tool and provides a framework to estimate cross-correlation uncertainty even in 3D cross-correlation.

Acknowledgements

We would like to acknowledge Dr Andrea Sciacchitano of Delft University and Dr Douglas Neal of LaVision for providing the experimental jet flow dataset. We also want to thank Dr Sciacchitano for his Image Matching code.

This research was partially supported by the National Science Foundation (PoLS-1205642, CBET-1336038, and IDBR-1152304).

2.5 References

- [1] R. J. Adrian, “Twenty years of particle image velocimetry,” *Exp. Fluids*, vol. 39, no. 2, pp. 159–169, Jul. 2005.
- [2] R. J. Adrian and J. Westerweel, *Particle Image Velocimetry*. 2011.
- [3] M. Raffel, C. E. Willert, S. T. Wereley, and J. Kompenhans, *Particle Image Velocimetry: A Practical Guide*, vol. 2nd. 2007.
- [4] B. H. Timmins, B. W. Wilson, B. L. Smith, and P. P. Vlachos, “A method for automatic estimation of instantaneous local uncertainty in particle image velocimetry measurements,” *Exp. Fluids*, 2012.
- [5] J. J. Charonko and P. P. Vlachos, “Estimation of uncertainty bounds for individual particle image velocimetry measurements from cross-correlation peak ratio,” *Meas. Sci. Technol.*, vol. 24, no. 6, p. 065301, Jun. 2013.
- [6] A. Eckstein and P. P. Vlachos, “Digital particle image velocimetry (DPIV) robust phase correlation,” *Measurement Science and Technology*, vol. 20. p. 055401, 2009.
- [7] Z. Xue, J. J. Charonko, and P. P. Vlachos, “Particle image velocimetry correlation signal-to-noise ratio metrics and measurement uncertainty quantification,” *Meas. Sci. Technol.*, vol. 25, no. 11, p. 115301, 2014.
- [8] Z. Xue, J. J. Charonko, and P. P. Vlachos, “Particle image pattern mutual information and uncertainty estimation for particle image velocimetry,” *Meas. Sci. Technol.*, vol. 26, no. 7, p. 074001, 2015.
- [9] A. Sciacchitano, B. Wieneke, and F. Scarano, “PIV uncertainty quantification by image matching,” *Meas. Sci. Technol.*, vol. 24, no. 4, p. 045302, Apr. 2013.
- [10] B. Wieneke, “PIV uncertainty quantification from correlation statistics,” *Meas. Sci. Technol.*, vol. 26, no. 7, p. 074002, 2015.
- [11] A. Sciacchitano, D. R. Neal, B. L. Smith, S. O. Warner, P. P. Vlachos, B. Wieneke, and F. Scarano, “Collaborative framework for PIV uncertainty quantification: comparative assessment of methods,” *Meas. Sci. Technol.*, vol. 26, no. 7, p. 074004, Jul. 2015.
- [12] A. Boomsma, S. Bhattacharya, D. Troolin, S. Pothos, and P. Vlachos, “A comparative experimental evaluation of uncertainty estimation methods for two-component PIV,” *Meas. Sci. Technol.*, vol. 27, no. 9, p. 094006, Sep. 2016.

- [13] S. Scharnowski and C. J. Kähler, “Estimation and optimization of loss-of-pair uncertainties based on PIV correlation functions,” *Exp. Fluids*, vol. 57, no. 2, p. 23, Feb. 2016.
- [14] M. P. Wernet, “Symmetric phase only filtering: A new paradigm for DPIV data processing,” *Meas. Sci. Technol.*, 2005.
- [15] M. Thomas, S. Misra, C. Kambhamettu, and J. T. Kirby, “A robust motion estimation algorithm for PIV,” *Meas. Sci. Technol.*, vol. 16, no. 3, pp. 865–877, 2005.
- [16] H. W. Coleman and W. G. Steele, *Experimentation, Validation, and Uncertainty Analysis for Engineers*. Hoboken, NJ, USA: John Wiley & Sons, Inc., 2009.
- [17] S. Scharnowski, R. Hain, and C. J. Kähler, “Reynolds stress estimation up to single-pixel resolution using PIV-measurements,” *Exp. Fluids*, vol. 52, no. 4, pp. 985–1002, Aug. 2011.
- [18] A. C. Eckstein, J. Charonko, and P. Vlachos, “Phase correlation processing for DPIV measurements,” *Exp. Fluids*, vol. 45, no. 3, pp. 485–500, 2008.
- [19] J. Westerweel, “On velocity gradients in PIV interrogation,” pp. 831–842, 2008.
- [20] A. Etebari and P. P. Vlachos, “Improvements on the accuracy of derivative estimation from DPIV velocity measurements,” *Exp. Fluids*, vol. 39, no. 6, pp. 1040–1050, 2005.
- [21] “<https://github.com/aether-lab/prana/>.” .
- [22] A. Eckstein and P. P. Vlachos, “Assessment of advanced windowing techniques for digital particle image velocimetry (DPIV),” *Measurement Science and Technology*, vol. 20. p. 075402, 2009.
- [23] M. Stanislas, K. Okamoto, C. J. Kähler, and J. Westerweel, “Main results of the Second International PIV Challenge,” *Exp. Fluids*, vol. 39, no. 2, pp. 170–191, Mar. 2005.
- [24] M. Stanislas, K. Okamoto, C. J. Kähler, J. Westerweel, and F. Scarano, “Main results of the third international PIV Challenge,” *Exp. Fluids*, vol. 45, no. 1, pp. 27–71, 2008.
- [25] C. J. Kahler, T. Astarita, P. P. Vlachos, J. Sakakibara, R. Hain, S. Discetti, R. La Foy, and C. Cierpka, “Main results of the fourth International PIV Challenge,” *Exp. Fluids*, 2016.
- [26] D. R. Neal, A. Sciacchitano, B. L. Smith, and F. Scarano, “Collaborative framework for PIV uncertainty quantification: the experimental database,” *Meas. Sci. Technol.*, vol. 26, no. 7, p. 74003, 2015.

3. STEREO-PARTICLE IMAGE VELOCIMETRY UNCERTAINTY QUANTIFICATION

Sayantana Bhattacharya¹, John J. Charonko², Pavlos P. Vlachos¹

¹ School of Mechanical Engineering, Purdue University, USA.

² Physics Division, Los Alamos National Laboratory, USA.

This chapter has been previously published in Measurement Science and Technology, 28 015301.

DOI: <https://doi.org/10.1088/1361-6501/28/1/015301>

Abstract

Particle Image Velocimetry (PIV) measurements are subject to multiple elemental error sources and thus estimating overall measurement uncertainty is challenging. Recent advances have led to *a posteriori* uncertainty estimation method for planar two-component PIV. However, no complete methodology exists for uncertainty quantification in stereo PIV. In the current work, a comprehensive framework is presented to quantify the uncertainty stemming from stereo registration error and combine it with the underlying planar velocity uncertainties. The disparity in particle locations of the dewarped images is used to estimate the positional uncertainty of the world coordinate system, which is then propagated to the uncertainty in the calibration mapping function coefficients. Next, the calibration uncertainty is combined with the planar uncertainty fields of the individual cameras through an uncertainty propagation equation and uncertainty estimates are obtained for all three velocity components. The methodology was tested with synthetic stereo PIV data for different light sheet thicknesses, with and without registration error, and also validated with an experimental vortex ring case from 2014 PIV challenge. Thorough sensitivity analysis was performed to assess the relative impact of the various parameters to the overall uncertainty. The results suggest that in absence of any disparity, the stereo PIV uncertainty prediction method is more sensitive to the planar uncertainty estimates than to the angle uncertainty, although the latter is not negligible for non-zero disparity. Overall the presented uncertainty quantification framework showed excellent agreement between the error and

uncertainty RMS values for both the synthetic and the experimental data and demonstrated reliable uncertainty prediction coverage. This stereo PIV uncertainty quantification framework provides the first comprehensive treatment on the subject and potentially lays foundations applicable to volumetric PIV measurements.

Nomenclature

x, y, z	Physical or world coordinates
X, Y	Image coordinates
FX, FY	Camera calibration polynomial mapping function for X and Y image coordinates
a_i	Calibration mapping function coefficients
$FX_{x,y,z}^{1,2}$	Mapping function gradients with respect to x, y, z for each camera (1 or 2)
U, V	Planar 2D velocity field for each camera
u, v, w	Stereo 2D-3C velocity components
α	Angle in $x - z$ plane
β	Angle in $y - z$ plane
σ	Uncertainty in any variable
e	Error in any variable
d_x, d_y	Disparity field between two stereo cameras
δ_x, δ_y	Subpixel positional difference between matching particles in a PIV interrogation window.
A_j	New calibration z plane fit coefficients
b	Standard bias uncertainty component in any variable
r	Standard random uncertainty component in any variable
S_{ci}	Sensitivity coefficients for c^{th} stereo component and multiplying i^{th} elemental uncertainty
RMS	Root Mean Square

3.1 Introduction

Particle Image Velocimetry (PIV) [1], [2] is a non-invasive fluid velocity measurement technique based on cross-correlation of particle image patterns. Planar PIV velocity estimation is a complex function of several parameters like particle image size, seeding density, in-plane displacement, camera noise and out-of-plane motion. In addition to the planar PIV error sources, stereo-PIV also includes registration error, which contributes to the uncertainty in the velocity measurement. Developments in PIV over the last few decades have optimized the measurement accuracy and minimized the error from all these error sources. However, only recently has the community addressed uncertainty quantification in a planar PIV measurement. The uncertainty in stereoscopic PIV (stereo-PIV) is a combination of the planar PIV uncertainty for each camera and the uncertainty in the stereo calibration function. Although methods presently exist for quantifying planar two-component PIV uncertainty, no complete uncertainty quantification approach exists for planar three-component, stereo-PIV. The present work develops a framework for quantifying uncertainty in stereo-PIV measurements.

A number of *a posteriori* methods have been recently developed for uncertainty estimation in planar PIV. As a first approach Timmins et al. [3] built an uncertainty mapping function or “Uncertainty Surface” by varying the primary PIV error sources over a wide range. In this method once the parameters like particle image size, seeding density, shear rate and displacement are evaluated for an image pair, the mapping function can be used to predict the measurement uncertainty. In parallel effort, Charonko et al. [4] showed that the uncertainty is inversely proportional to the correlation plane primary peak to secondary peak height ratio (PPR) and used the “PPR” metric for uncertainty prediction. Xue et al. [5], [6] also quantified PIV uncertainty as a function of other correlation plane signal to noise ratio (SNR) metrics. Since there is no analytical relationship between PIV uncertainty and its error sources or the SNR metrics, these methods are sensitive to the calibration fits used for prediction. Direct, calibration-free, methods have also been developed to quantify uncertainty using a multi-pass converged velocity field. Sciacchitano et al. [7] proposed “Image Matching” (IM) where the original images are deformed using the final pass velocity field to overlay on top of each other and the RMS of the positional mismatch of particle images in each interrogation window is used as a measure of standard uncertainty. Wieneke [8] in “Correlation Statistics” (CS) linked the covariance of the pixel by pixel intensity difference of the deformed particle images to the correlation function uncertainty, which when used in the 3-point

Gaussian fit uncertainty propagation equation, yields an estimate of the displacement uncertainty. The advantages and disadvantages of each of these methods have been compared in a jet flow case with varying error sources by Sciacchitano et al. [9], [10]. Also, in another comparative evaluation the planar uncertainty methods were compared for two experimental cases (a jet flow and a cylinder in cross flow) across different processing software[11]. Both the comparisons concluded that the direct methods are more sensitive to the variation in RMS error in presence of different error sources. However, Boomsma et al. [11] showed that direct methods can under predict the standard uncertainty, even when the systematic error is negligible. Overall, the direct methods show better response to the variation in random error. Thus, here we use the direct methods (IM & CS) to estimate the planar uncertainty. We then proceed to introduce a rigorous framework for including the effect of multi-camera calibrations and stereo reconstruction on the uncertainty, and finally assess the sensitivity of the overall uncertainty in the derived stereo velocity components to each of these sources of potential error.

Stereoscopic PIV [12] was developed to resolve the out-of-plane velocity component using two angled views of the same flow field. The measurement chain includes the following procedures as shown in the block diagram in Figure 3.1.

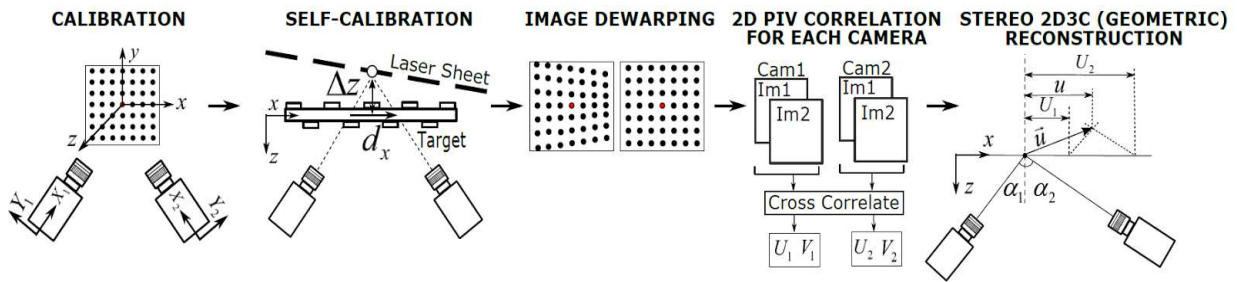


Figure 3.1. Stereo PIV measurement chain

The first step, calibration, maps the measurement domain in physical coordinates (world coordinate system) onto the camera image coordinate system using calibration target images [13]. Once the mapping function is known, individual camera images of particle fields are back-projected or dewarped onto the physical grid and cross-correlated to evaluate any mismatch or disparity between the two camera images at the same time instant. This process is known as self-calibration [14]. For perfect calibration i.e. perfect camera correspondence and no misalignment between calibration target and laser sheet position, the disparity should be zero. Self-calibration attempts to correct for any disparity by modifying the calibration mapping function coefficients or

adding additional terms. Recent analysis by Beresh et al. [15] has shown that large stereoscopic angles and thick laser sheets can introduce significant bias errors even after a converged self-calibration. The situation is worse for smaller particle image diameters and higher seeding density. Thus, any uncertainty in the evaluation of the disparity field can contribute to the uncertainty in the calibration mapping function. This corrected mapping function is then used to dewarp the individual camera images. Due to the viewing angle of the cameras the resulting images can have non-uniform magnifications. Depending on the camera overlap a common grid is selected in the physical space and the mapping function is used to determine the corresponding grid points in the image domain. The camera images are then interpolated on this new grid, which results in a constant magnification factor across the image. These dewarped images are cross-correlated for each camera, using standard planar PIV processing algorithms to yield the projected velocity components. The camera angles are estimated using mapping function gradients. Finally the projected velocity components are combined with the camera angles to yield the three velocity components (Willert et al. [16]) on the two dimensional physical grid. An alternative approach by Soloff et al. [17] does planar cross-correlation on the original camera images and then dewarps the 2D vector fields and uses them for reconstructing the stereo field. However, false vectors calculated at different world coordinate positions can corrupt interpolation and lead to erroneous stereo reconstruction. This approach also leads to varying spatial resolution across the field of view as the vector fields are dewarped and not the images. This is more significant for cameras placed on two sides of the laser sheet, in which case, stereo reconstruction is performed with planar displacements having different spatial resolution and uncertainties. This method is not considered herein.

The complexity of the measurement chain presents a challenge for quantifying the elemental uncertainties at each step of the process and determining how the uncertainty in the calibration step propagates into the uncertainty in the viewing angles and in turn in the stereo reconstruction. Although it has been shown that the out-of-plane velocity component RMS error is a strong function of the camera angle, such work has not considered any uncertainty in calibration or angle estimation [18], [19]. The present framework, for the first time, quantifies the uncertainty in each step of the measurement chain and propagates the elemental uncertainties into the reconstructed velocity components.

3.2 Methodology

The first step in stereo-PIV requires aligning the two cameras with the measurement domain through calibration. The calibration mapping function is obtained by imaging a target with precisely positioned dots and then fitting a model function between the known world coordinates and the corresponding estimated image coordinates. Typically a pinhole model [20] or a polynomial mapping function [13] is used. Here we consider a polynomial mapping function with cubic order in x and y (in plane world coordinates) and quadratic order in z (out of plane world coordinate) as shown in equation (21).

$$X = FX(a_i, x, y, z) = a_1 + a_2x + a_3y + a_4z + a_5x^2 + a_6xy + a_7y^2 + a_8xz + a_9yz + a_{10}z^2 + a_{11}x^3 + a_{12}x^2y + a_{13}xy^2 + a_{14}y^3 + a_{15}x^2z + a_{16}xyz + a_{17}y^2z + a_{18}xz^2 + a_{19}yz^2 \quad (21)$$

There are four such functions mapping each camera X and Y image coordinates to the world coordinates x , y and z e.g. FX_1, FY_1, FX_2, FY_2 and a total of $4 \times 19 = 68$ coefficients determined from calibration.

For stereo-PIV, a standard calibration process results in a small re-projection error. A more significant source of error is the “registration error” which refers to any mismatch between the dewarped camera images. Any error in the camera mapping function or misalignment between the laser sheet and the calibration plane lead to “registration error”, which results in a disparity between dewarped particle images and in turn reflects as a systematic error in the reconstructed stereo velocity field. The self-calibration process [14] corrects for the misalignment by triangulation of the disparity field to determine the world coordinate system which achieves the best correspondence between the cameras and the measurement plane. This transformed physical coordinate system is used to do another calibration fit, which results in modified mapping function coefficients. This process adjusts the camera mapping functions relative to each other and may not completely eliminate the true position error with respect to the original world coordinate system, without any further reference. Also, if only a single camera is misaligned, this process will adjust and modify both mapping functions to minimize the disparity and thus introducing error in both mapping functions. It has been shown that this self-calibration process is critical in improving the accuracy of a stereo-PIV measurement [21]. However, the uncertainty in the disparity vectors, resulting from 2D cross-correlation between the dewarped images, and its propagation to

uncertainty in the calibration coefficients as well as the world coordinate grid position have not yet been considered.

Figure 3.2 shows the uncertainty propagation from the different uncertainty sources in a stereo-PIV process. Figure 3.2 (a, b, c) corresponds to how to estimate the uncertainty in physical coordinate system and is described in Section 3.2.1. Sections 3.2.2 and 3.2.3 discuss the uncertainty in triangulated z location represented in Figure 3.2 d, e and the uncertainty in mapping function coefficients (Figure 3.2 f, g) respectively. Subsequently, the uncertainties in the angles (Figure 3.2 h) are estimated in 3.2.4. Section 3.2.5 discusses the planar uncertainty (Figure 3.2 i) for individual camera dewarped images. Finally, the planar uncertainties and angle uncertainties are combined to obtain the uncertainty of the three velocity components (Figure 3.2 j) in Section 3.2.6.

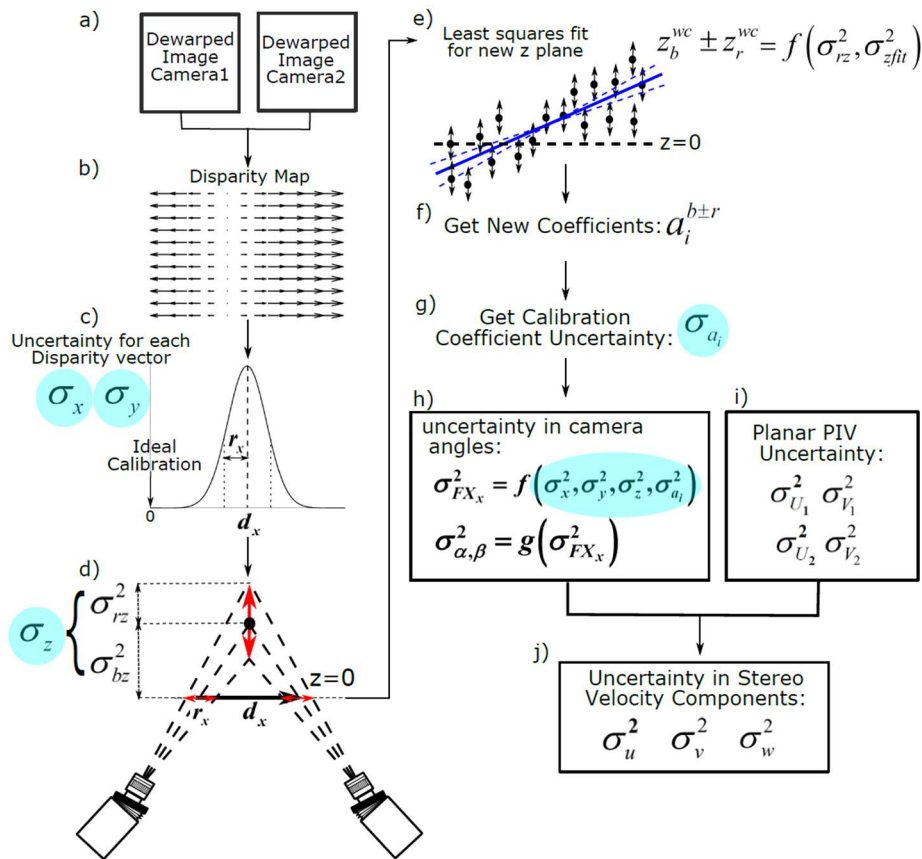


Figure 3.2. Uncertainty propagation flow chart for a stereo-PIV measurement process: (a, b, and c) correspond to how to estimate the uncertainty in physical coordinate system (d and e refer to the uncertainty in triangulated z location, and (f, g) correspond to the uncertainty in the mapping function coefficients respectively. (h, i) correspond to the uncertainties in the angles and the planar uncertainty for individual camera dewarped images. Finally, the planar uncertainties and angle uncertainties combined to obtain the uncertainty of all three velocity components (j).

3.2.1 Uncertainty in physical coordinate system

We first estimate the uncertainty in the disparity vector field (d_x, d_y) by cross-correlating the individual camera dewarped images at the same time instant (Figure 3.2a, Figure 3.2b). Ideally, for a thin light sheet (about 1mm), small observation angles and a perfect calibration the back-projected particle images should match each other and there should be zero disparity. Any misalignment or offset between the measurement plane and calibration plane leads to a disparity between the particle image locations, resulting in a biased estimate of final velocities. Moreover, due to out of plane motion the projected particle images appear at different locations on the dewarped images. This happens especially for thick laser sheets and towards the edge of the images and is also a strong function of camera working distance and the size of the field of view. To minimize this effect “ensemble correlation” is used which gives a robust estimate of the mean disparity field. In presence of any vibration, the transient disparity variation information from frame to frame is lost in the ensemble process. However, in the following method of uncertainty quantification, the variance in the instantaneous frame correlation is still captured in the random error distributions for each disparity vector. In addition, this method for estimating the uncertainty in the disparity field can work irrespective of the ensemble process. For estimating the random uncertainty associated with each disparity vector, the correlating windows are shifted towards each other by half of the estimated disparity vector (Discrete Window Offset) [22] and then for each matching particle pair the subpixel difference in their location (δ_x, δ_y) is considered. Previously, Sciacchitano et al. in their “Image Matching” method [9] have shown that the uncertainty in a 2D PIV vector can be related to the difference in particle positions of two matching image pairs. Here we apply this concept to find the positional mismatch between the particles in the individual camera dewarped images. The matching of these particle image pairs can be challenging in case of noisy images, overlapping particle images or loss-of-pairs. Suitable image preprocessing and intensity thresholding can make the particle image detection more robust. The estimated positional differences (δ_x, δ_y) for all the particle image pairs in an interrogation window and for all the windows across the ensemble image pairs are combined in a histogram and the standard deviation of the Gaussian fit to this distribution gives the random uncertainty (r_x, r_y) at that grid point, as shown in Figure 3.2c. It is to be noted that, in principle, a pixel wise matching of the dewarped images (similar to CS method) can also be used for estimating the random uncertainty, such that out-of-plane losses are taken into account.

In addition, the disparity vector itself evaluated over all the image pairs is a measure of the bias uncertainty ($b_x = d_x, b_y = d_y$), and is the error source that the subsequent self-calibration procedure attempts to remove. It is important to mention that both the bias and random uncertainty when estimated with discrete window offset, inherently assumes that both cameras equally contributed to the disparity. If small shift in one camera is the only source of bias, then it is impossible to account for that without any additional reference system. Finally, the combined standard uncertainty (contribution from both random and bias component) in world coordinate position (σ_x, σ_y and σ_z) can be expressed as follows:

$$\begin{aligned}\sigma_x &= \sqrt{b_x^2 + r_x^2}, \sigma_y = \sqrt{b_y^2 + r_y^2} \\ \sigma_z &= \sqrt{\frac{\sigma_x^2}{(\tan \alpha_1 + \tan \alpha_2)^2}} = \sqrt{\frac{b_x^2 + r_x^2}{(\tan \alpha_1 + \tan \alpha_2)^2}} = \sqrt{\sigma_{bz}^2 + \sigma_{rz}^2}\end{aligned}\quad (22)$$

The combined standard uncertainty includes the systematic uncertainty which is defined as the standard deviation of bias error distribution. Since the bias distribution is unknown in this case, we assume that the estimated disparity (bias error) approximates the uncertainty bound for the possible bias distribution one expects to see. The uncertainty in z location can be expressed through triangulation equation as a function of the stereo angles and the x or y standard uncertainty depending upon camera orientation. For the present case camera angles are considered only in $x - z$ plane (i.e. α_1, α_2 are non-zero, Figure 3.1) and only significant disparity in x was assumed. Thus in equation (22), σ_z is expressed as a function of σ_x . For non-zero $y-z$ plane angle (β_1, β_2) the σ_y uncertainty can also be propagated using the triangulation equation, in which case, both σ_x and σ_y will contribute to σ_z . Here, σ_{bz} and σ_{rz} denote the bias and the random part of the z location uncertainty (Figure 3.2d). The corresponding equations for the general case when both cameras are at an angle $\beta_{1,2} \gg 0$ in the $y - z$ plane are provided in Appendix A.

3.2.2 Uncertainty in triangulated z -plane location

The projected z coordinates obtained through triangulation are used to do a least squares plane fit ($z = A_1x + A_2y + A_3$) to find the modified world coordinate system. Equation (23) describes how the least squares fit equation is used to find the plane fit coefficients A_j as a function of z position. Here M denotes the left hand side matrix in equation (23), multiplying the plane fit coefficient

vector A and R is the right hand side column vector. Both M and R are functions of world coordinates. Also, B represents the inverse of M .

$$\begin{bmatrix} \sum x^2 & \sum xy & \sum x \\ \sum xy & \sum y^2 & \sum y \\ \sum x & \sum y & \sum 1 \end{bmatrix} \begin{Bmatrix} A_1 \\ A_2 \\ A_3 \end{Bmatrix} = \begin{Bmatrix} \sum xz \\ \sum yz \\ \sum z \end{Bmatrix} \Leftrightarrow MA = R \Leftrightarrow A = M^{-1}R \Leftrightarrow A = BR \quad (23)$$

$$A_j = \sum_i (B_{j1}x_i + B_{j2}y_i + B_{j3})z_i = \sum_i C_{ji}z_i$$

The total random uncertainty in the z coordinates for the least squares plane fit has a contribution from two sources. First, the random uncertainty on each z point originating from the uncertainty in the evaluation of the disparity vector itself i.e. $\sigma_{rz_i}^2$ from equation (22). Secondly, the uncertainty associated with the least square fit residual (e_i) which is estimated by the standard error in the fit (σ_{zfit}^2), shown in equation (24).

$$\sigma_{zfit}^2 = \frac{1}{N-p} \sum_{i=1}^N e_i^2 \quad (24)$$

Thus, using the propagation equation the uncertainty in the coefficients $\sigma_{A_j}^2$ can be evaluated using equation (25).

$$\sigma_{A_j}^2 = \sum_i C_{ji}^2 (\sigma_{rz_i}^2 + \sigma_{zfit}^2) \quad (25)$$

So we can write the corrected world coordinate plane location as $z_b^{wc} \pm z_r^{wc} = (A_1 \pm \sigma_{A_1})x + (A_2 \pm \sigma_{A_2})y + (A_3 \pm \sigma_{A_3})$, as shown in Figure 3.2e, where the solid line (z_b^{wc}) denotes the mean location of the world coordinate system and the dashed lines ($z_b^{wc} \pm z_r^{wc}$) represent the possible shifted plane locations due to the inherent standard uncertainty.

3.2.3 Uncertainty in mapping function coefficients

To determine the uncertainty in the calibration coefficients a calibration fit is done between the new world coordinate plane and the image plane for each camera. Let a_i^b be the mapping function coefficients determined by the non-linear least squares fit between z_b^{wc} and the image coordinates. Also, let $a_i^{b\pm r}$ be the coefficients obtained from calibration using $z_b^{wc} \pm z_r^{wc}$ as the world

coordinate planes (Figure 3.2f). Then we can define the bias and the random uncertainty in the coefficients using the following equations:

$$\begin{aligned}\sigma_{ba_i} &= a_i^0 - a_i^b, \sigma_{ra_i} = (a_i^{b+r} - a_i^{b-r})/2 \\ \sigma_{a_{fit}}^2 &= (J^t J)^{-1} \sigma_{res}^2 I\end{aligned}\tag{26}$$

Where, a_i^0 are the existing calibration coefficients and $\sigma_{a_{fit}}^2$ is the fit uncertainty obtained as a function of the Jacobian (J) of the residual at the solution and the variance of the fit residual error (σ_{res}^2). Thus the total uncertainty in the calibration coefficients σ_{a_i} , as shown in Figure 3.2g, can be expressed as:

$$\sigma_{a_i} = \sqrt{\sigma_{ba_i}^2 + \sigma_{ra_i}^2 + \sigma_{a_{fit}}^2}\tag{27}$$

Where σ_{ra_i} and $\sigma_{a_{fit}}$ can vary in their relative contribution, depending on the error source and its variation across the image. In general, both are dependent on the distribution of positional mismatch between each camera particle images. Since it is difficult to quantify the correlation between these random errors, they are assumed to be independent in this analysis. Neglecting the correlation between these random errors accounts for the errors twice. Thus the true uncertainty should be lower making the estimated σ_{a_i} an upper bound for the uncertainty. It is to be noted, that σ_{ra_i} reflects the local variation in particle image positions while $\sigma_{a_{fit}}$ accounts for the global variation in disparity magnitudes across the image. Equations (23) to (27) show how the uncertainty in the particle positions in the dewarped images propagate to the uncertainty in the mapping function coefficients. This method can be used to estimate the σ_{a_i} 's after calibration or self-calibration. Typically, a good calibration and converged self-calibration leads to very small value of σ_{a_i} . However, if the calibration fit residual RMS error is high or there is any remaining disparity, even after self-calibration, then σ_{a_i} can be significant.

It is to be noted that typically Scheimpflug adapters are present (as shown in Figure 3.2d) in a stereo PIV measurement to align the plane of focus with the measurement plane and thus increases the overlapping region between the cameras. Without these adapters the calibration accuracy may suffer and the self-calibration accuracy may also deteriorate because of the contribution from out-of-focus particles. This will also affect the planar correlation uncertainty.

However, the calibration and planar velocity field uncertainty is quantified in a generalized way to take into account any effect from the out-of-focus particles. A detailed analysis on uncertainty variation in absence of Scheimpflug adapters is not considered herein.

3.2.4 Uncertainty in stereo angles

The stereo angles can be calculated as a function of the mapping function gradients following Giordano et al. [23] (equation (28)):

$$\tan \alpha_1 = \frac{FY_z^1 FX_y^1 - FY_y^1 FX_z^1}{FY_y^1 FX_x^1 - FY_x^1 FX_y^1}, \tan \beta_1 = \frac{FY_z^1 FX_x^1 - FY_x^1 FX_z^1}{FY_x^1 FX_y^1 - FY_y^1 FX_x^1} \quad (28)$$

Consequently, the uncertainty in the stereo angles can be expressed as a function of the uncertainty in the mapping function gradients as shown in equation (29).

$$\begin{aligned} \sigma_\alpha^2 &= f\left(\sigma_{FX_x}^2, \sigma_{FX_y}^2, \sigma_{FX_z}^2, \sigma_{FY_x}^2, \sigma_{FY_y}^2, \sigma_{FY_z}^2\right) \\ \sigma_\beta^2 &= g\left(\sigma_{FX_x}^2, \sigma_{FX_y}^2, \sigma_{FX_z}^2, \sigma_{FY_x}^2, \sigma_{FY_y}^2, \sigma_{FY_z}^2\right) \end{aligned} \quad (29)$$

For the mapping function given in equation (21), the gradients can be analytically computed by equation (30). Similarly, the expressions for other gradients can also be evaluated.

$$FX_x = \frac{\partial FX}{\partial x} = a_2 + 2a_5x + a_6y + a_8z + 3a_{11}x^2 + 2a_{12}xy + a_{13}y^2 + 2a_{15}xz + a_{16}yz + a_{18}z^2 \quad (30)$$

Since FX_x is a function of x , y , z and a_i 's, the uncertainty in the mapping function gradients can be expressed as a function of the uncertainty in the calibration coefficients (σ_{a_i}) and the uncertainty in the world coordinate grid position ($\sigma_x, \sigma_y, \sigma_z$), as shown in equation (31).

$$\sigma_{FX_x}^2 = \left(\frac{\partial FX_x}{\partial a_i}\right)^2 \sigma_{a_i}^2 + \left(\frac{\partial FX_x}{\partial x}\right)^2 \sigma_x^2 + \left(\frac{\partial FX_x}{\partial y}\right)^2 \sigma_y^2 + \left(\frac{\partial FX_x}{\partial z}\right)^2 \sigma_z^2 \quad (31)$$

From equations (22) and (27) the values of $\sigma_x, \sigma_y, \sigma_z$ and σ_{a_i} can be evaluated. Substituting these values into equation (31) and using the evaluated uncertainties in equation (29), the uncertainty in the stereo angles can be quantified (Figure 3.2h).

3.2.5 Uncertainty in dewarped camera image cross correlation

The next step in a Stereo-PIV measurement involves dewarping the individual camera images to a common physical grid. The interpolation of the camera images is often performed using a higher order schemes such as sinc or bspline methods to ensure the reconstruction does not introduce biases into the cross correlation steps [24]. Here we have chosen to use an 8 point sinc function with Blackman apodization to balance accuracy with computational efficiency. Given a sufficiently accurate scheme, the uncertainty in dewarping is mainly a function of the uncertainty in the mapping function coefficients, which leads to interpolation of particle images at the wrong world coordinate locations and biased displacement estimates. Dewarping involves inverting the non-linear polynomial mapping function and thus analytically propagating the uncertainty is not a feasible approach, however, this error is negligible after a successful self-calibration, and therefore it is not included in this framework. Nevertheless, further future analysis could ascertain the uncertainty contribution of this step in more detail.

Cross-correlating the dewarped images yields the 2D velocity fields for each stereo camera. The uncertainty in the planar velocity fields can be evaluated using any existing planar uncertainty estimation algorithm. In this work, IM and CS methods have been used to calculate the planar uncertainties (step i) in Figure 3.2).

3.2.6 Uncertainty propagation in stereo reconstruction

Once the planar uncertainties are known and the angle uncertainties are estimated, both can be propagated through the velocity reconstruction equation to give the uncertainty in the three velocity components u , v and w (Figure 3.2j). For geometric reconstruction with cameras in the $x - z$ plane (Figure 3.1) the reconstructed velocity components are given by [16], [23]:

$$\begin{aligned} u &= \frac{U_2 \tan \alpha_1 - U_1 \tan \alpha_2}{\tan \alpha_1 - \tan \alpha_2} \\ w &= \frac{U_2 - U_1}{\tan \alpha_1 - \tan \alpha_2} \\ v &= \frac{V_1 + V_2}{2} + \frac{w}{2} (\tan \beta_2 + \tan \beta_1) \end{aligned} \quad (32)$$

The uncertainty in the u velocity component is obtained by a Taylor-series uncertainty propagation of the reconstruction equation, as shown in equation (33). The uncertainty σ_u^2 is expressed as a product of a row vector of sensitivity coefficients and a column vector of corresponding elemental uncertainties.

$$\sigma_u^2 = \frac{\partial u}{\partial U_1}^2 \sigma_{U_1}^2 + \frac{\partial u}{\partial U_2}^2 \sigma_{U_2}^2 + \frac{\partial u}{\partial \alpha_1}^2 \sigma_{\alpha_1}^2 + \frac{\partial u}{\partial \alpha_2}^2 \sigma_{\alpha_2}^2 \quad (33)$$

$$[\sigma_u^2] = [S_{uU_1} \quad S_{uU_2} \quad (U_1 - U_2)^2 S_{u\alpha_1} \quad (U_1 - U_2)^2 S_{u\alpha_2}] \{ \sigma_{U_1}^2 \quad \sigma_{U_2}^2 \quad \sigma_{\alpha_1}^2 \quad \sigma_{\alpha_2}^2 \}^T$$

Similarly, equations (34) and (35) give the uncertainty in w and v components as a function of the uncertainty in the planar velocity components and the uncertainty in the angles.

$$[\sigma_w^2] = [S_{wU_1} \quad S_{wU_2} \quad (U_1 - U_2)^2 S_{w\alpha_1} \quad (U_1 - U_2)^2 S_{w\alpha_2}] \{ \sigma_{U_1}^2 \quad \sigma_{U_2}^2 \quad \sigma_{\alpha_1}^2 \quad \sigma_{\alpha_2}^2 \}^T \quad (34)$$

$$[\sigma_v^2] = \frac{1}{4} [S_{vV_1} \quad S_{vV_2} \quad w^2 S_{v\beta_1} \quad w^2 S_{v\beta_2} \quad S_{vw}] \{ \sigma_{V_1}^2 \quad \sigma_{V_2}^2 \quad \sigma_{\beta_1}^2 \quad \sigma_{\beta_2}^2 \quad \sigma_w^2 \}^T \quad (35)$$

The sensitivity coefficients in equations (33) to (35) are denoted by S_{ci} 's with subscript c indicating the respective stereo velocity components (u , v , w). The subscript i represents the corresponding elemental planar or angle uncertainty variables ($U_{1,2}$, $V_{1,2}$, $\alpha_{1,2}$ and $\beta_{1,2}$), whose uncertainty is weighted by S_{ci} . The coefficients S_{ci} 's are functions of the stereo angles and the terms are explicitly given in Table 3.1. For the angle uncertainty coefficients $S_{u\alpha_1}$, $S_{u\alpha_2}$, $S_{w\alpha_1}$ and $S_{w\alpha_2}$, the overall sensitivity takes into account a factor of $(U_1 - U_2)^2$. Similarly, the w^2 term contributes to the scaling of the coefficients $S_{v\beta_1}$ and $S_{v\beta_2}$ in equation (35). Comparing the coefficients of $\sigma_{U_1}^2$ and $\sigma_{U_2}^2$ in equation (33) and (34), the presence of $\tan \alpha_1$, $\tan \alpha_2$ terms in the numerator of S_{uU_1} and S_{uU_2} make them unequal for asymmetric stereo angles, unlike S_{wU_1} and S_{wU_2} , which are equal. The σ_v^2 uncertainty is mainly dominated by $\sigma_{V_1}^2$ and $\sigma_{V_2}^2$, but the σ_w^2 uncertainty also affects the σ_v^2 with a sensitivity coefficient S_{vw} , which is proportional to the sum of the tangent of the β angles. The contribution of the angle uncertainties $\sigma_{\alpha_1}^2$ and $\sigma_{\alpha_2}^2$ disappears if the projected velocities U_1 and U_2 are equal to each other.

Table 3.1. Expressions for Sensitivity coefficients as a function of stereo angles for stereo uncertainty propagation equations.

S_{uU_1}	S_{uU_2}	$S_{u\alpha_1}$	$S_{u\alpha_2}$
$\frac{\tan^2 \alpha_2}{(\tan \alpha_1 - \tan \alpha_2)^2}$	$\frac{\tan^2 \alpha_1}{(\tan \alpha_1 - \tan \alpha_2)^2}$	$\frac{\sin^2 \alpha_2 \cos^2 \alpha_2}{\sin^4(\alpha_1 - \alpha_2)}$	$\frac{\sin^2 \alpha_1 \cos^2 \alpha_1}{\sin^4(\alpha_1 - \alpha_2)}$
S_{wU_1}	S_{wU_2}	$S_{w\alpha_1}$	$S_{w\alpha_2}$
$\frac{1}{(\tan \alpha_1 - \tan \alpha_2)^2}$	$\frac{1}{(\tan \alpha_1 - \tan \alpha_2)^2}$	$\frac{\sec^4 \alpha_2}{(\tan \alpha_1 - \tan \alpha_2)^4}$	$\frac{\sec^4 \alpha_1}{(\tan \alpha_1 - \tan \alpha_2)^4}$
S_{vV_1}, S_{vV_2}	$S_{v\beta_1}$	$S_{v\beta_2}$	S_{vw}
1	$\sec^4 \beta_1$	$\sec^4 \beta_2$	$(\tan \beta_1 + \tan \beta_2)^2$

3.3 Sensitivity Analysis

To assess the variation and range of the coefficients weighting the elemental uncertainties in stereo uncertainty propagation (equations (33), (34) and (35)), contour maps of the coefficients S_{ci} 's for a range of the stereo camera angles are shown in Figure 3.3. For a typical camera configuration in the $x - z$ plane (as shown in Figure 3.1), stereo angles α_1 and α_2 are varied between 0° and 60° while angle β is considered close to 0° (between -5° and $+5^\circ$). The sensitivity coefficients are multiplied with the elemental uncertainties (via Monte Carlo approach) to ascertain the variation of σ_u , σ_v and σ_w with the stereo angles. A uniform distribution of 0 to 0.5 pixels is assumed for the planar uncertainty components ($\sigma_{U_1}, \sigma_{V_1}, \sigma_{U_2}, \sigma_{V_2}$) and the angle uncertainties ($\sigma_{\alpha_1}, \sigma_{\beta_1}, \sigma_{\alpha_2}, \sigma_{\beta_2}$) in the range of 0° to 1° are considered. For w component, a typical range depends on the particular nature of the flow. Here we choose a uniform distribution in the range of 0 to 2 pixels for the out-of-plane velocity component. The $U_1 - U_2$ term is obtained for each α_1, α_2 combination using the geometric reconstruction equation(32). It is to be noted that the elemental uncertainties are randomly sampled from a uniform distribution to reflect a range of possible experimental conditions.

Figure 3.3a shows the coefficients for the u component. The coefficients S_{uU_1} and S_{uU_2} increase with the angles α_2 and α_1 respectively, up to a maximum value of 1. For non-symmetric stereo angles, that is α_1 equal to -55° and α_2 equal to 5° , $\sigma_{U_2}^2$ uncertainty has a more significant

contribution than $\sigma_{U_1}^2$ as the coefficient S_{uU_1} tends to 0. The angle uncertainty coefficients $S_{u\alpha_1}$ and $S_{u\alpha_2}$ have values greater than 1 for smaller angles in the range $\alpha_1 \geq -10^\circ, \alpha_2 \leq 30^\circ$ and $\alpha_1 \geq -30^\circ, \alpha_2 \leq 10^\circ$ respectively. However, since for typical values of angle and planar velocity errors the squared uncertainties are as much as three orders of magnitude higher for the velocities, unless the difference between U_1 and U_2 are large the uncertainty in the camera angles will contribute little to the total. Combining the coefficient maps with the planar and angle uncertainty distributions, the propagated uncertainty map for σ_u shows a minimum (about 0.23 pixels) along the diagonal, between 15° and 55° , which indicates that symmetric angles yield minimum uncertainty. Overall, though, the reconstruction process has only a small effect on the u velocity, with uncertainties remaining less than 0.3 pixels as long as both angles are above 8° .

For the out of plane velocity uncertainty, in Figure 3.3b shows that the planar uncertainty weights S_{wU_1} and S_{wU_2} are equal and scale $\sigma_{U_1}^2$ and $\sigma_{U_2}^2$ by a factor greater than 1 for α_1 and α_2 less than 25° . Coefficients $S_{w\alpha_1}$ and $S_{w\alpha_2}$ become less than 1 and go to minimum for $\alpha_2 \geq 45^\circ$ and $\alpha_1 \geq 45^\circ$ respectively, indicating a lower sensitivity to the angle uncertainty in that range. Similarly to σ_u , in most cases the uncertainty due to the angles remains low because of the small magnitude of σ_{α_1} and σ_{α_2} , leaving the geometry and the planar uncertainty as the major contributors. In contrast to the u and (as will be seen) v components, the larger sensitivity coefficients on the planar velocity uncertainties tend to dramatically amplify the final w velocity uncertainties. This can be seen from the σ_w contour which varies from a minimum of 0.15 pixels for $\alpha_1 + \alpha_2 = 120^\circ$ to 0.5 pixels at angle of 24° , about 1 pixel at an angle of 14° and approaches infinity at 0° .

Finally, the sensitivity coefficients for the v component are shown in Figure 3.3c. The planar uncertainty weights (S_{vV_1}, S_{vV_2}) for V_1 and V_2 are constant at 1.0 and are thus not plotted. The coefficients $S_{v\beta_1}$ and $S_{v\beta_2}$ also have values close to 1 in the range of β considered. This leads to a sensitivity of $0.25w^2$ for the angle uncertainties $\sigma_{\beta_1}^2$ and $\sigma_{\beta_2}^2$, making the out-of-plane velocity the major driver of the sensitivity of σ_v to the angle uncertainties. The contribution of σ_w^2 uncertainty is weighted by S_{vw} , which varies in the range 0 to 0.04 and is zero for $\beta_1 = -\beta_2$ and increases if both the cameras have any undiagnosed tilt in the same direction (in $y - z$ plane of Figure 3.1). Thus, the uncertainty on w has a negligible impact on v , and for reasonable values of the angle uncertainty (such as the $< 1^\circ$ values considered here), so does the out-of-plane velocity,

leaving only the contribution from the planar estimates of V . The combined effect of these coefficients leads to practically a constant value of 0.2 pixels for σ_v with a slightly higher value of 0.22 pixels at $\beta_1 = \beta_2 = \pm 5^\circ$. It is to be noted that σ_w is a function of the angles α_1 and α_2 (Figure 3.3b) and thus RMS of σ_w (about 0.5 pixels excluding the high values near 0° to 5° angle) is used in equation (35) to obtain the σ_v contour (Figure 3.3c). In summary, it is clear from Figure 3.3 that symmetric stereo angles in the range 45° to 60° will minimize the uncertainty in u and w components. However, for scenarios with asymmetric angles and unequal range of planar uncertainties one can assess and minimize the individual uncertainty contributions based on their relative weights predicted by these contour maps.

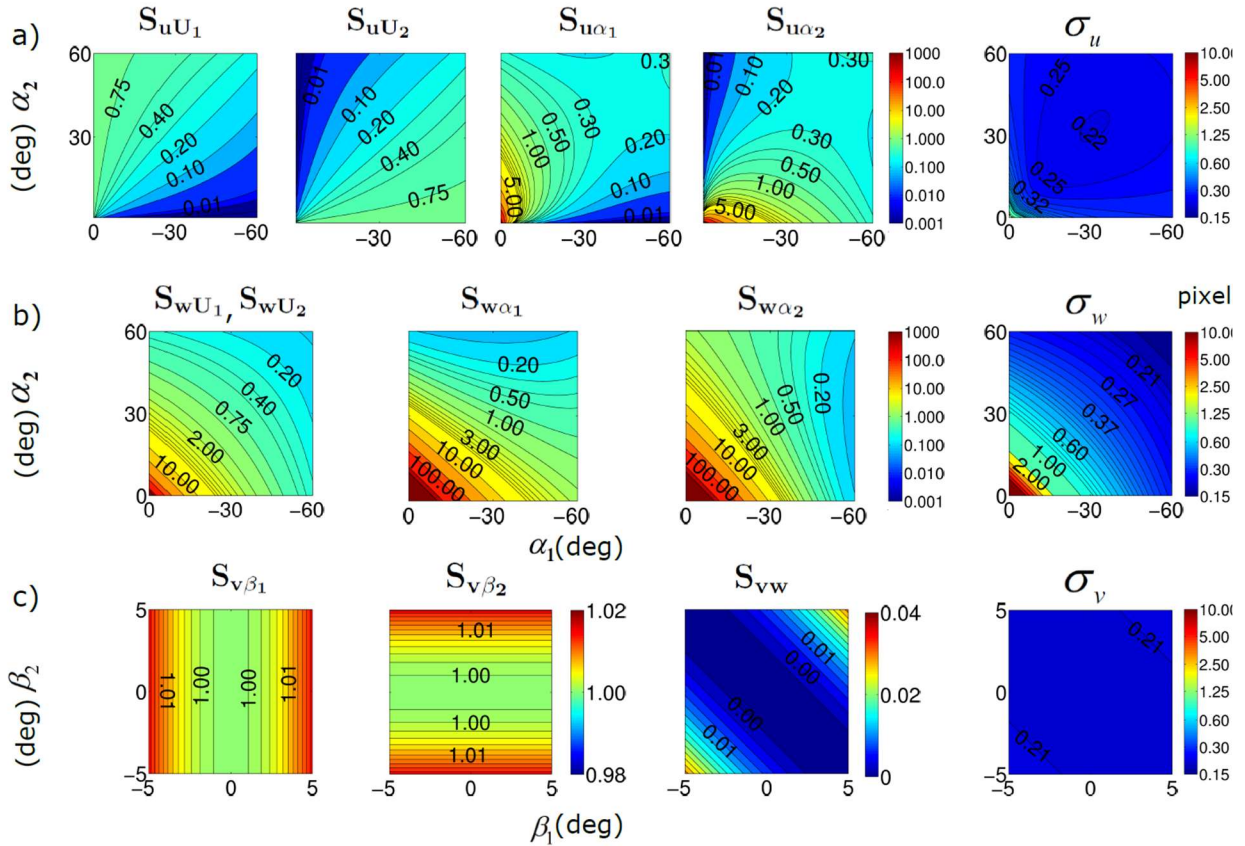


Figure 3.3. Contour maps of sensitivity coefficients and reconstructed velocity uncertainties as a function of stereo angles are shown for a) u , b) w and c) v components.

The sensitivity coefficients for the mapping function gradient uncertainty can also be analyzed. Equation (31) can be written in a more explicit form as follows:

$$\begin{aligned}
\begin{bmatrix} \sigma_{FX_x}^2 \\ \sigma_{FX_y}^2 \\ \sigma_{FX_z}^2 \end{bmatrix} &= \begin{bmatrix} (2a_5 + 6a_{11}x + 2a_{12}y + 2a_{15}z)^2 & (a_6 + 2a_{12}x + 2a_{13}y + a_{16}z)^2 & (a_8 + 2a_{15}x + a_{16}y + 2a_{18}z)^2 \\ (a_6 + 2a_{12}x + 2a_{13}y + a_{16}z)^2 & (2a_7 + 2a_{13}x + 6a_{14}y + 2a_{17}z)^2 & (a_9 + a_{16}x + 2a_{17}y + 2a_{19}z)^2 \\ (a_8 + 2a_{15}x + a_{16}y + 2a_{18}z)^2 & (a_9 + a_{16}x + 2a_{17}y + 2a_{19}z)^2 & (2a_{10} + 2a_{18}x + 2a_{19}y)^2 \end{bmatrix} \begin{bmatrix} \sigma_x^2 \\ \sigma_y^2 \\ \sigma_z^2 \end{bmatrix} \\
&+ \begin{bmatrix} \sigma_{a_2}^2 + (2x)^2\sigma_{a_5}^2 + y^2\sigma_{a_6}^2 + z^2\sigma_{a_8}^2 + (3x^2)^2\sigma_{a_{11}}^2 + (2xy)^2\sigma_{a_{12}}^2 + y^4\sigma_{a_{13}}^2 + (2xz)^2\sigma_{a_{15}}^2 + (yz)^2\sigma_{a_{16}}^2 + z^4\sigma_{a_{18}}^2 \\ \sigma_{a_3}^2 + x^2\sigma_{a_6}^2 + (2y)^2\sigma_{a_7}^2 + z^2\sigma_{a_9}^2 + x^4\sigma_{a_{12}}^2 + (2xy)^2\sigma_{a_{13}}^2 + (3y^2)^2\sigma_{a_{14}}^2 + (xz)^2\sigma_{a_{16}}^2 + (2yz)^2\sigma_{a_{17}}^2 + z^4\sigma_{a_{19}}^2 \\ \sigma_{a_4}^2 + x^2\sigma_{a_8}^2 + y^2\sigma_{a_9}^2 + (2z)^2\sigma_{a_{10}}^2 + x^4\sigma_{a_{15}}^2 + (xy)^2\sigma_{a_{16}}^2 + y^4\sigma_{a_{17}}^2 + (2xz)^2\sigma_{a_{18}}^2 + (2yz)^2\sigma_{a_{19}}^2 \end{bmatrix} \quad (36)
\end{aligned}$$

The first part on the R.H.S. of equation (36) is the contribution of the world coordinate uncertainties and the second part denotes the contribution of the uncertainties in the mapping function coefficients. It is important to note here that coefficient a_1 denotes the offset between world coordinate and pixel coordinate origin location and coefficients a_2 , a_3 and a_4 are related to the x , y and z magnifications respectively. The coefficients a_5 to a_{19} are typically very small and thus the sensitivity of the gradient uncertainty to the world coordinate position uncertainty is low. However, for calibration images with distortion, the higher order coefficients can become significant, consequently increasing the contribution of the world coordinate uncertainty. For the second part comprising of the $\sigma_{a_i}^2$ terms, the $\sigma_{a_2}^2$, $\sigma_{a_3}^2$ and $\sigma_{a_4}^2$ have the dominant contribution to the angle uncertainty. Thus, the uncertainty in the magnification will often be the dominant driver for the uncertainty in the gradients, and consequently, by propagation through equation (30) for the camera angles as well.

3.4 Results

The stereo-PIV uncertainty framework was verified using a synthetic uniform flow case and an experimental vortex ring case. The synthetic case was tested for results with and without self-calibration, using only the IM [7] method for planar uncertainty estimation. The vortex ring case was tested with self-calibration for different camera orientations using both CS [8] and IM methods for estimating planar PIV uncertainty. The details of the two cases and the resulting uncertainty predictions are discussed in detail in the following sections.

3.4.1 Uncertainty estimation for synthetic flow case

For simulating stereo-PIV images a volume (150mmx150mmx15mm) of 3×10^5 particles was generated and only the particles falling within a Gaussian beam of certain thickness (either 1mm

or 3mm) were rendered in the images. The images were generated using an in-house lightfield ray-tracing code. The code simulates 10000 light rays per particle, Mie-scattering of the light rays from the particles and its propagation through a lens system to form an image in a camera at any orientation. To calculate the pixel intensity a 1-pixel by 1-pixel square region was considered centered about the point at which the traced ray hits the sensor. The fractional area of the square belonging to each pixel in a four-pixel neighborhood was used to calculate a weighing factor. This factor was multiplied with the radiance of the light ray and the angle of incidence to compute the amount by which the intensities of each of the four pixels were incremented. Thus, in effect, intensity of each pixel is an integral of light rays falling across it, with a fill factor of 1.0. The world coordinate system was defined and cameras were placed at an angle of 30° in the $x - z$ plane. A 105 mm lens with f-number equal to 8 was used. A uniform flow with in-plane velocities u and v equal to -2.5 and 3.72 pixels/frame respectively and out of plane motion w varying from 5% to 30% of laser sheet thickness was used to generate successive particle images. A second set of images used u and v of -6.55 and 6.23 pixels/frame respectively. The uniform flow with varying out-of-plane motion and laser sheet thickness was considered to see its effect on the random uncertainty in the disparity field. Flow gradients are not considered herein as the intent was to concentrate on the effect of the calibration and reconstruction, not the effect of challenging flow conditions on the uncertainty of the displacement estimates. The out-of-plane motion w was changed for a particular light sheet thickness to assess the effect of loss-of-pairs in stereo uncertainty propagation. Also, for the same w , a thicker light sheet would include more particle images across the depth and introduce more uncertainties in evaluating the disparity field as well as the planar cross-correlation. The choices of the camera and calibration parameters were guided by the vortex ring experimental case, which will be discussed in the later section.

The synthetic images were processed with “PRANA” stereo code [25], [26], [27]. A polynomial mapping function was obtained using calibration images at multiple z locations of a single plane target. The calibration $z = 0$ location was purposely offset by 3mm to check the uncertainty propagation results with and without self-calibration. The calibration uncertainty was estimated from the disparity map following the algorithm in Figure 3.2. The planar velocities were obtained using multi-pass processing with image deformation and the corresponding uncertainties were obtained using IM. Finally, the planar and the angle uncertainties were propagated using equations (33), (34), and (35).

Figure 3.4 shows the error and standard uncertainty histogram for u , v and w components in the uniform flow case with self-calibration. The results are shown for the 1mm thick light sheet case and the uncertainty distributions include the contribution of the angle uncertainties. The error distribution is nearly symmetric about zero for all three components, indicating minimal bias error in the measurement. The u and v component errors are contained within ± 0.2 pixels, while the w component error extends to ± 0.5 pixels. The uncertainty distributions shown here are only the positive bounds; the predicted negative bounds are assumed to be identical and symmetric about zero and are not shown here for clarity. The σ_u , σ_v and σ_w distributions have a sharp rise and a gradual fall with a small increase near the tail of the distributions. The vertical dashed and dotted lines indicate the RMS values of the uncertainty and error distributions, respectively. Sciacchitano et al. [9] showed that for error distributions with zero bias, the RMS of the error and uncertainty distributions should match each other when correctly predicted. Figure 3.4 depicts nearly perfect agreement in the RMS values implying excellent uncertainty prediction. Another important metric for comparison is the coverage, which is defined as the percentage of measurement errors falling within the estimated uncertainty band [28]. The standard uncertainty coverage is ideally expected to be 68.5%.

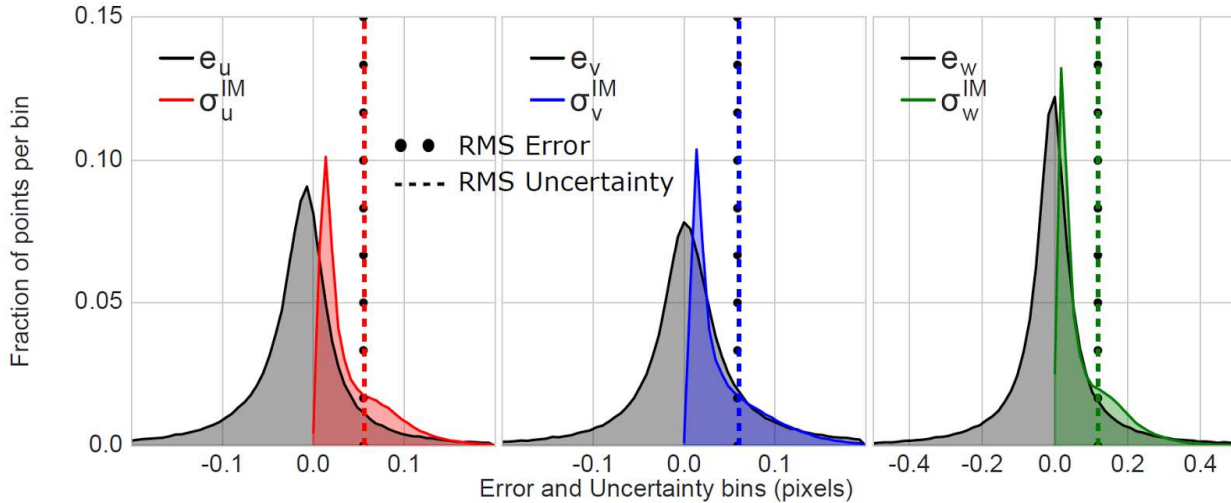


Figure 3.4. Error and uncertainty histograms for u , v and w components in synthetic uniform flow case with self-calibration.

Table 3.2 shows the coverage values for this case. The coverage values were calculated based on 193548 samples. Coverage values of about 59% and 62% are obtained for this case with 1 mm and 3mm light sheet thickness respectively, which is only slightly lower than expected. The

RMS uncertainty and the coverage values thus indicate successful prediction of stereo measurement uncertainty. The uncertainty propagation model was also tested for stereo reconstruction without self-calibration. Due to the initial disparity it is expected that the calibration error should lead to an additional bias error in the measured velocity field as noticed in the increase of RMS error values for this case, shown in Table 3.2, as the measured total error includes the effects of both systematic and random errors. The RMS values of error and uncertainty distributions reasonably match each other, within 0.01 pixels, for both light sheet thicknesses. However, the coverage is less than the expected value, in particular for the v component it is about 42%. This may be attributed to bias in the error distribution in which case even if the RMS error and uncertainty values match, a symmetric uncertainty bound about zero does not account for the bias and leads to under prediction of coverage.

Table 3.2. RMS of the total error, uncertainty and standard coverage for uniform flow case, with and without self-calibration.

With Self-Calibration						
Light Sheet Thickness	Velocity Component	With angle uncertainty			Without angle uncertainty	
		RMS Error	RMS Uncertainty	Coverage	RMS Uncertainty	Coverage
1 mm	u	0.055	0.056	59.0	0.056	59.0
	v	0.059	0.061	57.8	0.061	57.8
	w	0.118	0.119	59.6	0.119	59.6
3 mm	u	0.056	0.056	62.1	0.056	62.1
	v	0.059	0.061	62.1	0.061	61.9
	w	0.119	0.114	63.3	0.114	63.3
No Self-Calibration						
1 mm	u	0.063	0.061	50.6	0.060	47.6
	v	0.070	0.064	42.3	0.064	41.3
	w	0.123	0.127	63.4	0.126	59.8
3 mm	u	0.061	0.067	68.9	0.058	53.9
	v	0.075	0.068	42.9	0.064	37.5
	w	0.125	0.132	75.1	0.118	60.7

To assess the contribution of the angle uncertainty, the stereo uncertainty propagation was also tested with and without the angle uncertainty terms. For zero disparity after converged self-calibration, addition of angle uncertainty terms had a negligible contribution to the total uncertainty as evident from the RMS uncertainty and coverage values in Table 3.2 (top- half). Without self-calibration, the RMS uncertainty and the coverage slightly improved upon adding the

angle uncertainties for the 1 mm laser sheet case. However, for the 3mm light sheet case, the predicted uncertainty distributions show a significant increase in the RMS values when the uncertainties in the angles are accounted for. Since the w velocity component was set as a percentage of the light sheet thickness in the simulated flow, the 3 mm thick sheet had higher out of plane motion. Consequently, the projected velocity component difference ($U_1 - U_2$) was increased, which in turn increased the sensitivity of the angle uncertainties in this case (following equations (33) to (35)). Including the angle uncertainty also changed the coverage from 54%, 38% and 61% to 69%, 43% and 75%, for u , v and w components respectively.

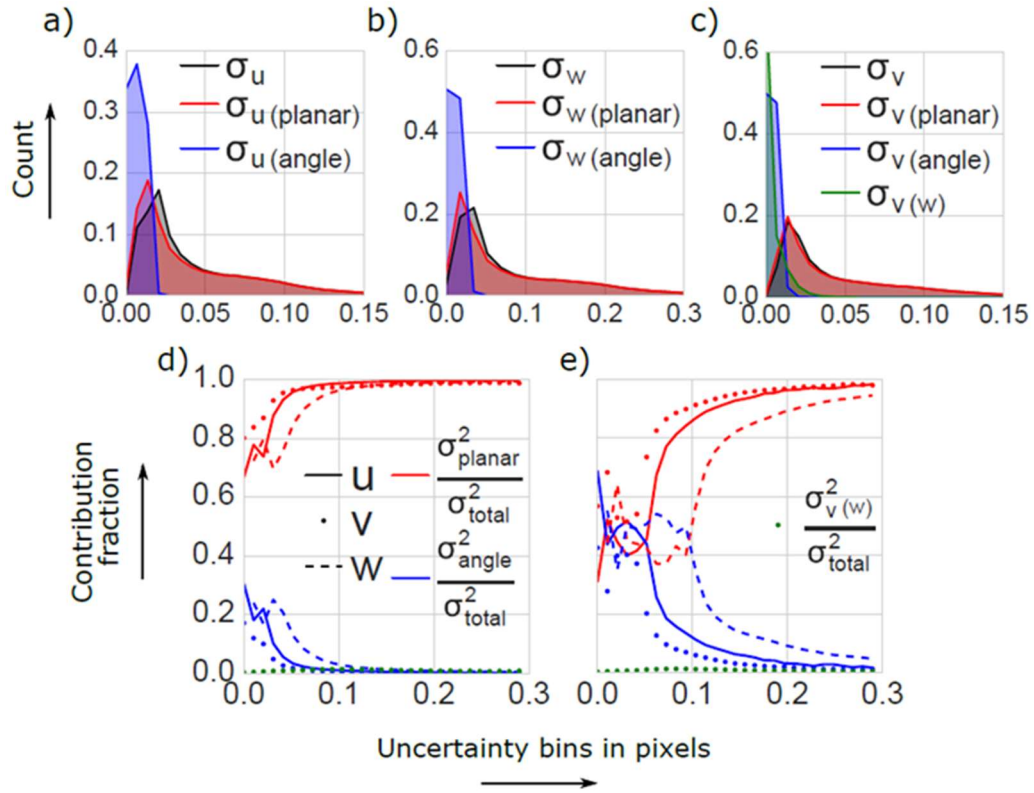


Figure 3.5. Contribution of planar and angle uncertainty to overall stereo field uncertainty for uniform flow case in presence of disparity. Subplots a), b) and c) show the uncertainty histograms for u , w and v components for 1mm laser sheet case. Subplots d) and e) show contribution fraction of different uncertainty components for 1mm and 3mm thick laser sheet cases respectively.

Figure 3.5 shows the relative contribution of the planar and angle uncertainty in each velocity component for the uniform flow case (1 mm thick light sheet) without self-calibration. The black histograms represent the overall uncertainty in the stereo components (Figure 3.5a, b,

c). The sum of the planar uncertainty terms ($[S_{uU_1}\sigma_{U_1}^2 + S_{uU_2}\sigma_{U_2}^2]^{0.5}$) is shown as $\sigma_u(planar)$ and the total angle uncertainty ($[(U_1 - U_2)^2(S_{u\alpha_1}\sigma_{\alpha_1}^2 + S_{u\alpha_2}\sigma_{\alpha_2}^2)]^{0.5}$) is plotted as $\sigma_u(angle)$. Similar terms are plotted for w and v components (Figure 3.5b, c). The latter includes an additional histogram showing the contribution of σ_w^2 (equation (35)), denoted by $\sigma_{v(w)}$. For the u component the planar and angle uncertainty distribution peaks are at 0.02 and 0.013 pixels respectively. The corresponding peaks for the w component are at 0.03 and 0.02 pixels, whereas v component has both peaks at 0.014 pixels. The location of the peaks at small values of uncertainty indicates that in most cases the uncertainty is low from either source. However, the uncertainties distributions due to the planar velocity estimates have much longer tails, meaning that in many cases the contribution from the velocity estimates will dominate the angle contributions, which remain below about 0.02 for u and v , and below 0.04 for w . This can be seen more clearly by the exact contribution fraction of planar and angle uncertainties in each uncertainty bin, which is shown for the 1mm and 3mm thick light sheets in Figure 3.5d and Figure 3.5e respectively. Each component is denoted by a different line style and the planar and angle uncertainty fractions are denoted by red and blue colors. The angle uncertainty contribution is about 20% up to total uncertainties of 0.05 pixels for the 1mm thick sheet. For the 3mm sheet it is about 50% for an uncertainty range up to 0.1 pixels. In the higher uncertainty bins the percentage contribution of planar uncertainty significantly increases and dominates the overall uncertainty distribution. The $\sigma_{v(w)}^2/\sigma_{total}^2$ term shown by the green dots remain almost zero throughout the uncertainty range indicating negligible contribution of σ_w to the v component uncertainty. The angle uncertainty has higher contribution for u and w components compared to the v velocity due to higher values of σ_α compared to σ_β , which is consistent with the camera configuration and existing disparity map. In summary, the results make it clear that in most cases the planar velocity uncertainty and the choice of geometric configuration for the experiment are the dominant sources of uncertainty in the final reconstructed velocities.

3.4.2 Uncertainty estimation for the experimental vortex ring flow case

The stereo-PIV experimental vortex ring case from fourth PIV Challenge 2014, was also used for validating the stereo uncertainty propagation model. A vortex ring in water was formed using motor-controlled piston motion in a cylinder and viewed using five cameras in a cross orientation.

Figure 3.6 shows a schematic of the experimental set-up. Camera 1 is at the center, cameras 4 and 2 are on the left and right side and cameras 3 and 5 are on top and bottom, respectively. A 2mm thick laser sheet was used and images were recorded at 1000 frames per second. The Reynolds number in this case was approximately 2300. Further details of the experimental set-up and results are presented in Kähler et al.[29]. To establish the ground truth, a five camera tomographic reconstruction [30] was performed using 10 iterations with MART algorithm. Prior to volumetric reconstruction the images were pre-processed with intensity normalization and background subtraction to enhance reconstruction quality. Volumetric self-calibration was also done to correct for any misalignment. The reconstructed intensity field was used to perform three dimensional cross correlation and u , v and w components were obtained in the volumetric grid. For calculating the velocity field pyramid correlation [31] was used. This technique computes the correlation between frames at different intervals and uses a homothetic transformation to combine them to yield an ensemble-averaged correlation plane with better precision and higher signal to noise ratio. Thus near the vortex core, a larger time separation between frames yields higher displacement, which leads to a better resolution. An optimal frame number of 4 was calculated taking into account the different sources for loss-of-correlation.

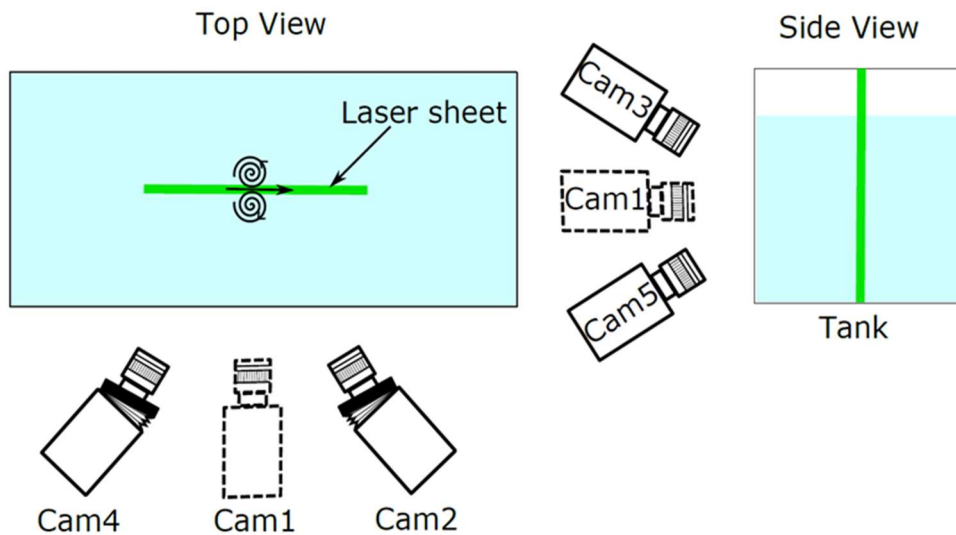


Figure 3.6. Schematic of experimental vortex ring set-up. Cam1 is in center and hence shown in dotted line. Cam2 and Cam4 are in horizontal plane with Scheimpflug adapter. Cam3 and Cam5 are in vertical plane without Scheimpflug adapter.

The tomo-PIV measurement at $z = 0$ location is used as the ground truth. It is to be noted that the uncertainty in the tomographic solution should be less than the stereo solution for the tomo-PIV to act as a reference solution. An independent reference solution does not exist to ascertain the uncertainty in each system. However, a measure of divergence of the velocity field can be used to compare the two measurements, as for an ideal solution it should be zero following continuity. Here, we neglect the out-of-plane gradient as stereo solution is two-dimensional. The mean divergence of the in-plane velocity field over the entire time series is 0.002 s^{-1} for both, but the RMS of the divergence of the instantaneous fields is 0.08 s^{-1} for the tomo-PIV solution whereas, it is 0.2 s^{-1} for the stereo-PIV measurement. The smaller RMS of divergence of the velocity field for tomo-PIV indicates that the estimated velocities closely approach the divergence free true solution. Thus if the true solution were known, this would yield smaller RMS error for the tomo-PIV solution and the corresponding uncertainty bounds would be much lesser than the stereo uncertainty limits. This supports the notion that the volumetric results can serve as a ground truth for comparison.

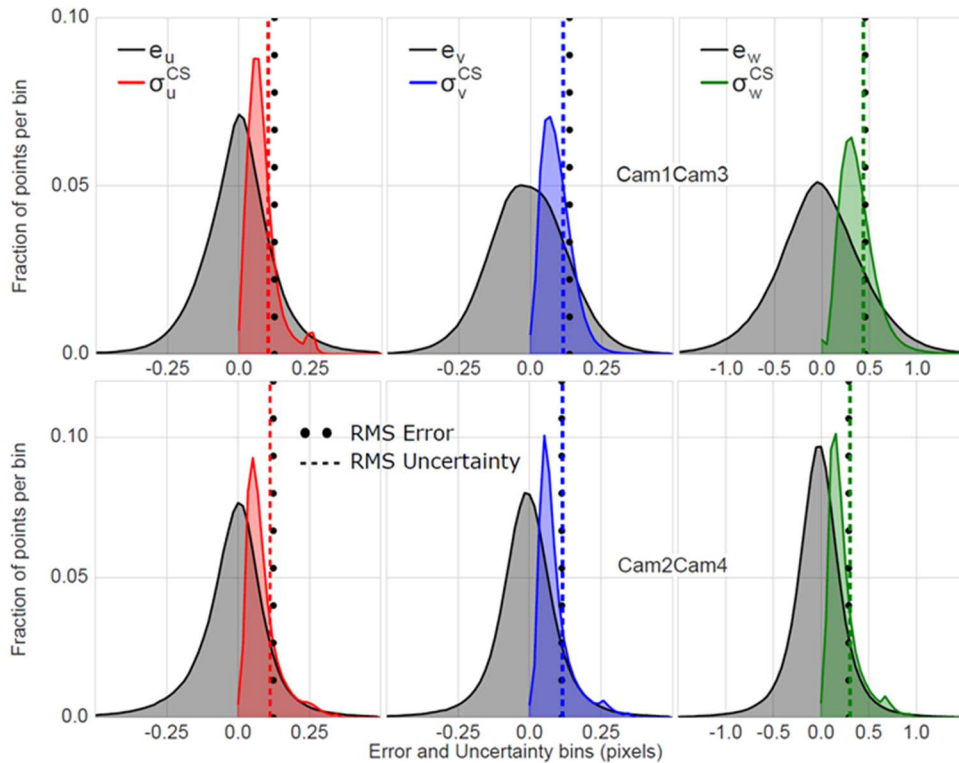


Figure 3.7. Vortex ring stereo velocity field error and uncertainty histogram for different camera orientation (Cam1Cam3: Top and Cam2Cam4: Bottom) using CS method for planar uncertainty estimation.

For the stereo processing of the vortex ring images, a polynomial mapping function was used for calibration. Self-calibration was performed using PRANA. The corrected mapping was used to dewarp the images onto the region of interest and the dewarped images were cross correlated with multi-pass iterative window deformation scheme. The planar uncertainty was estimated using the IM algorithm for PRANA processed velocity fields. The same dewarped images were also processed with similar settings using DaVis 8.2.1 to get the CS uncertainty estimates. Both the PRANA and DaVis planar velocity fields were reconstructed using the same geometric reconstruction code. The planar uncertainties and the angle uncertainties were propagated using equations (33), (34) and (35) and the uncertainty distributions for σ_u , σ_v and σ_w were obtained.

The stereo uncertainty was evaluated for two pairs of cameras, namely, camera 1 and camera 3 (vertical pair denoted by Cam1Cam3) and camera 2 and camera 4 (horizontal pair denoted by Cam2Cam4). Camera 1 is oriented front on (angle in $x - z$ plane $\alpha = 0$, angle in $y - z$ plane $\beta = 0$) while camera 3 is at an angle β equal to 25^0 and without Scheimpflug adapter. In contrast Camera 2 and 4 are at an angle $\alpha = \pm 30^0$, and both with Scheimpflug adapters. Thus, each pair has different imaging parameters and magnifications and so both pairs are compared against the tomographic solution.

Figure 3.7 shows the error and estimated uncertainty distributions for Cam1Cam3 (top) and Cam2Cam4 (bottom) configurations using CS method for planar uncertainties. The error distributions appear to be Gaussian and symmetric about zero. The e_u and e_v distributions vary in the range of ± 0.3 pixels while e_w varies up to about ± 1 pixel. The v component error has a slightly wider spread compared to e_u for Cam1Cam3 case, but slightly smaller for Cam2Cam4.

Table 3.3. RMS error, uncertainty and standard coverage for vortex ring case with IM and CS methods for planar uncertainty estimation.

Camera Configuration	Velocity Component	Image Matching (IM)			Correlation Statistics (CS)		
		RMS Error	RMS Uncertainty	Coverage	RMS Error	RMS Uncertainty	Coverage
Cam1 Cam3	u	0.124	0.098	56.0	0.125	0.102	52.9
	v	0.138	0.089	42.8	0.137	0.114	50.0
	w	0.455	0.462	65.7	0.454	0.438	60.0
Cam2 Cam4	u	0.122	0.125	71.9	0.123	0.112	58.0
	v	0.112	0.147	81.5	0.113	0.114	62.8
	w	0.286	0.342	78.9	0.291	0.307	65.5

For both cases, e_w is larger than e_u or e_v , but as expected the increase is larger for the Cam1Cam3 data due to the less optimized experimental setup. The uncertainty distributions are shown on one-sided as discussed in Figure 3.4 and are thus scaled down by a factor of 2 to match the heights of the error distributions. In this case the uncertainties are sharply distributed with the modal values

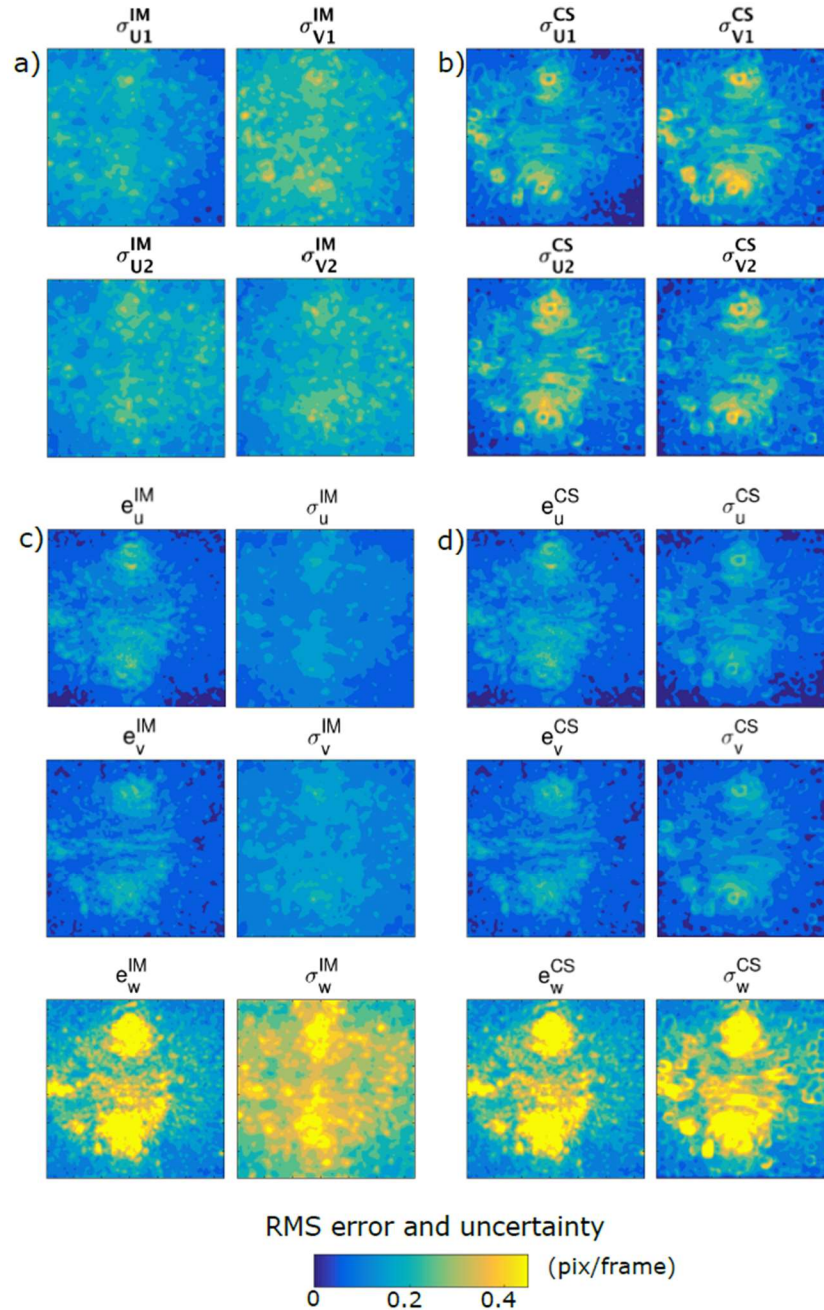


Figure 3.8. Planar uncertainty RMS contours for each camera components are shown in a) for IM and b) for CS methods. The RMS error and uncertainty spatial contours for stereo components are shown in c) and d) for IM and CS methods respectively.

and RMS values close to each other. The dotted and dashed lines indicating the RMS values of the error and uncertainty distributions respectively, are in good agreement for both camera orientations, especially for Cam2Cam4. Also, the coverage for Cam1Cam3 is about 50% to 60% while Cam2Cam4 has a higher coverage of about 58% to 66%.

A quantitative comparison of the estimated stereo uncertainties using two different planar uncertainty methods (IM and CS) is presented in Table 3.3. Both methods predicted RMS uncertainty values within 10% of the RMS error for u and w component velocities. However, the v component uncertainty using IM is under predicted by 0.05 pixels for Cam1Cam3 and over predicted by 0.035 pixels for Cam2Cam4 case. This is also reflected in the IM method standard coverage which is 81.5% for Cam2Cam4 and about 43% for Cam1Cam3. The difference in IM and CS results emphasize the contribution of the planar uncertainty estimates in stereo uncertainty propagation as only the planar uncertainty estimation method was changed, keeping all the other parameters the same.

To probe the difference in results shown in Table 3.3, the spatial contour maps of the RMS error and uncertainty for Cam2Cam4 orientation using IM and CS methods are compared in Figure 3.8. Figure 3.8a and Figure 3.8b show the planar uncertainty estimates for the IM and CS methods respectively. The CS planar uncertainty field shows sharper variation from about 0.35 pixels near the core to 0.05 pixels near the domain edges, while IM uncertainty prediction gives a smoother field which varies from 0.3 pixels in the core to about 0.13 pixels near the margins. This effect is directly propagated in the stereo solution uncertainty spatial maps shown in Figure 3.8c and d. The error distributions look essentially identical for both processing schemes, indicating that differences in the underlying velocity fields did not contribute to the final variation in the uncertainties. However, the IM method predicts a higher uncertainty over a wide range of the spatial domain compared to CS estimate, which only predicts higher uncertainty in the vortex core region. Thus the Figure 3.8d uncertainty contours are more consistent with the RMS error map compared to Figure 3.8c, which explains the over prediction of IM method coverage, mentioned in Table 3.3. In addition, it appears that using the IM estimates the uncertainties in the vortex core are under predicted.

Figure 3.9 shows the RMS error (solid line) vs RMS uncertainty (dotted line) time series for 50 frames. Although the temporal variation in RMS error and uncertainty over the 50 frames are negligible, the figure shows the quantitative agreement between the expected and predicted

uncertainty values for both IM and CS methods and also compares the RMS errors across different camera configurations. The RMS of σ_w is around 0.45 pixels/frame for Cam1Cam3 case compared to 0.3 pixels/frame for Cam2Cam4 case and the resulting error ratio of out-of-plane to in-plane RMS errors is consistent with the stereo inclusive angles for each configuration. The lack of Scheimpflug adapter on camera 3 also contributes to the increased error in Cam1Cam3 solution. The RMS uncertainty line closely matches the RMS error line for CS case and the agreement is better for Cam2Cam4 configuration indicating that the estimation of stereo uncertainties is better for an optimized experiment. The under prediction and over prediction of IM predicted stereo uncertainties in the time series is consistent with previous observations.

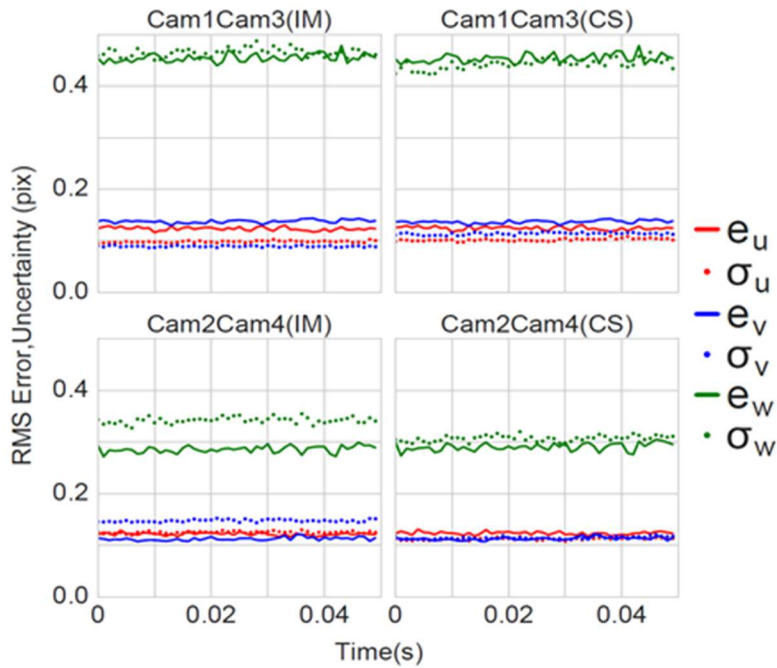


Figure 3.9. Comparison of RMS error and uncertainty temporal distributions for the vortex ring case. The left column plots are for IM method and right column plots are for CS method. Top row and bottom row subplots correspond to Cam1Cam3 and Cam2Cam4 camera orientations respectively.

The results for both the synthetic uniform flow and the vortex ring case show successful stereo uncertainty prediction using the present methodology. The sensitivity coefficients for the stereo uncertainty propagation equations have been plotted as function of a range of stereo angles. For the synthetic case, the out-of-plane motion and light sheet thickness are varied to see their effect on the calibration and planar uncertainties. Also, the experimental case was tested for two

different magnifications and different stereo angles, with one camera pair having Scheimpflug adapter mounted. Thus the results are representative of the effect of variation in some of the significant parameters, which one optimizes in a practical application. However, a more detailed parametric study of the estimated stereo uncertainty with a range of planar and stereo-PIV error sources, needs to be further explored in future.

3.5 Conclusion

The present work establishes a framework for stereo-PIV uncertainty estimation. The individual camera image correlation uncertainty is quantified using existing 2D PIV uncertainty algorithms. The uncertainties in the stereo angles are also quantified. Positional disparity in the particle locations from ensemble correlation of dewarped camera images is considered as the origin of calibration uncertainty. This uncertainty in the disparity field is assigned as the world coordinate uncertainty, and using triangulation uncertainty and least squares fit uncertainty, the uncertainty in the calibration mapping function coefficient is determined. These elemental uncertainties are propagated through the mapping function gradient equation to find the angle uncertainty. Subsequently, the angle and the planar field uncertainties are combined to get the uncertainty in the three velocity components.

The sensitivity analysis of the coefficients show a minimum uncertainty in the velocity components for symmetric stereo angles between 45° and 60° , and that in most cases the uncertainty in the planar velocity estimates controlled the uncertainty due to the calibration. The model has been tested with synthetic uniform flow images as well as an experimental vortex ring case. Both cases show reasonable agreement between the RMS of the standard uncertainty and the RMS of the error distribution. The estimated coverage varied between 58% and 63% for the synthetic flow with self-calibration, which is close to the ideal value of 68.5%. For the vortex ring the coverage values varied over a wider range, from 50% to 80%. An analysis of the synthetic case in presence of disparity showed up to 50% contribution from the angle uncertainty in the lower bins of the total uncertainty distribution. However, after self-calibration and in the absence of any bias error the planar uncertainty again was shown to dominate the total stereo uncertainty. In the experimental case, for the same calibration uncertainty and the same dewarped images, IM and CS methods predicted different stereo uncertainties implying a higher sensitivity of the planar velocity

field uncertainty to the overall uncertainty. Overall, both the cases showed that the estimated stereo uncertainty is strongly dependent on the in-plane velocity field uncertainty.

Although the methodology successfully estimates the stereo component uncertainties, a detailed investigation of the calibration uncertainty for more challenging calibration scenarios (such as distortion in the calibration due to variation in the imaging medium density and refractive index) and more complex flows (such as homogeneous turbulence with high gradient of out-of-plane velocity) will be considered as a future work. Furthermore, the proposed methods can be conceptually extended to volumetric PIV calibration uncertainty where uncertainty in the projected particle locations for all cameras in each sub-volume can quantify the tomographic PIV mapping function uncertainty, which can then be propagated to the final displacement estimates in a similar manner as done here.

Acknowledgements

This research was partially supported by the National Science Foundation (PoLS-1205642, CBET-1336038, and IDBR-1152304).

3.6 References

- [1] R. J. Adrian and J. Westerweel, *Particle Image Velocimetry*. 2011.
- [2] M. Raffel, C. E. Willert, S. T. Wereley, and J. Kompenhans, *Particle Image Velocimetry: A Practical Guide*, vol. 2nd. 2007.
- [3] B. H. Timmins, B. W. Wilson, B. L. Smith, and P. P. Vlachos, “A method for automatic estimation of instantaneous local uncertainty in particle image velocimetry measurements,” *Exp. Fluids*, 2012.
- [4] J. J. Charonko and P. P. Vlachos, “Estimation of uncertainty bounds for individual particle image velocimetry measurements from cross-correlation peak ratio,” *Meas. Sci. Technol.*, vol. 24, no. 6, p. 065301, Jun. 2013.
- [5] Z. Xue, J. J. Charonko, and P. P. Vlachos, “Particle image velocimetry correlation signal-to-noise ratio metrics and measurement uncertainty quantification,” *Meas. Sci. Technol.*, vol. 25, no. 11, p. 115301, 2014.
- [6] Z. Xue, J. J. Charonko, and P. P. Vlachos, “Particle image pattern mutual information and uncertainty estimation for particle image velocimetry,” *Meas. Sci. Technol.*, vol. 26, no. 7, p. 074001, 2015.
- [7] A. Sciacchitano, B. Wieneke, and F. Scarano, “PIV uncertainty quantification by image matching,” *Meas. Sci. Technol.*, vol. 24, no. 4, p. 045302, Apr. 2013.
- [8] B. Wieneke, “PIV uncertainty quantification from correlation statistics,” *Meas. Sci. Technol.*, vol. 26, no. 7, p. 074002, 2015.
- [9] A. Sciacchitano, D. R. Neal, B. L. Smith, S. O. Warner, P. P. Vlachos, B. Wieneke, and F. Scarano, “Collaborative framework for PIV uncertainty quantification: comparative assessment of methods,” *Meas. Sci. Technol.*, vol. 26, no. 7, p. 074004, Jul. 2015.
- [10] D. R. Neal, A. Sciacchitano, B. L. Smith, and F. Scarano, “Collaborative framework for PIV uncertainty quantification: the experimental database,” *Meas. Sci. Technol.*, vol. 26, no. 7, p. 74003, 2015.
- [11] A. Boomsma, S. Bhattacharya, D. Troolin, S. Pothos, and P. Vlachos, “A comparative experimental evaluation of uncertainty estimation methods for two-component PIV,” *Meas. Sci. Technol.*, vol. 27, no. 9, p. 094006, Sep. 2016.
- [12] M. P. Arroyo and C. A. Greated, “Stereoscopic particle image velocimetry,” *Meas. Sci. Technol.*, vol. 2, no. 12, pp. 1181–1186, Dec. 1991.

- [13] S. M. Soloff, R. J. Adrian, and Z. C. Liu, “Distortion compensation for generalized stereoscopic particle image velocimetry,” *Meas. Sci. Technol.*, vol. 8, no. 12, pp. 1441–1454, 1997.
- [14] B. Wieneke, “Stereo-PIV using self-calibration on particle images,” *Exp. Fluids*, vol. 39, no. 2, pp. 267–280, 2005.
- [15] S. J. Beresh, J. L. Wagner, and B. L. Smith, “Self-calibration performance in stereoscopic PIV acquired in a transonic wind tunnel,” *Exp. Fluids*, vol. 57, no. 4, p. 48, Apr. 2016.
- [16] C. Willert, “Stereoscopic digital particle image velocimetry for application in wind tunnel flows,” *Meas. Sci. Technol.*, vol. 8, no. 12, pp. 1465–1479, 1997.
- [17] S. M. Soloff, R. J. Adrian, and Z.-C. Liu, “Distortion compensation for generalized stereoscopic particle image velocimetry,” *Meas. Sci. Technol.*, vol. 8, no. 12, pp. 1441–1454, 1999.
- [18] N.J. Lawson and J. Wu, “Three-dimensional particle image velocimetry: error analysis of stereoscopic techniques,” *Meas. Sci. Technol.*, vol. 8, no. 8, pp. 894–900, Aug. 1997.
- [19] A. K. Prasad, “Stereoscopic particle image velocimetry,” *Exp. Fluids*, vol. 29, no. 2, pp. 103–116, 2000.
- [20] R. Tsai, “A versatile camera calibration technique for high-accuracy 3D machine vision metrology using off-the-shelf TV cameras and lenses,” *IEEE J. Robot. Autom.*, vol. 3, no. 4, pp. 323–344, 1987.
- [21] C. W. H. Van Doorne and J. Westerweel, “Measurement of laminar, transitional and turbulent pipe flow using Stereoscopic-PIV,” *Exp. Fluids*, vol. 42, no. 2, pp. 259–279, 2007.
- [22] J. Westerweel, D. Dabiri, and M. Gharib, “The effect of a discrete window offset on the accuracy of cross-correlation analysis of digital PIV recordings,” *Exp. Fluids*, vol. 23, no. 1, pp. 20–28, May 1997.
- [23] R. Giordano and T. Astarita, “Spatial resolution of the Stereo PIV technique,” *Exp. Fluids*, vol. 46, no. 4, pp. 643–658, Nov. 2009.
- [24] T. Astarita, “Analysis of interpolation schemes for image deformation methods in PIV: effect of noise on the accuracy and spatial resolution,” *Exp. Fluids*, vol. 40, no. 6, pp. 977–987, May 2006.
- [25] A. C. Eckstein, J. Charonko, and P. Vlachos, “Phase correlation processing for DPIV measurements,” *Exp. Fluids*, vol. 45, no. 3, pp. 485–500, 2008.

- [26] A. Eckstein and P. P. Vlachos, “Digital particle image velocimetry (DPIV) robust phase correlation,” *Measurement Science and Technology*, vol. 20. p. 055401, 2009.
- [27] “<https://github.com/aether-lab/prana/>.” .
- [28] H. W. Coleman and W. G. Steele, *Experimentation, Validation, and Uncertainty Analysis for Engineers*. Hoboken, NJ, USA: John Wiley & Sons, Inc., 2009.
- [29] C. J. Kähler, T. Astarita, P. P. Vlachos, J. Sakakibara, R. Hain, S. Discetti, R. La Foy, and C. Cierpka, “Main results of the 4th International PIV Challenge,” *Exp. Fluids*, vol. 57, no. 6, p. 97, May 2016.
- [30] G. E. Elsinga, F. Scarano, B. Wieneke, and B. W. van Oudheusden, “Tomographic particle image velocimetry,” *Exp. Fluids*, vol. 41, no. 6, pp. 933–947, 2006.
- [31] A. Sciacchitano, F. Scarano, and B. Wieneke, “Multi-frame pyramid correlation for time-resolved PIV,” *Exp. Fluids*, vol. 53, no. 4, pp. 1087–1105, Oct. 2012.

Appendix A

Stereo uncertainty propagation equations for large stereo angles (α and β) are given in this section. When the stereo cameras have an inclusive angle $\alpha_1 + \alpha_2$ in the $x - z$ plane and also both cameras are at an angle $\beta_{1,2} \gg 0$ in the $y - z$ plane (Figure 3.10), then the stereo geometric reconstruction (equation (32)) can be written as follows:

$$\begin{aligned}
 u &= \frac{U_2 \tan \alpha_1 - U_1 \tan \alpha_2}{\tan \alpha_1 - \tan \alpha_2} \\
 w &= \frac{U_2 - U_1}{\tan \alpha_1 - \tan \alpha_2} \\
 v &= \frac{V_2 \tan \beta_1 - V_1 \tan \beta_2}{\tan \beta_1 - \tan \beta_2}
 \end{aligned} \tag{A1}$$

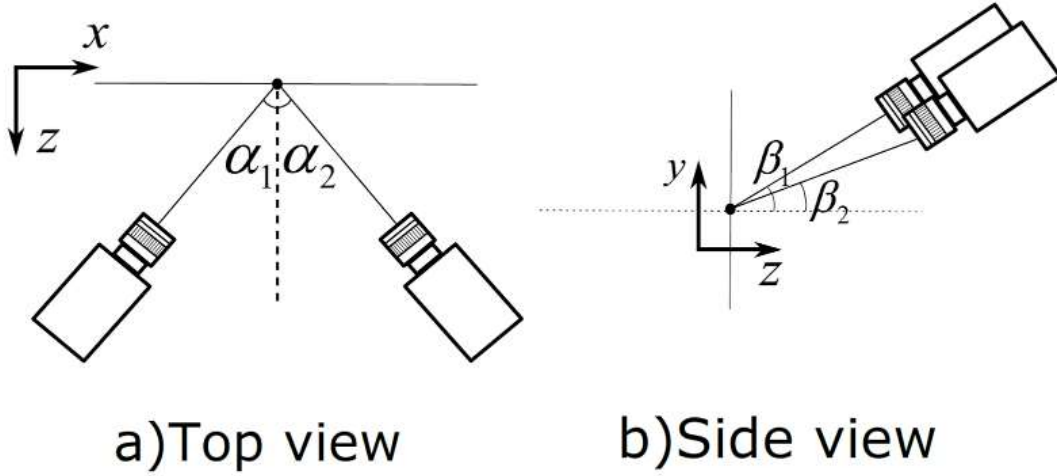


Figure 3.10. Schematic of stereo PIV camera set up for large camera angles.

This equation is true even when the primary stereo angles are β_1 and β_2 as long as the condition $\alpha_{1,2} \gg 0$ also holds. Equation (A1) is different from equation (32) only in the v component. For large β angles the denominator is not small and the v component can be expressed only as a function of planar components V_1, V_2 and the angles β_1, β_2 . The uncertainty propagation for v in this case is similar to that of u component (equation (33)) and is given by equation (A2).

$$\left[\sigma_v^2 \right] = \left[S_{vV_1} \quad S_{vV_2} \quad (V_1 - V_2)^2 S_{v\beta_1} \quad (V_1 - V_2)^2 S_{v\beta_2} \right] \left\{ \sigma_{V_1}^2 \quad \sigma_{V_2}^2 \quad \sigma_{\beta_1}^2 \quad \sigma_{\beta_2}^2 \right\}^T \tag{A2}$$

The sensitivity coefficients for v component uncertainty is given in Table 3.4.

Table 3.4. Sensitivity coefficients for ν component uncertainty propagation for large stereo angles.

$S_{\nu V_1}$	$S_{\nu V_2}$	$S_{\nu \beta_1}$	$S_{\nu \beta_2}$
$\frac{\tan^2 \beta_2}{(\tan \beta_1 - \tan \beta_2)^2}$	$\frac{\tan^2 \beta_1}{(\tan \beta_1 - \tan \beta_2)^2}$	$\frac{\sin^2 \beta_2 \cos^2 \beta_2}{\sin^4(\beta_1 - \beta_2)}$	$\frac{\sin^2 \beta_1 \cos^2 \beta_1}{\sin^4(\beta_1 - \beta_2)}$

4. VOLUMETRIC PARTICLE TRACKING VELOCIMETRY (PTV) UNCERTAINTY QUANTIFICATION

Sayantana Bhattacharya, Pavlos P. Vlachos

Purdue University, Department of Mechanical Engineering, West Lafayette, USA.

This chapter is submitted for review in Experiments in Fluids.

Abstract

We introduce the first comprehensive approach to determine the uncertainty in volumetric Particle Tracking Velocimetry (PTV) measurements. Volumetric PTV is a state-of-the-art non-invasive flow measurement technique, which measures the velocity field by recording successive snapshots of the tracer particle motion using a multi-camera set-up. The measurement chain involves reconstructing the three-dimensional particle positions by a triangulation process using the calibrated camera mapping functions. The non-linear combination of the elemental error sources during the iterative self-calibration correction and particle reconstruction steps increases the complexity of the task. Here, we first estimate the uncertainty in the particle image location, which we model as a combination of the particle position estimation uncertainty and the reprojection error uncertainty. The latter is obtained by a gaussian fit to the histogram of disparity estimates within a sub-volume. Next, we determine the uncertainty in the camera calibration coefficients. As a final step the previous two uncertainties are combined using an uncertainty propagation through the volumetric reconstruction process. The uncertainty in the velocity vector is directly obtained as a function of the reconstructed particle position uncertainty. The framework is tested with synthetic vortex ring images. The results show good agreement between the predicted and the expected RMS uncertainty values. The prediction is consistent for seeding densities tested in the range of 0.01 to 0.1 particles per pixel. Finally, the methodology is also successfully validated for an experimental test case of laminar pipe flow velocity profile measurement where the predicted uncertainty is within 17% of the RMS error value.

Nomenclature

x_w, y_w, z_w : World coordinates or physical coordinates

X^c, Y^c : Camera image coordinates for camera c

FX^c, FY^c : X and Y calibration mapping function for camera c

a_i : camera mapping function coefficients

e : Error

σ : Standard uncertainty

Σ : Covariance matrix

\vec{d} : Disparity vector estimated from ensemble of reprojection error.

u, v, w : Velocity components in x, y, z directions respectively.

Σ_b : Bias uncertainty

4.1 Introduction

Volumetric PTV [1]–[4] is a fluid velocity measurement technique which resolves the three-dimensional (3D) flow structures by tracking the motion of tracer particles introduced in the flow. The tracer particle motion is recorded with multiple cameras to obtain projected particle images. Each camera is also linked to the physical space using a calibration mapping function [5]. The particle images are then mapped back to the physical space using a triangulation process [1], [6]. Finally, a three-dimensional (3D) tracking of the reconstructed particles estimates the Lagrangian trajectories of the particles and subsequently resolves the volumetric velocity field. PTV easily lends itself to calculation of particle acceleration from the tracked trajectories. Also, unlike Tomographic Particle Image Velocimetry (Tomo-PIV) [7], which involves spatial averaging over the interrogation window, 3D PTV has higher spatial resolution as it yields a vector for every tracked particle position. However, as the number of particles increases, identification of overlapping particles and its corresponding 3D reconstruction becomes challenging, which leads to a tradeoff between spatial resolution and reconstruction accuracy. Hence, the simple triangulation-based 3D PTV method introduced in 1993 [1] had limited applications compared to Tomo-PIV for highly seeded flows. Improvements in terms of particle identification [8] and tracking algorithms [9]–[14] have been proposed to minimize the error in the measurement.

Recent advancements in terms of reconstruction algorithms, such as Iterative Particle Reconstruction (IPR) [15] and Shake-the-box (STB) [16] have significantly improved the accuracy of 3D PTV. IPR uses an initial triangulation based reconstructed field to construct a projected image and then minimizes the intensity residuals in the image plane by shaking the particles in world coordinate location. This process achieves a better positional accuracy, reduced fraction of ghost particles and the reconstruction accuracy is comparable to intensity based Multiplicative Algebraic Reconstruction Technique (MART) [7], for up to a seeding density of 0.05 particles per pixels (ppp). This concept has been further advanced in STB, which uses the temporal information, for a time-resolved measurement, to predict the particle location in the future frames and corrects the predicted position iteratively using IPR. Such measurements have successfully resolved flow structures for experiments with high particle concentrations (up to 0.125 ppp). With such capabilities, 3D PTV measurements have gained renewed attention and applicability in various experiments.

To analyze any experimental results with statistical significance, uncertainty quantification (UQ) is crucial, especially, where the measured data are used in a design process or to validate computational models [17]–[21]. Given the increasing applicability and relevance of PTV/IPR/STB volumetric measurements, providing uncertainty estimation for an individual 3D PTV measurement is now of paramount importance.

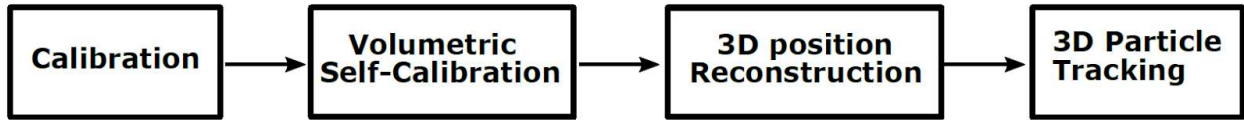


Figure 4.1. A volumetric PTV measurement chain showing the main steps in the process.

Uncertainty estimation in PIV measurements has received interest only recently and several methods have been proposed for planar PIV uncertainty quantification. Broadly such methods can be categorized into direct and indirect methods. Indirect methods rely on a calibration function, which maps an estimated measurement metric (e.g. correlation plane signal to noise ratio metrics [22]–[24] or estimates of the fundamental sources of error [25]) to the desired uncertainty values. Such a calibration is developed from a simulated image database and may not be sensitive to a specific error source for a given experiment. Direct methods, on the other hand, rely directly on the measured displacements and use the image plane “disparity” [26], [27] information or correlation-plane PDF (probability density function) of displacement information [28] to estimate the a-posterior uncertainty values. Comparative assessments [29], [30] have shown that the direct methods are more sensitive to the random error sources. However, indirect methods can be potentially used to predict any bias uncertainty. A direct uncertainty estimation for stereo-PIV measurement [31] has also been proposed recently. A detailed review of such methods can be found in [32]. Thus, although the foundations have been laid for planar and stereo-PIV uncertainty quantification, applicability of such methods to 3D measurements remains untested and these methods train strictly to cross-correlation based measurements. As a result, 3D reconstruction and tracking process for 3D PTV measurements is not covered under these methods and currently a-posterior uncertainty quantification methods for volumetric measurements (PTV/PIV) do not exist and new uncertainty model development is needed.

A flowchart for the different steps in a 3D PTV measurement chain is shown in Figure 1. The first step establishes a mapping function between the camera image coordinates (X, Y) and the

world coordinates (x_w, y_w, z_w) in the physical space using a multi-camera calibration process. The calibration coefficients are then iteratively corrected using the mapping function and the recorded particle images to eliminate any misalignment between the assumed world coordinate system origin of the calibration plane and the actual origin location for the measurement volume. This process is called volumetric self-calibration [6] and is essential in minimizing the reconstruction error (due to existing offset or disparity between cameras) and improving the calibration accuracy. Using the modified calibration, for each particle in a given camera, the corresponding match in the second camera is searched along the epipolar line and the particle matches in all cameras are triangulated [1], [6] to a 3D world position. This reconstruction process can be done in an iterative sense for an IPR type algorithm. However, for the particle pairing process in each camera view, the matching ambiguity increases for higher particle concentrations, which leads to erroneous reconstructions and is considered one of the main sources of error in the process. Finally, the reconstructed 3D particle positions are tracked to find the velocity vectors using “nearest neighbor” or other advanced algorithms [14]. The tracking and reconstruction can be done in conjunction for STB type evaluations. From calibration fitting error, particle position estimation error, the disparity vector estimation error to the error in finding the 3D positions and its pairing, the errors in each step of the process are inter-linked in a complex non-linear way and affect the overall error propagation. The iterative corrections and the governing non-linear functions lead to several interdependent error sources making the definition of a data reduction equation intractable and the development of an uncertainty quantification model non-trivial.

In the current framework, a model is developed to quantify the uncertainty in particle image position and the mapping function coefficient. These uncertainties are in turn combined with the uncertainty propagation through the reconstruction process. Finally, the uncertainty in the velocity vector is expressed directly as a combination of the position uncertainty in the matching pair of particles. The methodology is described in detail in the next section.

4.2 Methodology

The primary relation between the observed image coordinate (X, Y) and the expected particle world coordinate (x_w, y_w, z_w) in physical space is given by the individual camera mapping function FX^c for each camera c , as given in equation (37).

$$\begin{aligned}
X^c = FX^c(x_w, y_w, z_w, a_i) = & a_1 + a_2x_w + a_3y + a_4z + a_5x_w^2 + a_6x_wy_w + a_7y_w^2 \\
& + a_8x_wz_w + a_9y_wz_w + a_{10}z_w^2 + a_{11}x_w^3 + a_{12}x_w^2y_w + a_{13}x_wy_w^2 \\
& + a_{14}y_w^3 + a_{15}x_w^2z_w + a_{16}x_wy_wz_w + a_{17}y_w^2z_w + a_{18}x_wz_w^2 + a_{19}y_wz_w^2
\end{aligned} \tag{37}$$

Typically, a polynomial mapping function is used following Soloff et al. [5] to have higher accuracies in the presence of optical distortion effects. Once a mapping function is established and iteratively corrected using self-calibration process, the reconstruction process involves finding an inverse of the mapping function for the matching particle image coordinates in different projections. Hence an error propagation through the mapping function is the starting point of the uncertainty quantification and is described in the next subsection.

4.2.1 Error propagation through the mapping function

An error propagation for equation (37) can be written as follows:

$$e_{X^c} = \frac{\partial FX^c}{\partial x_w} e_{x_w} + \frac{\partial FX^c}{\partial y_w} e_{y_w} + \frac{\partial FX^c}{\partial z_w} e_{z_w} + \frac{\partial FX^c}{\partial a_i} e_{a_i} \tag{38}$$

Equation (38) is obtained as a Taylor series expansion of equation (37), neglecting the higher order terms. Thus, the error in image coordinate e_{X^c} can be related to the error in world coordinate positions $e_{x_w}, e_{y_w}, e_{z_w}$ and the error in calibration function coefficients e_{a_i} through the mapping function gradients $\left(\frac{\partial FX^c}{\partial x_w}, \frac{\partial FX^c}{\partial y_w}, \frac{\partial FX^c}{\partial z_w}, \frac{\partial FX^c}{\partial a_i}\right)$. A similar propagation equation can be written for the error in Y (e_{Y^c}) image coordinate for each camera mapping function. It is important to note that the quantities of interest are $e_{x_w}, e_{y_w}, e_{z_w}$ as we seek to estimate the unknown variance in the reconstructed world coordinate positions. Rearranging the unknown terms in the left-hand side and multiplying each side by its transpose yields the variance propagation equation as follows:

$$\begin{aligned}
& \left(\frac{\partial FX^c}{\partial x_w} e_{x_w} + \frac{\partial FX^c}{\partial y_w} e_{y_w} + \frac{\partial FX^c}{\partial z_w} e_{z_w}\right) \left(\frac{\partial FX^c}{\partial x_w} e_{x_w} + \frac{\partial FX^c}{\partial y_w} e_{y_w} + \frac{\partial FX^c}{\partial z_w} e_{z_w}\right)^T \\
& = \left(e_{X^c} - \frac{\partial FX^c}{\partial a_i} e_{a_i}\right) \left(e_{X^c} - \frac{\partial FX^c}{\partial a_i} e_{a_i}\right)^T
\end{aligned} \tag{39}$$

The error in particle image position estimation (e_{X^c}) is a function of particle image fitting error and can be assumed to be independent of the error in calibration function coefficients (e_{a_i}). However, the calibration error can influence the error in projected particle image location or the

projection error and thus any covariance between e_{X^c} and e_{a_i} is implicitly accounted in the projection error formulation, as discussed in section 4.2.2. With these considerations, a simplified version of equation (39) can be written as shown in equation (40).

$$\begin{bmatrix} \frac{\partial FX^c}{\partial x_w} & \frac{\partial FX^c}{\partial y_w} & \frac{\partial FX^c}{\partial z_w} \end{bmatrix} \Sigma_{\vec{x}_w} \begin{bmatrix} \frac{\partial FX^c}{\partial x_w} & \frac{\partial FX^c}{\partial y_w} & \frac{\partial FX^c}{\partial z_w} \end{bmatrix}^T = \sigma_{X^c}^2 + C_{\vec{a}} \Sigma_{\vec{a}}^c C_{\vec{a}}^T \quad (40)$$

Here, $\begin{bmatrix} \frac{\partial FX^c}{\partial x_w} & \frac{\partial FX^c}{\partial y_w} & \frac{\partial FX^c}{\partial z_w} \end{bmatrix}$ is a row vector containing mapping function gradients for each camera c with respect to $\vec{x}_w = \{x_w, y_w, z_w\}$ and $\Sigma_{\vec{x}_w}$ represents the unknown covariance matrix in world coordinates ($\Sigma_{\vec{x}_w} = \{e_{x_w} \ e_{y_w} \ e_{z_w}\}^T \{e_{x_w} \ e_{y_w} \ e_{z_w}\}$). The uncertainty in particle image position X^c is denoted by σ_{X^c} . The term $C_{\vec{a}} \Sigma_{\vec{a}}^c C_{\vec{a}}^T$ evaluates to a single numerical value, which accounts for the contribution from the uncertainty in the calibration coefficients $\vec{a} = \{a_i\}_{1 \times 19}$, for the mapping function FX^c of camera c . $C_{\vec{a}} = \begin{bmatrix} \frac{\partial FX^c}{\partial a_i} \end{bmatrix}_{1 \times 19}$ represents the mapping function gradients with respect to the calibration coefficients \vec{a} and the covariance in mapping function coefficients is denoted by $\Sigma_{\vec{a}}^c = \{e_{a_i}\} \{e_{a_i}\}_{19 \times 19}^T$. For solving equation (40), it can be written as a stack of 8 rows of equations corresponding to X and Y mapping functions for each of, for example, a four-camera set-up. The combined equation for all cameras is given by equation (41) and is solved for each reconstructed particle individually.

$$C_{\vec{x}_w} \Sigma_{\vec{x}_w} C_{\vec{x}_w}^T = \Sigma_{\vec{X}} + \Sigma_{\vec{a}} \quad (41)$$

In equation (41), $C_{\vec{x}_w}$ is an 8×3 coefficient matrix containing mapping function gradients for the 8 mapping functions. The combined variance matrix in particle image position $\vec{X} = \{X^c, Y^c\}$ is denoted by $\Sigma_{\vec{X}}$ and contains $\sigma_{X^c}^2$ and $\sigma_{Y^c}^2$ as diagonal entries for each camera. The correlation in e_{X^c} between different camera components is seen to be negligible and thus the off-diagonal terms of $\Sigma_{\vec{X}}$ are set to zero. Lastly, the evaluated values of $C_{\vec{a}} \Sigma_{\vec{a}}^c C_{\vec{a}}^T$ for each mapping function in equation (40) are put as the diagonal terms in the $\Sigma_{\vec{a}}$ matrix ($(\Sigma_{\vec{a}})_{ii} = C_{\vec{a}} \Sigma_{\vec{a}}^c C_{\vec{a}}^T$), which represents the net calibration uncertainty contribution across all 4 cameras. Thus, equation (41) contains the unknown covariance matrix in world coordinates $\Sigma_{\vec{x}_w}$ as a function of $\Sigma_{\vec{X}}$ and $\Sigma_{\vec{a}}$. The following sections focus on estimating the $\Sigma_{\vec{X}}$ and $\Sigma_{\vec{a}}$ terms.

The overview of the uncertainty estimation and propagation process is depicted in Figure 4.2.

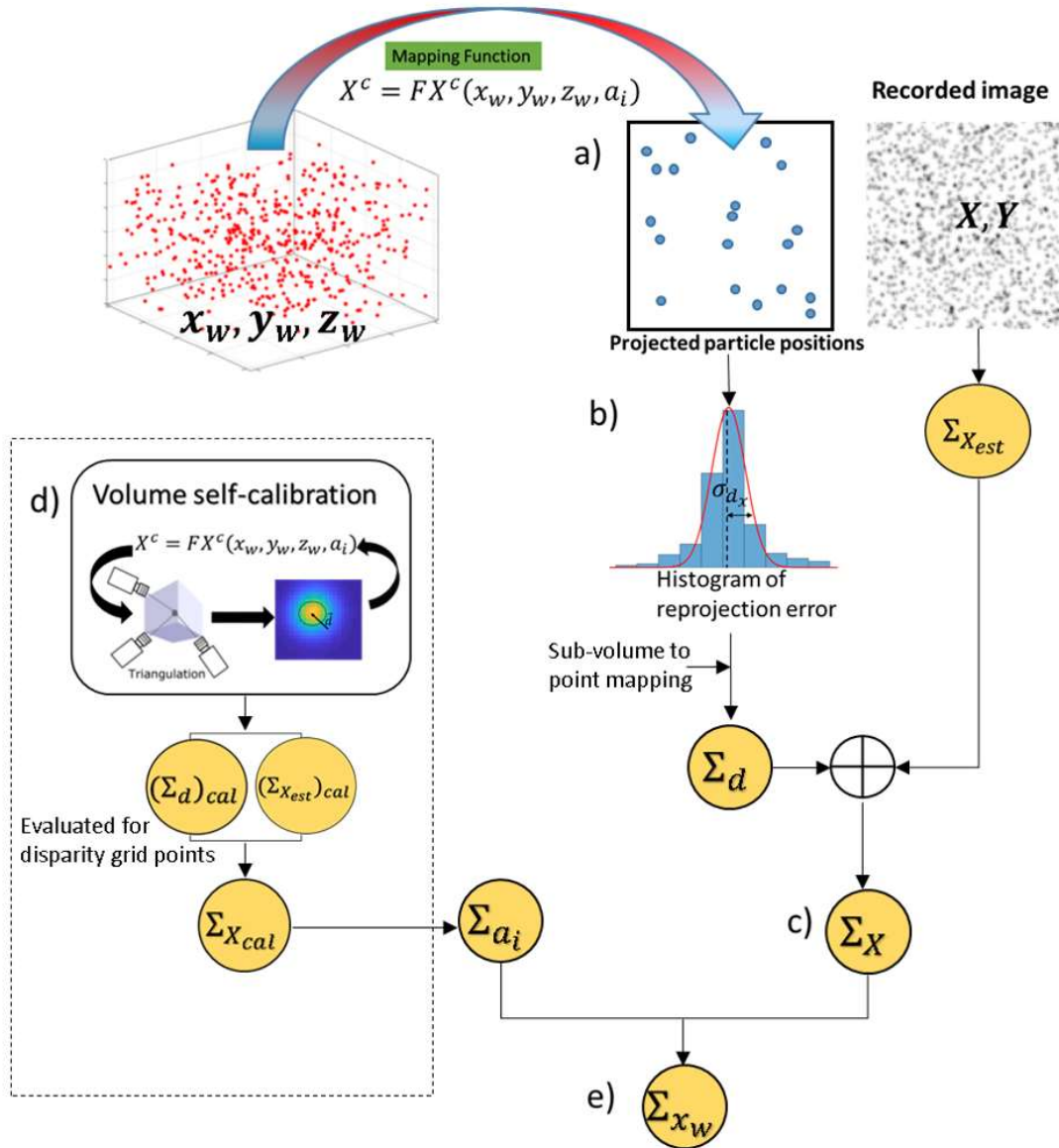


Figure 4.2. A schematic showing different steps (a – e) for estimating elemental uncertainties in particle image location X and calibration coefficients a_i and its propagation to the uncertainty in the world coordinate x_w .

4.2.2 Estimating uncertainty in particle image location

For a-posteriori uncertainty quantification, we start from a reconstructed 3D particle positions obtained either from a triangulation or IPR reconstruction method. For a given 3D particle position,

we want to find the corresponding projected particle image locations and its uncertainty for each camera. As shown in Figure 4.2a), the projected particle image positions are compared with the recorded image to find the error in particle image location. This can be expressed as a sum of the estimated projection error ($\vec{X}_{proj} - \vec{X}_{est}$) and the 2D particle fit position estimation error ($\vec{X}_{est} - \vec{X}_{true}$), for all $\vec{X} = \{X^c, Y^c\}$ and for each camera c , as shown in equation (42).

$$e_{\vec{X}} = \vec{X}_{proj} - \vec{X}_{true} = \vec{X}_{proj} - \vec{X}_{est} + \vec{X}_{est} - \vec{X}_{true} \quad (42)$$

Thus, the variance in particle image location, $\Sigma_{\vec{X}}$, becomes a sum of the variance in the estimated projection error, denoted by $\Sigma_{\vec{d}}$, and variance of the error in particle image position estimation.

$$\Sigma_{\vec{X}} = e_{\vec{X}} e_{\vec{X}}^T = \Sigma_{\vec{d}} + \Sigma_{\vec{X}_{est}} \quad (43)$$

As mentioned in section 4.2.1 equation (41), each of these variance matrices consider only the diagonal terms corresponding to X and Y mapping functions for each camera. In order to estimate $\Sigma_{\vec{d}}$ the reconstruction domain is divided into sub-volumes and the estimated projection error for a group of particles belonging to the same sub-volume are stacked up into a histogram (this relates to the concept of disparity(\vec{d}) defined by Wieneke [6]). The sub-volume size can be varied or particles from other frames can be included to have a larger statistical sample. It is observed that a histogram consisting of 50 or more particles in the sub-volume yields a statistically consistent estimate, irrespective of the number of sub-volumes considered. Such a histogram of disparity(\vec{d}) estimates is shown in Figure 4.2b), where the variance in the estimated X projection error is denoted by σ_{d_X} . For a perfectly converged self-calibration, the mean disparity (\bar{d}) should be zero. Typically, the disparity histogram approaches a Gaussian distribution and for the robustness of variance estimation a Gaussian fit is applied on this histogram. The estimated standard deviation from the fitted curve is used to evaluate the variance of the disparity distribution. However, for a lower seeding density the disparity distribution is observed to deviate from a Gaussian distribution. Consequently, if the area under the fitted Gaussian curve is different by more than 5% compared to the histogram area evaluated using trapezoidal integration rule, the standard deviation of the distribution is used as the standard uncertainty. In this framework, this

estimated variance is modeled as the desired $\Sigma_{\vec{a}}$ of equation (43). For the particles belonging to the same sub-volume, the same value of $\Sigma_{\vec{a}}$ is used.

Each particle image within ± 0.5 pixels of the projected 3D particle location is fitted with a Gaussian shape and thus the uncertainty in the fitted position parameter for the least square fit process is considered as $\Sigma_{\vec{x}_{est}}$. Equation (44) denotes an expression for the position estimation variance which is shown to be a function of the variance in the fit residual error (σ_{res}^2) and the Jacobian(J) of the residual at the solution point (I denotes an identity matrix). This is consistent with the Cramer-Rao lower bound (CRLB) determination for 2D particle image centroid, as highlighted by Rajendran et al. [33]. Hence, once $\Sigma_{\vec{a}}$ and $\Sigma_{\vec{x}_{est}}$ are estimated, the $\Sigma_{\vec{x}}$ is known (Figure 4.2c).

$$\Sigma_{\vec{x}_{est}} = (J^T J)^{-1} \sigma_{res}^2 I \quad (44)$$

4.2.3 Estimating the uncertainty in mapping function coefficients

As seen from the flowchart in Figure 4.2, once the variance in particle image position ($\Sigma_{\vec{x}}$) is estimated through the progression of steps shown on the right side, the next workflow is focused on estimating the variance in the calibration coefficients ($\Sigma_{\vec{a}}$). The overall calibration uncertainty $\Sigma_{\vec{a}}$ is a combination of $\Sigma_{\vec{a}}^c$ for each camera c . The $\Sigma_{\vec{a}}^c$ estimation process (Figure 4.2d) can be performed in conjunction with the volumetric self-calibration process. In absence of self-calibration, the uncertainty in the coefficients a_i is dictated by the uncertainty in calibration image dot fitting. However, the presence of disparity between estimated and projected points leads to a shift in the projected grid points (X_{cal}, Y_{cal}) in the image domain, this correction leads to a new set of coefficients (a_i) in the self-calibration process. Hence, the uncertainty in X_{cal}, Y_{cal} positions, namely $\Sigma_{\vec{x}_{cal}}$, should directly affect the $\Sigma_{\vec{a}}^c$. If we consider the world coordinate positions ($x_{cal}, y_{cal}, z_{cal}$) where the disparity vectors are evaluated, then those grid points being specific locations in space, will have no uncertainty in their location. Consequently, the unknowns ($e_{x_w}, e_{y_w}, e_{z_w}$) of equation (39) can be simplified to zero and the equation can be simplified to equation (45).

$$\Sigma_{\vec{x}_{cal}} = \left(\frac{\partial FX}{\partial a_i} e_a \right) \left(\frac{\partial FX}{\partial a} e_{a_i} \right)^T = C 1_{\vec{a}} \Sigma_{\vec{a}}^c C 1_{\vec{a}}^T \quad (45)$$

In this equation, the $C1_{\bar{a}}$ represents the matrix of gradients of the mapping function with respect to the coefficients a_i , having number of rows corresponding to number of disparity grid points. The variance in the particle image position $\Sigma_{\bar{x}_{cal}}$ can be evaluated in a similar way as mentioned in section 4.2.2. Here, the $\Sigma_{\bar{x}_{cal}}$ can be evaluated for the initially triangulated particle positions and is used in equation(45) to solve for $\Sigma_{\bar{a}}^c$ as a least squares problem for all disparity grid points.

4.2.4 Uncertainty propagation in reconstructed positions

The uncertainty in the reconstructed world coordinate position is finally obtained by solving for the world coordinate location covariance matrix $\Sigma_{\bar{x}_w}$ from equation (41), as shown in Figure 4.2e). This equation is evaluated for each world coordinate position combining mapping functions in X and Y for all four cameras. The estimated covariance $\Sigma_{\bar{a}}^c$ term in section 4.2.3 is used to evaluate $C_{\bar{a}}\Sigma_{\bar{a}}^cC_{\bar{a}}^T$, where $C_{\bar{a}}$ represents $\frac{\partial FX^c}{\partial a_i}$ for each camera c , as mentioned in equation (40). The $\Sigma_{\bar{a}}$ term is then evaluated as a diagonal matrix as $(\Sigma_{\bar{a}})_{ii} = C_{\bar{a}}\Sigma_{\bar{a}}^cC_{\bar{a}}^T$. The $\Sigma_{\bar{x}}$ has already been calculated using equation (43). Hence, we solve for $\Sigma_{\bar{x}_w}$ by inverting the $C_{\bar{x}_w}$ matrix as shown in equation (46).

$$\Sigma_{\bar{x}_w} = B (\Sigma_{\bar{x}} + \Sigma_{\bar{a}}) B^{-1} \quad (46)$$

Where, B is given by $B = (C_{\bar{x}_w}^T C_{\bar{x}_w})^{-1} C_{\bar{x}_w}^T$. It can be noted that for standard Gaussian particle images, the covariance between X and Y particle image position estimation can be assumed to be negligible. However, in presence of optical distortion, such a covariance can be estimated from the 2D least square fit of an elliptical Gaussian function on the mean particle image shape. Thus, the term $(\Sigma_{\bar{x}} + \Sigma_{\bar{a}})$ is essentially an 8x8 diagonal matrix for 8 mapping function equations. From the covariance matrix $\Sigma_{\bar{x}_w}$, the standard uncertainty in reconstructed positions $(\sigma_{x_w}, \sigma_{y_w}, \sigma_{z_w})$ are obtained by taking the square root of the diagonal terms $(\sqrt{(\Sigma_{\bar{x}_w})_{ii}})$.

We also evaluate the bias uncertainty terms $\sigma_{x_b}, \sigma_{y_b}, \sigma_{z_b}$ based on the mean disparity value for each subvolume. Ideally, for a converged self-calibration the mean disparity is negligible. However, due to measurement noise, any residual mean disparity (\bar{d}) can lead to a bias in the reconstructed position measurement. We estimate \bar{d} from the disparity histogram and use that to

estimate $\Sigma_{\vec{x}_b}$, the bias uncertainty in particle image position and $\Sigma_{\vec{a}_b}^c$, the bias uncertainty in a_i 's using the propagation equations (43) and (45). For $\Sigma_{\vec{x}_b}$, only $\Sigma_{\vec{a}_b}$ is considered in equation (43). The final bias uncertainty estimates for reconstructed x, y, z positions are obtained using the propagation equation (46) by substituting the values of $\Sigma_{\vec{x}_b}$ and $\Sigma_{\vec{a}_b}$.

4.2.5 Uncertainty in estimated velocity field

The uncertainty in each tracked 3D velocity measurement is evaluated as a direct combination of the estimated 3D position uncertainties of each paired particle. Thus, if a particle in frame 1 ($\sigma_{x_{w1}}, \sigma_{y_{w1}}, \sigma_{z_{w1}}$) is paired with a particle in frame 2, then the uncertainty in the tracked displacement σ_u is given by

$$\sigma_u^2 = \sigma_{x_b}^2 + \sigma_{x_{w1}}^2 + \sigma_{x_{w2}}^2 - \rho_{x_{w1}x_{w2}} \sigma_{x_{w1}} \sigma_{x_{w2}} \quad (47)$$

In equation (47), σ_{x_b} is the bias uncertainty term as evaluated in section 4.2.4. The bias uncertainty depends on the mean disparity and the mapping function coefficients and is not expected to change from frame to frame. Hence it is accounted for only once in the tracking uncertainty estimation. It is also observed that the true position error in the estimated 3D particle position for a paired particle in frame 1 and frame 2 has a strong correlation. Thus, the covariance term $\rho_{x_{w1}x_{w2}} \sigma_{x_{w1}} \sigma_{x_{w2}}$ in equation (47) is significant. The correlation coefficient $\rho_{x_{w1}x_{w2}}$ varies from about 0.5 to 0.8, depending on the flow field and calibration and is estimated as an average of the correlation of the individual camera disparity error between paired particles. The $\rho_{x_{w1}x_{w2}}$ term can be computed for each pair of frames and also for a statistically significant number of particles within the same sub-volume. However, if the spatio-temporal variations of $\rho_{x_{w1}x_{w2}}$ is within 5% of the mean value, then an average coefficient may be used to calculate the covariance term. The disparity error correlation is expected to have a similar magnitude compared to the true position error correlation between frames and is verified to be the case for synthetic test cases with true error quantification. The uncertainty in v and w components (σ_v, σ_w) can be obtained in a similar way following equation (47). It is to be noted, that the uncertainty due to false matching in presence of ghost particles may need further analysis. However, for a valid measurement we expect equation (47) to account for the uncertainty in the tracked velocity measurement.

4.3 Results

The proposed framework to estimate the uncertainty in the reconstructed particle positions is tested using synthetic vortex ring images. The particle field was generated and advected using incompressible axisymmetric vortex ring equations mentioned in [34]. The camera calibration and particle images (256x256 pixels) were generated using in-house code. The camera angles were selected as 35° and were positioned in a plus (+) configuration. The volume of interest was set to 42mmx42mmx24mm and the seeding density was varied from 0.01ppp to 0.1ppp. The processing was also done using in-house calibration and IPR code for 100 image pairs. A polynomial model was used for the camera calibration and the initial estimate of the calibration was modified by 3 iterations of volumetric self-calibration to eliminate any mean disparity. An allowable triangulation error of 1 pixel was used for initial triangulation with particle identification using dynamic particle segmentation method [8] to better resolve overlapping particle images. The particle image positions were estimated using least square Gaussian fit. The optical transfer function (OTF) [35] was calculated and used in IPR iterations. The number of inner loop and outer loop iterations for each frame was set to 4 with particle “shaking” of ± 0.1 voxels. The 3D particle tracking was done using “nearest neighbor” algorithm. The uncertainty for each measurement was computed using the set of equations described in section 4.2.

4.3.1 Comparing error and uncertainty histogram for reconstructed particle positions

First, the uncertainty in reconstructed particle positions are analyzed. The reconstructed particle positions are compared with the true particle positions in space and if a particle is found within 1 voxel radius of the true particle, then it is considered as a valid reconstruction. The error in reconstructed x_w position is denoted by e_{x_w} and defined as:

$$e_{x_w} = x_w^{estimated} - x_w^{true} \quad (48)$$

Similarly, e_{y_w} and e_{z_w} are defined. Figure 4.3 shows the histogram of error and uncertainty distributions x_w , y_w and z_w coordinates. Figure 4.3a and Figure 4.3b shows the distributions for the reconstructed particle positions obtained using triangulation and IPR methods respectively, for a particle concentration of 0.05ppp. The x-axis is divided into 60 equally spaced bins and the y-

axis denotes the number of measurements falling within each bin as a fraction of total number of points. The root mean squared (RMS) error is defined as:

$$RMS\ error = \sqrt{\frac{1}{N} \sum_{i=1}^N e_{i_w}^2} \quad (49)$$

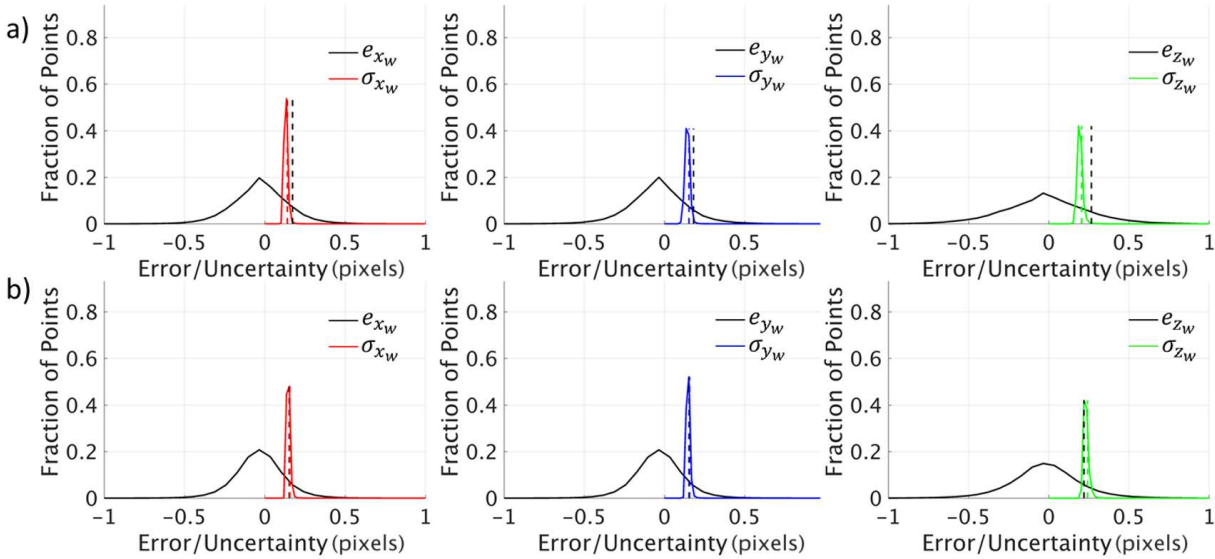


Figure 4.3. Histogram of error (e) and uncertainty (σ) distributions for reconstructed particle positions (x_w, y_w, z_w) for the synthetic vortex ring case with 0.05ppp particle concentration for a) triangulation and b) IPR reconstructions. The vertical lines indicate the RMS value for each distribution.

The error distribution for the triangulated particle positions is wider with RMS error of about 0.17, 0.18 and 0.27 pixels in x_w, y_w and z_w positions compared to RMS error of 0.15, 0.15 and 0.22 pixels for the IPR case. The predicted uncertainty distributions have significantly less spread and have a tight distribution around the RMS error. For a successful prediction, it is expected that the RMS value of the error distribution should match the RMS value of the estimated uncertainty distribution [29]. The RMS value for each distribution is indicated by the dashed vertical line. For Figure 4.3a, the RMS uncertainty values underpredict the RMS error by 0.03 pixels in x_w and y_w and by 0.06 pixels in z_w . For IPR case in Figure 4.3b, the predicted uncertainties are within 0.02 pixels of the RMS error values. Overall, the predicted uncertainties

are in close agreement with the expected value, indicating a successful prediction for position reconstruction uncertainty.

4.3.2 Reconstructed position uncertainty for varying particle concentration

The increase in particle concentration leads to a higher percentage of overlapping particles which increases the error in particle identification, and subsequently in 3D particle reconstruction. To test

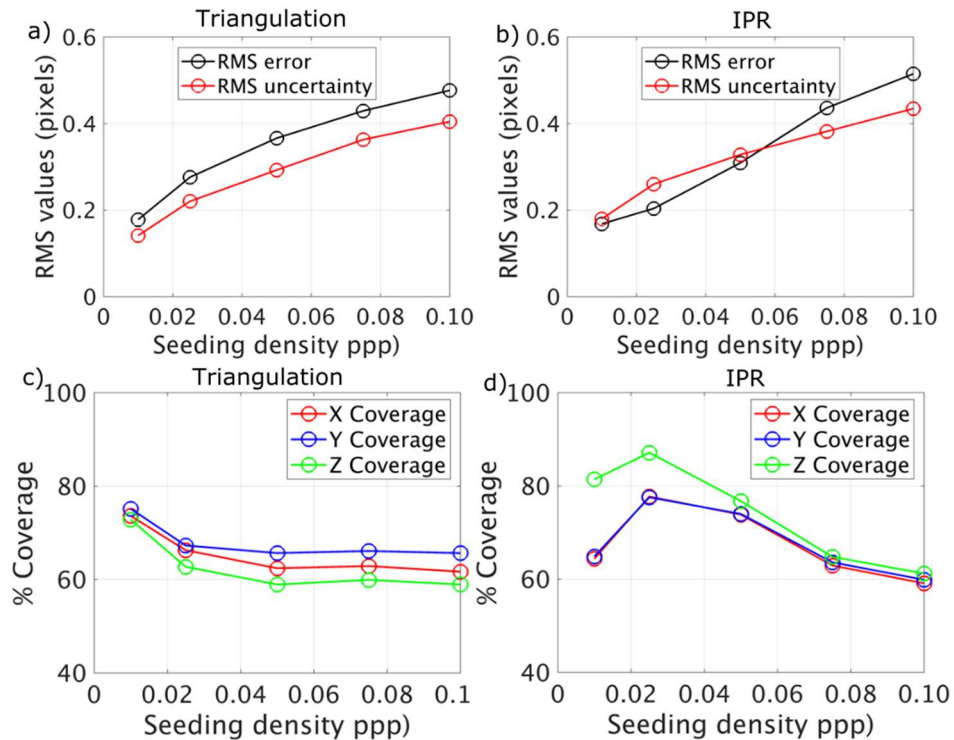


Figure 4.4. Comparison of triangulation and IPR reconstructed position error and uncertainty as a function of seeding density for the synthetic vortex ring case. Plot a) compares the RMS error and RMS of predicted uncertainties for seeding densities in the range of 0.01ppp to 0.1ppp and plot b) compares the coverage in each case.

the sensitivity of the uncertainty predictions in such scenarios, the seeding density is varied from 0.01ppp to 0.1ppp and the RMS error and uncertainty values are compared in each case, as shown in Figure 4a and Figure 4b. The results show a high sensitivity of the predicted uncertainty to the trend of the RMS error for both triangulation and IPR methods. The reconstructed position RMS error predicted by IPR is lesser than the triangulation error for lower seeding densities, whereas, for 0.1ppp the IPR error is higher, which may be related to the specifics of the in-house IPR implementation. However, the objective is to predict the correct RMS error level given the

different reconstructed positions using different methodologies. For triangulation the RMS uncertainty follows the RMS error trend consistently, but underpredicts the magnitude by about 0.04 pixels (23%) at 0.01ppp and by 0.07 pixels (20%) at 0.1ppp. For the IPR case, the predicted uncertainty matches the expected uncertainty value closely at 0.01ppp and 0.05ppp with a deviation of about 0.01 pixels (10%), but underpredicts the uncertainty by 0.08 pixels (30%) at 0.1ppp. Overall the increasing trend agreement, between the predicted and the expected uncertainty validates the current framework for prediction of uncertainty for a wide range of particle concentrations and using both reconstruction methods.

For a more specific comparison across seeding densities, the values of RMS errors and uncertainties in x_w , y_w and z_w positions for both methods have been presented in Table 4.1. The maximum underprediction of about 0.06 pixels occurs at 0.1ppp case for both methods. The best agreement is obtained for the IPR case for up to 0.05ppp and for the triangulation case upto

Table 4.1. Comparison of RMS error and RMS uncertainty values for the triangulation and IPR based reconstructed particle positions for a range of seeding densities.

Particle Concentration (ppp)	RMS e_{x_w} (voxels)	RMS σ_{x_w} (voxels)	RMS e_{y_w} (voxels)	RMS σ_{y_w} (voxels)	RMS e_{z_w} (voxels)	RMS σ_{z_w} (voxels)
Triangulation Reconstruction						
0.010	0.08	0.07	0.09	0.07	0.13	0.10
0.025	0.13	0.11	0.14	0.11	0.20	0.16
0.050	0.17	0.14	0.18	0.15	0.27	0.21
0.075	0.21	0.17	0.22	0.19	0.31	0.25
0.100	0.23	0.19	0.24	0.22	0.34	0.28
IPR Reconstruction						
0.010	0.09	0.08	0.09	0.09	0.11	0.13
0.025	0.11	0.12	0.11	0.12	0.14	0.19
0.050	0.15	0.16	0.15	0.16	0.22	0.24
0.075	0.22	0.18	0.22	0.18	0.31	0.28
0.100	0.26	0.21	0.26	0.21	0.36	0.32

0.025ppp. It is to be noted that the IPR reconstruction error is higher than expected, which may be related to a lower convergence rate and in turn depends on the specifics of the implementation, however, given a reconstructed field the current method reasonably predicts the standard uncertainty in 3D particle based reconstruction.

To compare the global prediction of uncertainty level for all particles the estimated coverage is plotted in Figure 4c and Figure 4d. The coverage is defined as the percentage of

measurement errors falling within the uncertainty bound ($\pm\sigma$). For an ideal Gaussian error distribution, the standard uncertainty coverage is 68.3%. In Figure 4c, the coverage for all cases lies within 60% to 68%, except for 0.01 ppp for which case the coverage is about 74% for triangulation. The deviation for lower seeding density case may be related to the non-Gaussian nature of the error distributions at such particle concentrations. For IPR the coverage varies from 60% to 87%, with maximum overprediction for the 0.025ppp case, as shown in Figure 4d. Thus, the uncertainty coverage metric is mostly in the range of 60% to 73% in the present analysis and agrees well with the ideal expected coverage of 68.3%.

4.3.3 Uncertainty prediction for tracked velocity vectors

As a final step, the uncertainty prediction in the tracked velocity field is assessed. The reconstructed 3D particle positions are tracked for a pair of frames for 100 pairs using nearest-neighbor tracking. The true particle positions in 1 voxel vicinity of the reconstructed particle positions is found for the first frame and the corresponding true displacement is subtracted from the estimated displacement to compute the error (e) in u , v and w velocity components. A measurement is considered valid if the computed error magnitude is within 1 voxel. The uncertainty ($\sigma_u, \sigma_v, \sigma_w$) in the velocity components are computed using equation (47).

The RMS uncertainty values mentioned in Table 4.2 are in close agreement with the RMS error values with a maximum deviation of 0.04 pixels across all cases. The RMS error increases with the particle concentration due to higher probability of erroneous matches resulting from ghost particle reconstruction. The predicted uncertainty increases proportionally with RMS error, for both reconstruction methods, as observed in Table 4.2.

The histogram of velocity error and uncertainty distribution is compared in Figure 4.5a for the triangulation case and Figure 4.5b for the IPR case, for 0.05ppp seeding density. The error distribution is sharper for the triangulation case. It is noticed that the w component has higher error compared to u and v components. For all cases, the uncertainty distributions have a very narrow spread and predicts the RMS error magnitude perfectly. Further analysis for higher seeding densities with STB processing is required to validate the displacement uncertainty model proposed by equation (47), however, these results show reasonable agreements between predicted and expected uncertainty values for the estimated velocity components.

Table 4.2. Comparison of RMS error and RMS uncertainty values for the particle tracking displacement estimates using triangulation and IPR based reconstructed particle positions for a range of seeding densities.

Particle Concentration (ppp)	RMS e_u (voxels /frame)	RMS σ_u (voxels /frame)	RMS e_v (voxels /frame)	RMS σ_v (voxels /frame)	RMS e_w (voxels /frame)	RMS σ_w (voxels /frame)
Triangulation Reconstruction						
0.010	0.06	0.05	0.07	0.05	0.10	0.07
0.025	0.09	0.08	0.09	0.08	0.14	0.11
0.050	0.11	0.11	0.12	0.12	0.18	0.16
0.075	0.13	0.15	0.14	0.16	0.20	0.21
0.100	0.14	0.17	0.15	0.19	0.22	0.25
IPR Reconstruction						
0.010	0.12	0.08	0.12	0.09	0.13	0.13
0.025	0.12	0.11	0.12	0.11	0.14	0.17
0.050	0.16	0.14	0.16	0.14	0.22	0.22
0.075	0.22	0.18	0.22	0.18	0.30	0.28
0.100	0.25	0.21	0.25	0.22	0.34	0.33

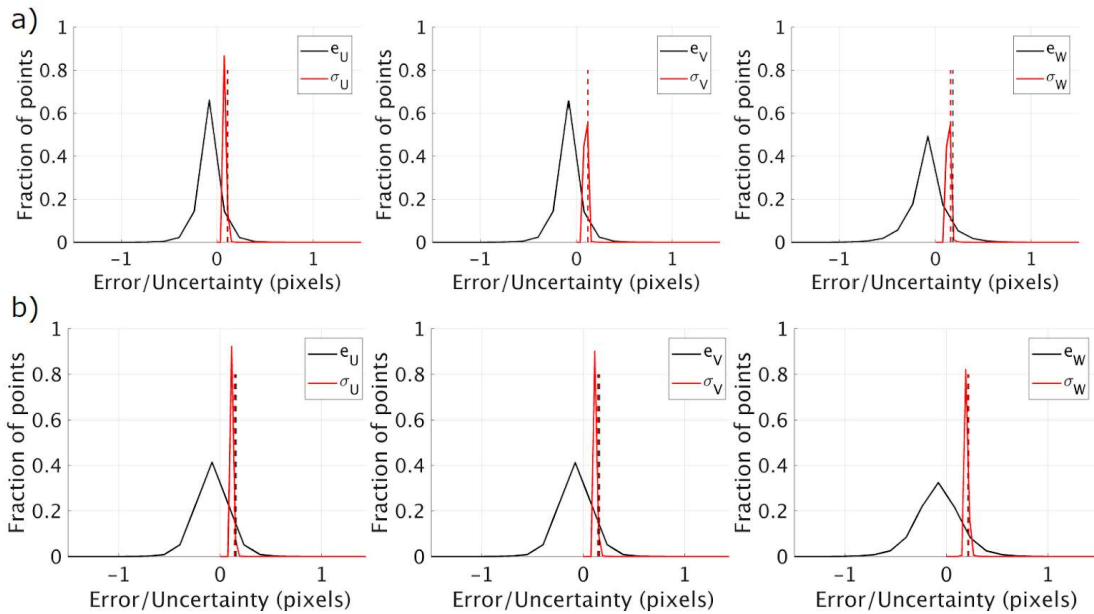


Figure 4.5. Error and uncertainty histogram comparison for tracked velocity vectors in the synthetic vortex ring case with seeding density of 0.05ppp for a) triangulation based reconstruction and for b) IPR based reconstruction.

4.3.4 Experimental Validation: Uncertainty prediction for laminar pipe flow

The current framework is also validated for a canonical laminar pipe flow experiment for a Reynolds number of 630. The schematic of the experimental set up is shown in Figure 4.6. The

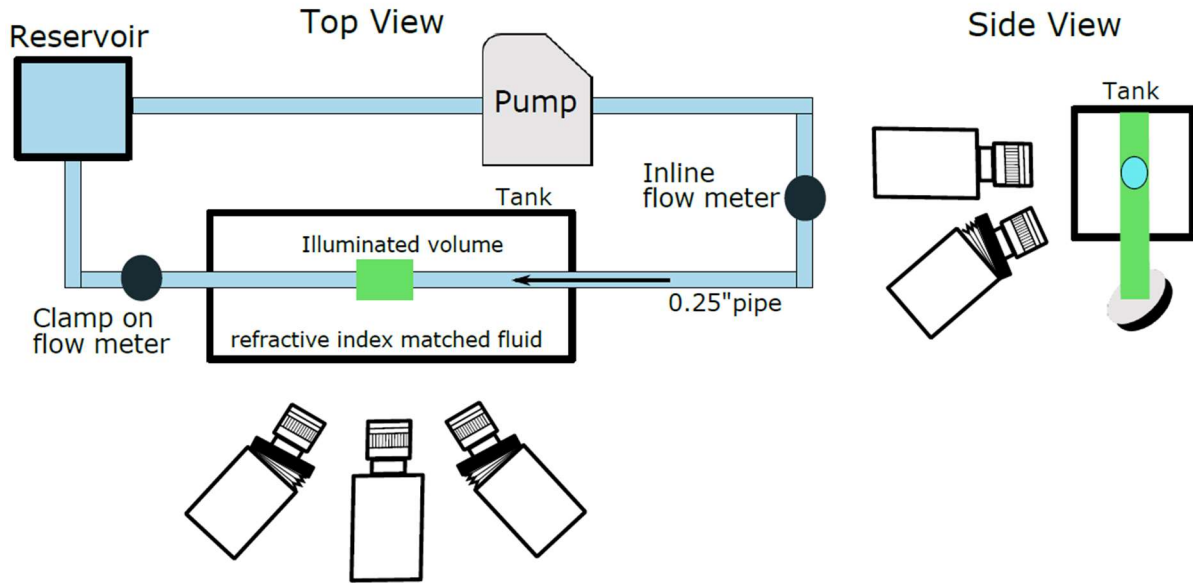


Figure 4.6. Schematic of laminar pipe flow set up showing the flow loop and camera arrangement.

flow loop consisted of a gear pump driving a steady flow rate of 0.17 L/min through a circular FEP tube of 0.25 inches diameter. The working fluid inside the pipe was chosen as distilled water-urea (90:10) solution with a density of 1015 kg/m³ and dynamic viscosity of 0.915 mPas. The tube was fully immersed in an acrylic tank filled with water-glycerol solution such that it is refractive index matched. The volumetric PTV measurement was performed using four Phantom Miro M340 cameras with three cameras at the same horizontal plane and one camera angled in the vertical plane, as shown in the sideview of Figure 4.6. The flow rate in the upstream and downstream of the pipe was measured using an ultrasonic flowmeter and the average flow rate was used to determine the true velocity profile. The measurement volume was 9x6.5x6.5 mm³ and was illuminated by a continuum Terra-PIV laser with appropriate optical setup. The time-resolved measurements were taken at 6 kHz, and the image size was 640x624 pixels with an average magnification of 17.8 microns/pixel. 24-micron fluorescent particles were used with a particle Stokes number $St = 0.0005$. The particle images were processed using in-house camera calibration,

particle reconstruction and tracking code. A polynomial mapping function [5] was used to establish a relation between image coordinates and physical coordinates. Three iterations of volumetric self-calibration [6] were done to eliminate any disparity between the measurement volume and calibration target location or alignment. Both triangulation and IPR was used to reconstruct the particle positions in physical coordinate system and subsequently the 3D particle locations were tracked using a “nearest-neighbor” pairwise tracking algorithm. 500 pairs of images were processed with a particle concentration of 0.005ppp.

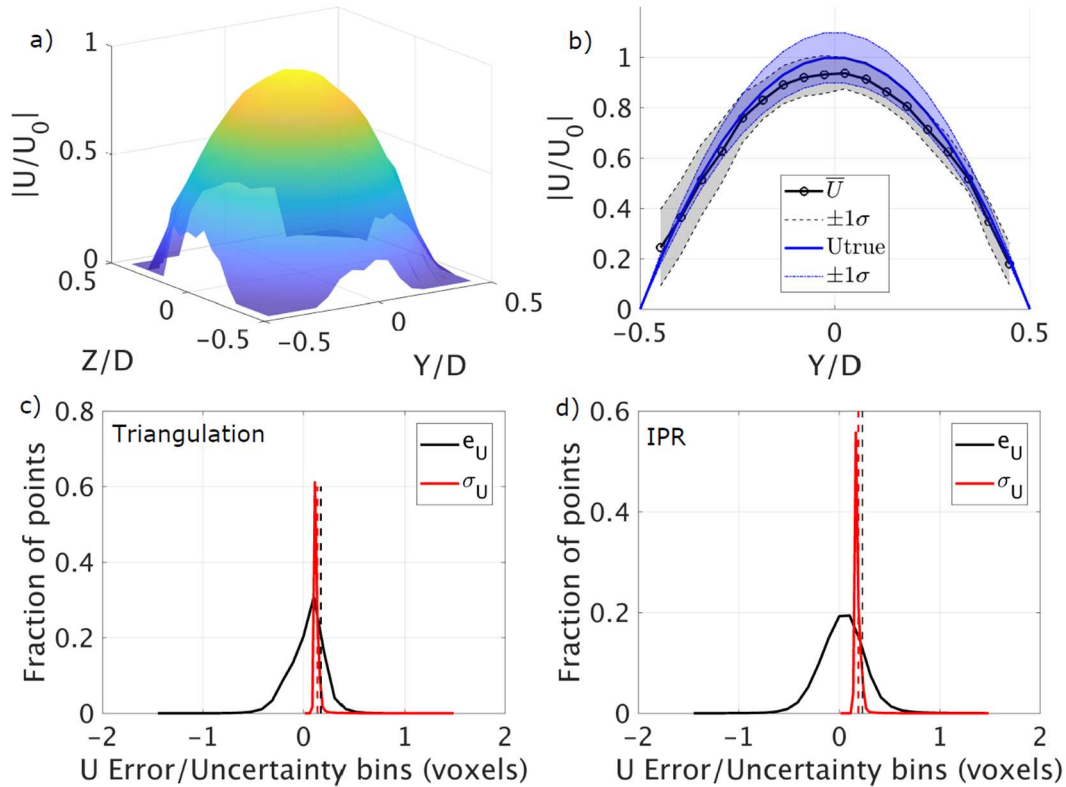


Figure 4.7. The mean streamwise velocity profile for a 3D PTV measurement of a laminar pipe flow is shown in a). The velocity profile is compared with the true solution in b). The error and estimated uncertainty histogram are shown for triangulation-based reconstruction in c) and for IPR based reconstruction in d).

The reconstructed particle positions across all images are summed up in the cross-sectional view of the tube and a least square circular fit is performed to fit a circle with size closest to the diameter of the tube. The fitted boundary is used to divide the cross-sectional area of the tube in 20x20 bins and all measurements in streamwise direction as well as across 500 frames are averaged

per bin to obtain the mean velocity profile shown in Figure 4.7a. The mean velocity profile along the middle y-plane is compared with the true solution in Figure 4.7b. The expected true velocity profile U_{true} for the measured flow rate is shown by the blue solid line. The flow meter has a 10% uncertainty and its corresponding standard uncertainty ($\pm\sigma$) is shown by the blue shaded region. The mean velocity profile obtained from particle tracks (for the triangulation case) is shown by the black solid line and the standard deviation of the velocity measurements in each bin is shown by the shaded grey region. The peak measured velocity reaches 94% of the true maximum velocity. The standard deviation of the measured velocity is observed to increase in the depth direction moving away from the camera. Overall, the mean velocity profile agreed with the expected parabolic profile of a laminar pipe flow.

The measured streamwise component of velocity (U) is compared with the true expected velocity (U_{true}) and the distribution of velocity tracking error e_U and the estimated corresponding uncertainty σ_U is shown in Figure 4.7c and Figure 4.7d for the triangulation and IPR reconstruction cases respectively. In both cases the error distribution is skewed with a higher bias error for the triangulation case of about 0.1 pixels/frame. The predicted uncertainty values are distributed closely about the RMS error value. The RMS error and RMS uncertainty values for Figure 4.7c are 0.17 pixels/frame and 0.14 pixels/frame and for Figure 4.7d are 0.23 pixels/frame and 0.19 pixels/frame respectively. Thus, the predicted uncertainty using the current framework shows 0.04 pixels underprediction and reasonably predicts the appropriate measurement uncertainty level.

4.4 Conclusion

We proposed a comprehensive framework to predict the uncertainty in the reconstructed 3D particle positions in a volumetric PTV measurement and subsequently propagate the uncertainty in the tracked velocity estimates. The variance estimated from the histogram of the projection error provides the uncertainty bound on the particle image position and contributes to the uncertainty in the mapping function coefficients. The uncertainty on the reconstructed 3D position is obtained as a combination of the particle image position uncertainty and the mapping function coefficient uncertainty. The bias uncertainty on the reconstructed particle positions due to the residual mean disparity is also considered. For the tracked velocity uncertainty, the uncertainty in the reconstructed particle positions is directly combined for each matching particle pair. The covariance between particle position error for paired particles in frame 1 and frame 2 is estimated

using the correlation coefficient of the disparity error values for corresponding particles. Analysis with the synthetic vortex ring images showed good agreement between the RMS of the predicted uncertainties in x_w, y_w, z_w positions and the RMS error. The estimated uncertainty in the displacement field was within 0.04 voxels/frame of the RMS error for both the vortex ring case and the experimental pipe flow case. Overall, the predicted uncertainties are sharply distributed close to the RMS error values and showed strong sensitivity to the variation in RMS error, across a range of seeding densities.

The proposed methodology is applicable, in general, for any given set of 3D reconstructed particle positions, even when they are obtained using advanced tracking methods like STB. However, for STB, the uncertainty in particle trajectory fitting should also be quantified. The current methodology assumes negligible variance in laser pulse separation and thus ignores any temporal uncertainty in the particle tracking. The method also assumes that any covariance in particle image position and calibration coefficient is implicitly taken into account by the uncertainty in the projection error. Another key assumption in this process is the independence between X and Y particle image position estimation errors. These limitations can be further explored and the covariance terms can be quantified in future. The distinction of uncertainty levels for true and false reconstructions should also be further analyzed to explore uncertainty predictions for ghost particle reconstructions. In conclusion, the proposed framework demonstrates accurate uncertainty predictions for both the vortex ring and the pipe flow test cases. These results establish the current methodology as the first successful predictor for uncertainty in a 3D PTV measurement.

Acknowledgements

This work is supported by the National Science Foundation's MRI program grant with award number 1725929.

4.5 References

- [1] H. G. Maas, A. Gruen, and D. Papantoniou, “Particle tracking velocimetry in three-dimensional flows,” *Exp. Fluids*, vol. 15, no. 2, pp. 133–146, Jul. 1993.
- [2] S. J. Baek and S. J. Lee, “A new two-frame particle tracking algorithm using matching possibility,” *Exp. Fluids*, vol. 22, pp. 261–304, 1996.
- [3] K. Ohmi and H.-Y. Li, “Particle-tracking velocimetry with new algorithms,” *Meas. Sci. Technol.*, vol. 11, no. 6, pp. 603–616, May 2000.
- [4] F. Pereira, H. Stüer, E. C. Graff, and M. Gharib, “Two-frame 3D particle tracking,” *Meas. Sci. Technol.*, vol. 17, no. 7, pp. 1680–1692, Jul. 2006.
- [5] S. M. Soloff, R. J. Adrian, and Z. C. Liu, “Distortion compensation for generalized stereoscopic particle image velocimetry,” *Meas. Sci. Technol.*, vol. 8, no. 12, pp. 1441–1454, 1997.
- [6] B. Wieneke, “Volume self-calibration for 3D particle image velocimetry,” *Exp. Fluids*, vol. 45, pp. 549–556, 2008.
- [7] G. E. Elsinga, F. Scarano, B. Wieneke, and B. W. van Oudheusden, “Tomographic particle image velocimetry,” *Exp. Fluids*, vol. 41, no. 6, pp. 933–947, 2006.
- [8] N. D. Cardwell, P. P. Vlachos, and K. A. Thole, “A multi-parametric particle-pairing algorithm for particle tracking in single and multiphase flows,” *Meas. Sci. Technol.*, vol. 22, no. 10, p. 105406, 2011.
- [9] K. Takehara, R. J. Adrian, G. T. Etoh, and K. T. Christensen, “A Kalman tracker for super-resolution PIV,” *Exp. Fluids*, vol. 29, no. 1, pp. S034–S041, 2000.
- [10] A. S. and M. L. Riethmuller, “Extension of PIV to super resolution using PTV,” *Meas. Sci. Technol.*, vol. 12, no. 9, p. 1398, 2001.
- [11] E. A. Cowen, S. G. Monismith, E. A. Cowen, and S. G. Monismith, “A hybrid digital particle tracking velocimetry technique,” *Exp. Fluids*, vol. 22, no. 3, pp. 199–211, Jan. 1997.
- [12] Y.-C. Lei *et al.*, “A vision-based hybrid particle tracking velocimetry (PTV) technique using a modified cascade correlation peak-finding method,” *Exp. Fluids*, vol. 53, no. 5, pp. 1251–1268, Nov. 2012.
- [13] T. Fuchs, R. Hain, and C. J. Kähler, “Double-frame 3D-PTV using a tomographic predictor,” *Exp. Fluids*, vol. 57, no. 11, p. 174, Nov. 2016.

- [14] T. Fuchs, R. Hain, and C. J. Kähler, “Non-iterative double-frame 2D/3D particle tracking velocimetry,” *Exp. Fluids*, vol. 58, no. 9, p. 119, Sep. 2017.
- [15] B. Wieneke, “Iterative reconstruction of volumetric particle distribution,” *Meas. Sci. Technol.*, vol. 24, no. 2, p. 024008, 2013.
- [16] D. Schanz, S. Gesemann, and A. Schröder, “Shake-The-Box: Lagrangian particle tracking at high particle image densities,” *Exp. Fluids*, vol. 57, no. 5, p. 70, May 2016.
- [17] M. Angioletti, E. Nino, and G. Ruocco, “CFD turbulent modelling of jet impingement and its validation by particle image velocimetry and mass transfer measurements,” *Int. J. Therm. Sci.*, vol. 44, no. 4, pp. 349–356, Apr. 2005.
- [18] C. S. Ferreira, G. Van Bussel, and G. Van Kuik, “2D CFD simulation of dynamic stall on a vertical axis wind turbine: Verification and validation with PIV measurements,” in *Collection of Technical Papers - 45th AIAA Aerospace Sciences Meeting*, 2007, vol. 23, pp. 16191–16201.
- [19] M. D. Ford *et al.*, “PIV-measured versus CFD-predicted flow dynamics in anatomically realistic cerebral aneurysm models,” *J. Biomech. Eng.*, vol. 130, no. 2, Apr. 2008.
- [20] P. van Ooij *et al.*, “Complex flow patterns in a real-size intracranial aneurysm phantom: phase contrast MRI compared with particle image velocimetry and computational fluid dynamics,” *NMR Biomed.*, vol. 25, no. 1, pp. 14–26, Jan. 2012.
- [21] M. C. Brindise *et al.*, “Multi-modality cerebral aneurysm haemodynamic analysis: In vivo 4D flow MRI, in vitro volumetric particle velocimetry and in silico computational fluid dynamics,” *J. R. Soc. Interface*, vol. 16, no. 158, 2019.
- [22] J. J. Charonko and P. P. Vlachos, “Estimation of uncertainty bounds for individual particle image velocimetry measurements from cross-correlation peak ratio,” *Meas. Sci. Technol.*, vol. 24, no. 6, p. 065301, Jun. 2013.
- [23] Z. Xue, J. J. Charonko, and P. P. Vlachos, “Particle image velocimetry correlation signal-to-noise ratio metrics and measurement uncertainty quantification,” *Meas. Sci. Technol.*, vol. 25, no. 11, p. 115301, 2014.
- [24] Z. Xue, J. J. Charonko, and P. P. Vlachos, “Particle image pattern mutual information and uncertainty estimation for particle image velocimetry,” *Meas. Sci. Technol.*, vol. 26, no. 7, p. 074001, 2015.

- [25] B. H. Timmins, B. W. Wilson, B. L. Smith, and P. P. Vlachos, “A method for automatic estimation of instantaneous local uncertainty in particle image velocimetry measurements,” *Exp. Fluids*, 2012.
- [26] A. Sciacchitano, B. Wieneke, and F. Scarano, “PIV uncertainty quantification by image matching,” *Meas. Sci. Technol.*, vol. 24, no. 4, p. 045302, Apr. 2013.
- [27] B. Wieneke, “PIV uncertainty quantification from correlation statistics,” *Meas. Sci. Technol.*, vol. 26, no. 7, p. 074002, 2015.
- [28] S. Bhattacharya, J. J. Charonko, and P. P. Vlachos, “Particle image velocimetry (PIV) uncertainty quantification using moment of correlation (MC) plane,” *Meas. Sci. Technol.*, vol. 29, no. 11, p. 115301, 2018.
- [29] A. Sciacchitano *et al.*, “Collaborative framework for PIV uncertainty quantification: comparative assessment of methods,” *Meas. Sci. Technol.*, vol. 26, no. 7, p. 074004, Jul. 2015.
- [30] A. Boomsma, S. Bhattacharya, D. Troolin, S. Pothos, and P. Vlachos, “A comparative experimental evaluation of uncertainty estimation methods for two-component PIV,” *Meas. Sci. Technol.*, vol. 27, no. 9, p. 094006, Sep. 2016.
- [31] S. Bhattacharya, J. J. Charonko, and P. P. Vlachos, “Stereo-particle image velocimetry uncertainty quantification,” *Meas. Sci. Technol.*, vol. 28, no. 1, p. 015301, Jan. 2017.
- [32] A. Sciacchitano, “Uncertainty quantification in particle image velocimetry,” *Meas. Sci. Technol.*, Apr. 2019.
- [33] L. K. Rajendran, S. P. M. Bane, and P. P. Vlachos, “Uncertainty amplification due to density/refractive-index gradients in volumetric PTV and BOS experiments,” *arXiv Prepr. arXiv1910.09379*, 2019.
- [34] J.-Z. Wu, H.-Y. Ma, and M.-D. Zhou, *Vorticity and Vortex Dynamics*. Berlin, Heidelberg: Springer Berlin Heidelberg, 2006.
- [35] D. Schanz, S. Gesemann, A. Schröder, B. Wieneke, and M. Novara, “Non-uniform optical transfer functions in particle imaging: calibration and application to tomographic reconstruction,” *Meas. Sci. Technol.*, vol. 24, no. 2, p. 024009, Feb. 2013.

5. A NEW PARTICLE IMAGE VELOCIMETRY TECHNIQUE FOR TURBOMACHINERY APPLICATIONS

Sayantana Bhattacharya, Reid A Berdanier, Pavlos P Vlachos, Nicole L Key

School of Mechanical Engineering, Purdue University, USA.

This chapter has been previously published in Journal of Turbomachinery, 138(12): 124501.

DOI: <https://doi.org/10.1115/1.4033672>

Abstract

Non-intrusive measurement techniques such as Particle Image Velocimetry (PIV) are growing in both capability and utility for turbomachinery applications. However, the restrictive optical access afforded by multistage research compressors typically requires the use of a periscope probe to introduce the laser sheet for measurements in a rotor passage. This paper demonstrates the capability to perform three-dimensional PIV in a multistage compressor without the need for intrusive optical probes and requiring only line-of-sight optical access. Results collected from the embedded second stage of a three-stage axial compressor highlight the rotor tip leakage flow and PIV measurements are qualitatively compared with high-frequency response piezoresistive pressure measurements to assess tip leakage flow identification.

Nomenclature

c	Chord
d_p	Particle diameter
P	Pressure
St	Stokes number

V_t	Blade tip velocity
W	Relative velocity
ρ_p	Particle density
μ	Air dynamic viscosity

Subscripts:

$o\text{-in,AA}$	Inlet area-averaged total condition
r	Radial
RMS	Root mean square

5.1 Introduction

Measuring the unsteady flow patterns in the rotor blade passage of a multistage compressor is a key step toward understanding the loss-inducing mechanisms in these environments. Traditional probe traversing measurement techniques are often used to study compressor performance, but their intrusive design alters the flow. Thus, a non-intrusive method capable of resolving the flow field is desired. To measure the flow inside the rotor blade passage, non-invasive measurement techniques, such as Laser Doppler Velocimetry (LDV), have been used in the past [1,2]. However, because LDV is a pointwise measurement, it can be a laborious and time-intensive process, and it can be difficult to resolve the spatial characteristics of the flow field.

Since the emergence of Particle Image Velocimetry (PIV), researchers have begun turning to this method to investigate turbomachinery flows. Previous authors have performed PIV measurements in compressor applications [3,4], and other studies have specifically focused on tip leakage flows and measurements in the rotor tip clearance [5-7]. However, in all of these studies, periscopic optical probes were inserted into the flow for light sheet delivery, which renders the measurement invasive and limits the regions of the flow field which can be imaged. The presence of the probe alters the flow, and using a small probe introduces difficulties in achieving precise alignment of the laser beam. Furthermore, seeding can damage the probe or require a shutdown to clean the optics.

These challenges caused by the physical and geometrical constraints imposed by rotating compressor facilities are further amplified when performing stereoscopic or volumetric measurements due to limited viewing angles and reduced overlapping field of view between multiple cameras. Thus, a viable solution is to perform PIV on the embedded stage of a multistage compressor by delivering the laser sheet through the same window used by the cameras to acquire the image. This work demonstrates, for the first time, the capability of performing three-component, three-dimensional PIV in a multistage compressor, without the need for any invasive imaging or light delivery probes inside the compressor.

5.2 Experimental Setup

For the present study, PIV was performed in the second stage rotor passage (Rotor 2) of the three-stage axial compressor at Purdue University. The compressor models the rear stages of a modern

high pressure compressor with engine-representative Mach numbers and Reynolds numbers. For the Rotor 2 conditions presented herein, the relative Mach number is on the order of 0.45 and the relative Reynolds number based on chord is approximately 7.7×10^5 . With a design rotational speed of 5000 rpm, the tip speed is approximately 160 m/s. These PIV measurements were collected as part of an extensive tip clearance sensitivity study, and the data presented herein pertain to a nominal tip clearance height of 2.0 mm, representing 4% rotor tip clearance (based on an annulus height of 50.8 mm). Additional information about the facility is available in Ref. [8].

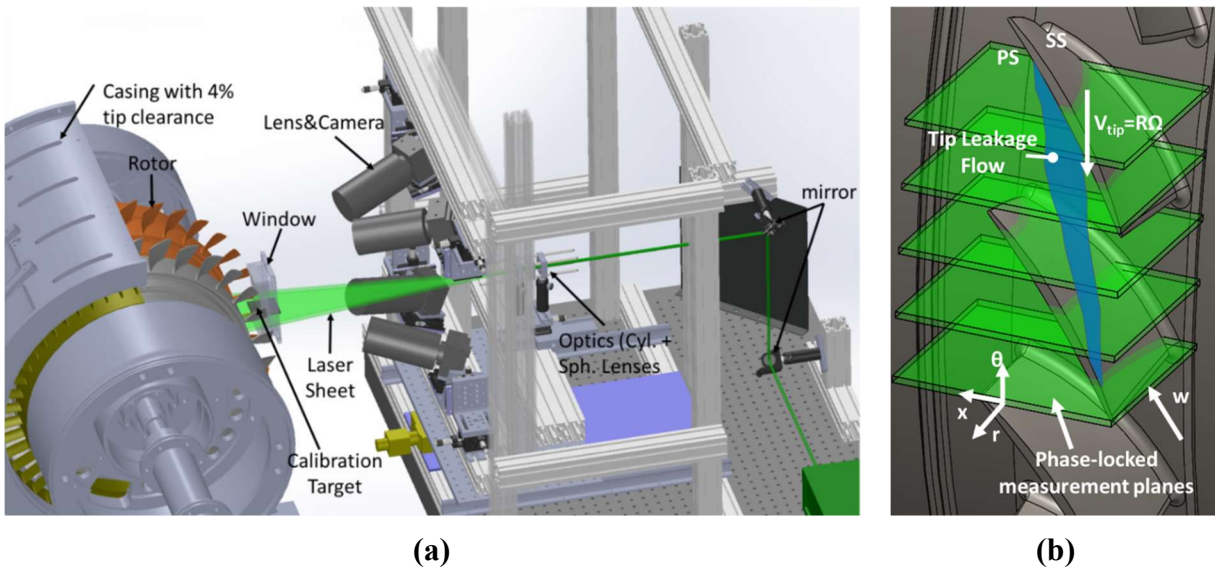


Figure 5.1. (a) Schematic of PIV setup with window, camera and laser positions, (b) Schematic showing flow direction, phase-locked measurement planes covering the blade passage and the expected tip leakage flow.

The experimental setup for the PIV measurements is shown in Figure 5.1(a). Optical access to the compressor was accomplished by a window extending approximately 20% axial chord upstream and downstream of the rotor blade and more than 2 blade pitches in the circumferential direction (69 mm by 127 mm field of view). This window was precision machined to match the curvature of the inner diameter for the compressor. A dual-plane LaVision Type 7 target was mounted between rotor blades during for calibration purposes. This calibration target has dimensions of 58 mm square by 5.8 mm thick, with 1 mm spacing between the two planes and 5 mm spacing between marker dots on each plane. However, the rotor blades blocked portions of the calibration target, effectively reducing the measurement domain to 40 mm in the axial direction. Reflections from the incident laser light were a primary concern for this technique, so an MgF_2

anti-reflective coating was applied to the window to minimize reflections at wavelengths larger than 425 nm.

A Quantel Evergreen Nd-YAG laser (532 nm) was used as the illumination source, and four Imperx CCD cameras were used to acquire the image pairs using a frame-straddling approach. An optimized arrangement of these four cameras, combined with the use of a laser sheet with 4 mm nominal thickness, provided the opportunity to utilize stereo or tomographic reconstruction techniques. Measurements were acquired at 20 phase-locked positions across one rotor blade pitch (based on overlap of the 4 mm laser sheet) to reconstruct a full measurement volume across an entire rotor pitch (Figure 5.1(b)). At the steep viewing angle required for this application, the image was out of focus from 60% span towards the hub and, as a result, meaningful measurements were only obtained between 65% span and the casing wall. The timing for the laser and the cameras was precisely controlled using a pulse generator with a once-per-revolution TTL tachometer signal to phase-lock measurements at different circumferential positions across one blade pitch. Based on the 10.5 Hz laser repetition rate and camera capabilities, one phase-locked position (comprising 1000 image pairs) required approximately five minutes of steady compressor operation.

The anti-reflective coating on the window prevented incident light reflections from this surface, but reflections from the blade surface and hub initially led to saturation of image pixels. To overcome this challenge, fluorescent dye with sufficiently separated absorption and emission wavelengths (Rhodamine B 610 chloride powder) was introduced with the seeding fluid. In addition, lens filters blocking wavelengths below 540 nm were used to filter laser reflections, ultimately yielding recorded images with very low background noise.

Flow seeding was one of the primary challenges for this experiment. The use of fluorescent dye with traditional fog fluid led to significant particle deposition on the window, thereby preventing the use of a fogger for particle seeding. Instead, a TSI 9307-06 six-jet Laskin nozzle was used to atomize the fluorescent dye with propylene glycol as the base fluid. For these tests, the particle generation with the Laskin nozzle was very sensitive to the specific seeding fluid mixture concentration. An ideal mixture for these tests included 1.3% by volume of ethanol added to the glycol to reduce the surface tension of the seed fluid and improve atomization. Ultimately, usable micron-sized tracer particles were successfully attained when introduced through a 12.7 mm tube into the center of the compressor inlet duct at a position 28 axial chords upstream of the IGV leading edge (Figure 5.2).

Seed fluid was injected at a volumetric flow rate of 0.21% with respect to the primary air flow. The compressor performance was assessed with and without seed injection to verify no performance changes were present when particles were introduced. The quality of these particles as flow tracers was evaluated by the Stokes number, St , defined by:

$$St = \frac{\rho_p d_p^2 / (18 \mu)}{c / V_t}, \quad (50)$$

for particle density, ρ_p , particle diameter, d_p , air viscosity, μ , blade chord, c , and blade tip velocity, V_t . Using Eq. (50), the Stokes number for these particles represents 0.0087, which satisfies the $St \ll 1$ condition for particles to behave as flow tracers for PIV.

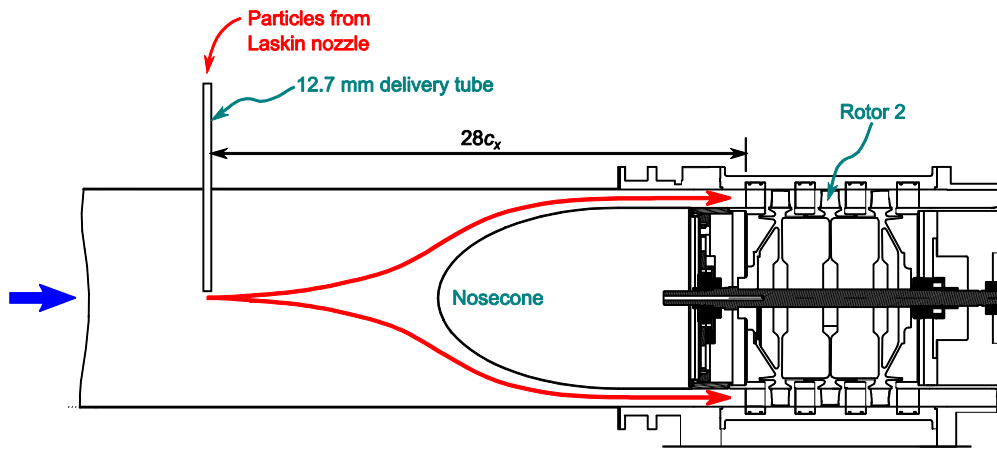


Figure 5.2. Schematic of flow seeding method.

5.3 PIV vector processing

For the present analysis, only the top two camera images were used to reconstruct planar 3-component velocity fields for each phase-locked measurement location. In-house PIV software “Prana”² was used for all calibration, cross-correlation image processing, and three-component velocity reconstruction. A polynomial mapping function [9] was used to map the world coordinate system (x, y, z) in the measurement domain to the image coordinate system (X, Y) for each camera. Due to the very low seeding density, the use of traditional pair-wise image cross-correlation to obtain the planar velocity fields yielded high noise levels and many erroneous measurements. Alternatively, to increase the cross-correlation signal, the sum-of-correlation (or ensemble

² <http://sourceforge.net/projects/qi-tools/>

correlation) approach [10,11] was adopted. Image pairs were cross-correlated, and then the resulting correlation planes were averaged to yield the final estimate. The ensemble correlation delivered high correlation signal-to-noise ratio and robust velocity estimation, reducing the number of outliers from 15% to 4%. The cross correlation was performed using 128-pixel square windows with 50% Gaussian spatial filter [12] and a final pass grid resolution of 8 pixels. Robust Phase Cross-Correlation [13] was used to correlate the image pairs. The planar fields were validated using velocity threshold and Universal Outlier Detection (UOD) to remove erroneous vectors. Then, the estimated planar velocity fields from the two cameras were dewarped onto physical coordinate space and combined with the gradients of the mapping to obtain the three velocity components using a least squares fit [9].

The reconstructed fields were median filtered to remove noisy vectors along the blade edges. The three-component vector fields obtained by generalized stereo reconstruction at each circumferential location were analyzed. The recorded stereo image coordinate system was reoriented and scaled to express the data in terms of the coordinate system defined by axial chord, span, and blade pitch. The blade tip velocity was subtracted from the circumferential velocity component to present the measured absolute frame velocity in terms of the relative rotating reference frame velocity (W).

5.4 Results

This note aims to demonstrate the feasibility of performing non-invasive three-component and three-dimensional measurements inside the embedded stage of a multistage compressor passage. Experiments were carried out at an operating condition near the peak efficiency point at the design speed, and the 20 measurement positions containing the three-component planar velocity fields were combined to reconstruct the volumetric vector field across one blade pitch. The effective domain was then 70% to 96% span, 15% to 90% axial chord, and 100% blade pitch. The velocity field was smoothed with a Gaussian kernel of two standard deviations and a window size of 7x7 grid points to reduce the noise in the flow field. The volume of data was then sliced at constant spanwise locations for interpretation purposes.

The alternating regions of positive and negative radial velocity in Figure 5.3 are indicative of the tip leakage flow and what has been identified as the tip leakage vortex [14]. Although the measurements were collected across one complete blade pitch, the domain was plotted with

periodic repetition in the pitchwise direction for more intuitive visualization. To further assess the viability of this PIV technique, the leakage flow trajectory identified in Figure 5.3 is qualitatively compared with a separate experimental method for tracking the tip leakage flow in Figure 5.4.

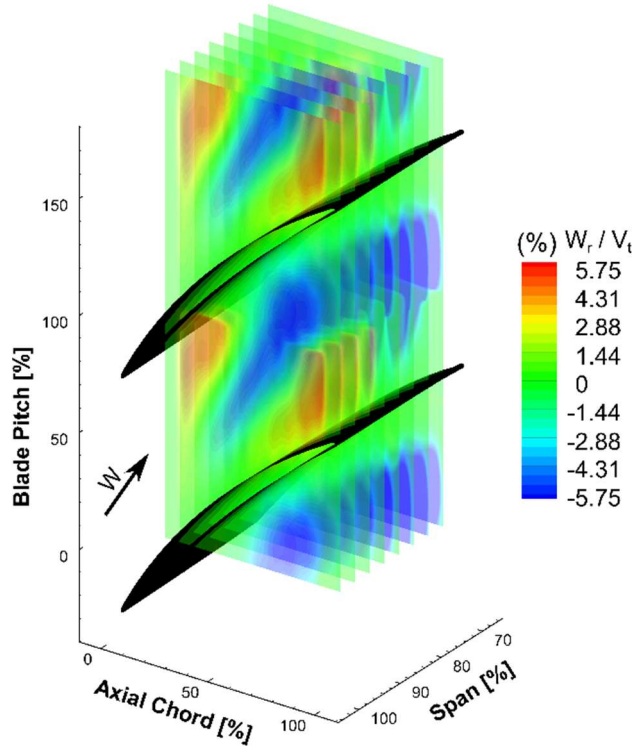


Figure 5.3. Volume slices of normalized radial velocity at fixed spanwise locations for stereo reconstructed velocity field.

In Figure 5.4(a), a slice of PIV data near the wall is presented as contours of normalized radial velocity with vectors shown as projections of the three-dimensional relative velocity vector onto the $r - \theta$ plane. For comparison, Figure 5.4(b) shows contours of static pressure unsteadiness measured using high-frequency response piezoresistive pressure transducers in a flush-mounted configuration over the rotors, as described by Berdanier and Key [15]. Using this method, the tip leakage flow trajectory can be tracked by the locus of peak unsteadiness points across the passage emanating from near the leading edge of the blade. In Figure 5.4(c), the results from both techniques are superimposed with colored contours of radial velocity from PIV and line contours from the static pressure unsteadiness. In this combined figure, the region of high unsteadiness identified in Figure 5.4(b) is bounded by the regions of negative and positive radial velocity from the PIV results in Figure 5.4(a). Based on this comparison, the trajectory angle of a line bounding

the tip leakage flow identified by either technique (in this case, both are non-intrusive measurements) is similar to within one degree across the passage.

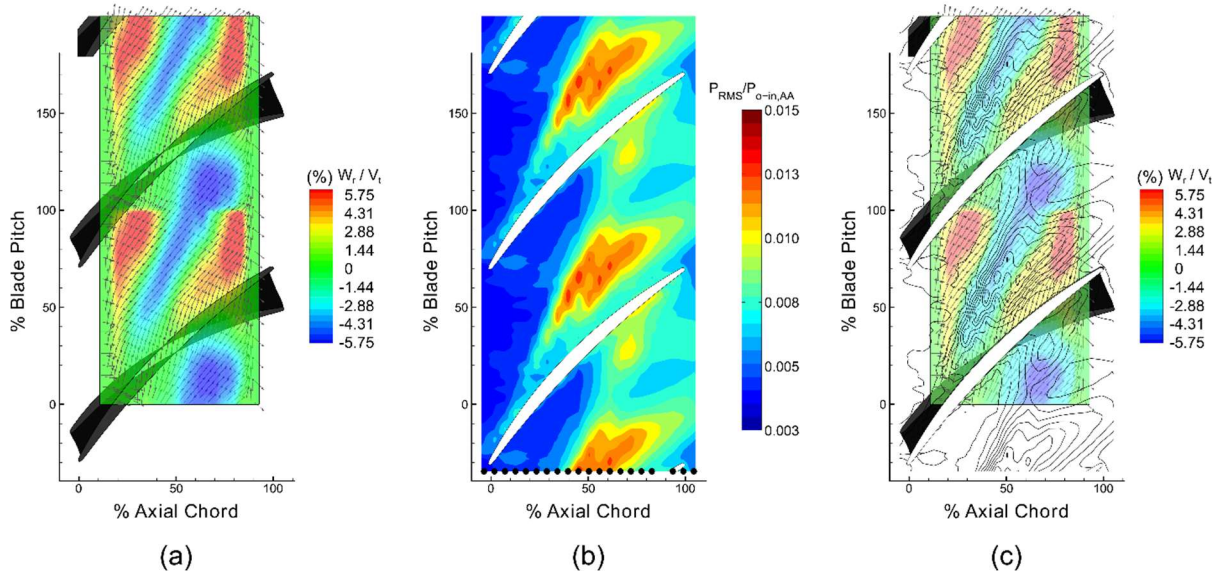


Figure 5.4. Comparison of PIV results with over-rotor static pressures. Flow is from left to right. (a) Contours of normalized radial velocity near the wall; (b) Over-rotor static pressure contours; (c) Both methods superimposed with PIV normalized radial velocities as colored contours and static pressure contours represented as lines.

5.5 Conclusion

These results show three-dimensional PIV measurements in a multistage compressor are not only possible, but a viable option, even with one simple optical access window and without the need for inserting an optical probe into the flow field. The development of this technique unlocks previously unknown possibilities for future implementation of optical measurements in turbomachinery applications which traditionally offer poor accessibility.

Several important steps were required for implementation of this technique, including: anti-reflective coating on the window, fluorescent dye particles, and fluorescent lens filters on the cameras. Challenges with seeding density were resolved through the use of an ensemble correlation technique in the image processing steps, although future variations of particle generation strategies and seeding locations are expected to yield improved results.

Slices of normalized radial velocity at fixed spanwise positions highlighted the development of the tip leakage flow across the rotor passage, and a qualitative comparison of PIV measurements near the wall showed exceptional similarity to a more mature tip leakage flow

tracking technique. Data collected from the entire four-camera system are under current refinement with the intent to obtain full tomographic PIV velocity fields using this method.

Acknowledgements

Technical assistance provided by Dr. Natalie Smith is gratefully acknowledged. This material is based upon work supported by NASA under the ROA-2010 NRA of the Subsonic Fixed Wing project, with Technical Monitor Dr. Mark Celestina, and in part by the National Science Foundation Graduate Research Fellowship Program under Grant No. DGE-1333468. National Science Foundation Instrument Development for Biological Research Grant No. 1152304 provided additional partial support. The authors would also like to thank Rolls-Royce for the permission to publish this work.

5.6 References

- [1] Ma, H., Jiang, H., and Zhang, Q., 2001, “Three-Dimensional Unsteady Flow Field Due to IGV-Rotor Interaction in the Tip Region of an Axial Compressor Rotor Passage,” ASME Paper No. 2001-GT-0296.doi: 10.1115/2001-GT-0296
- [2] Michon, G.-J., Miton. H., and Ouayhaya, N., 2005, “Unsteady Off-Design Velocity and Reynolds Stresses in an Axial Compressor,” *Journal of Propulsion and Power*, **21**(6), pp. 961-972.doi: 10.2514/1.10326
- [3] Balzani, N., Scarano, F., Riethmuller, M.L., and Breugelmans, F.A.E., 2000 “Experimental Investigation of the Blade-to-Blade Flow in a Compressor Rotor by Digital Particle Image Velocimetry,” *Journal of Turbomachinery*, **122**(4), pp. 743-750.doi: 10.1115/1.1311283
- [4] Sanders, A.J., Papalia, J., and Fleeter, S., 2001, “Multi-Blade Row Interactions in a Transonic Axial Compressor: Part I—Stator Particle Image Velocimetry (PIV) Investigation,” *Journal of Turbomachinery*, **124**(1), pp. 10-18.doi: 10.1115/1.1411973
- [5] Wernet, M.P., John, W.T., Prahst, P.S., and Strazisar, A.J., 2001, “Characterization of the tip clearance flow in an axial compressor using digital PIV,” AIAA Paper No. 2001-00697. doi: 10.2514/6.2001-697
- [6] Wernet, M.P., Van Zante, D., Strazisar, T.J., John, W.T., and Prahst, P.S., 2005, “Characterization of the tip clearance flow in an axial compressor using 3-D digital PIV,” *Experiments in Fluids*, **39**(4), pp. 743-753.doi: 10.1007/s00348-005-0007-7
- [7] Voges, M., Willert C.E., Mönig, R., Müller, M.W., and Schiffer, H.P., 2012, “The challenge of stereo PIV measurements in the tip gap of a transonic compressor rotor with casing treatment,” *Experiments in Fluids*, **52**(3), pp. 581-590.doi: 10.1007/s00348-011-1061-y
- [8] Berdanier, R.A. and Key, N.L., 2015, “The Effects of Tip Leakage Flow on the Performance of Multistage Compressors Used in Small Core Engine Applications,” *Journal of Engineering for Gas Turbines and Power*, **138**(5), 052605 (10 pages).doi: 10.1115/1.4031625
- [9] Soloff, S.M., Adrian, R., and Liu, Z., 1997, “Distortion compensation for generalized stereoscopic particle image velocimetry,” *Measurement Science and Technology*, **8**, pp. 1441-1454.doi: 10.1088/0957-0233/8/12/008

- [10] Santiago, J.G., Wereley, S.T., Meinhart, C.D., Beebe, D.J., and Adrian, R.J., 1998, “A particle image velocimetry system for microfluidics,” *Experiments in Fluids*, **25**(4), pp. 316-319.doi: 10.1007/s003480050235
- [11] Westerweel, J., Geelhoed, P.F., and Lindken, R., 2004, “Single-pixel resolution ensemble correlation for micro-PIV applications,” *Experiments in Fluids*, **37**(3), pp. 375-384. doi: 10.1007/s00348-004-0826-y
- [12] Eckstein, A. and Vlachos, P.P., 2009, “Assessment of advanced windowing techniques for digital particle image velocimetry (DPIV),” *Measurement Science and Technology*, **20**, 075402.doi: 10.1088/0957-0233/20/7/075402
- [13] Eckstein, A. and Vlachos, P.P., 2009, “Digital particle image velocimetry (DPIV) robust phase correlation,” *Measurement Science and Technology*, **20**, 055401.doi: 10.1088/0957-0233/20/5/055401
- [14] Storer, J.A. and Cumpsty, N.A., 1991, “Tip Leakage Flow in Axial Compressors,” *Journal of Turbomachinery*, **113**(2), pp. 252-259.doi: 10.1115/1.2929095
- [15] Berdanier, R.A. and Key, N.L., in press, “Experimental Characterization of Tip Leakage Flow Trajectories in a Multistage Compressor,” *Journal of Propulsion and Power*.

6. CONCLUSION

A detailed framework for uncertainty estimation in planar PIV, stereo-PIV and 3D PTV has been formulated in this dissertation. The principle idea behind the dissertation is justified by the practical need of uncertainty bounds for any PIV based design study, as well as the contemporary efforts to quantify the measurement uncertainty in the PIV community. The comparative analysis in the first chapter highlights the need for further development of new planar PIV uncertainty quantification methods. This work not only provides a reference for the existing methods but also a benchmark dataset for comparing the new developing methods. The second chapter propose a direct uncertainty estimation framework from the PIV correlation plane, namely the Moment of Correlation (MC). As a part of the framework, the PDF of displacement within an interrogation window is extracted using the phase of the correlation plane. This methodology predicts the correct uncertainty level and coverage for five different test flow cases, especially for a processing with higher interrogation window size. However, a bias error up to 0.02 pixels is observed for smaller windows due to limited number of particles contributing the correlation peak and thus reaching the resolution limit in estimating the standard deviation of the PDF. In general, the different 2D PIV uncertainty estimation methods find the uncertainty values utilizing the same information but through different modeling which leads to slightly different response for each method and overprediction or underprediction of RMS error. Hence, as a part of future work, a meta-uncertainty model is being developed incorporating the variance in the estimated uncertainty models and combining the different predictions to yield a more robust uncertainty estimate.

For stereo-PIV and for 3D PTV, the measurement chain requires quantifying the uncertainty in the calibration mapping function coefficients. For stereo-PIV, the uncertainty in the calibration mapping function relates to the uncertainty in the angles, which is combined with the individual camera 2D PIV uncertainty estimates through the propagation equation. For 3D PTV, the uncertainty in the mapping function and the uncertainty in the projected particle image location directly influence the reconstructed 3D position uncertainty and in turn the uncertainty in the tracked velocity estimate. The current results show a successful prediction of velocity uncertainty in each case. The contribution of the calibration uncertainty has been observed to be negligible for a well-designed stereo-PIV experiment. However, calibration uncertainty for a more challenging scenario, for example in presence of density gradients is yet to be analyzed. On the other hand, for

3D PTV, the contribution of “ghost” particles in 3D tracking uncertainty needs to be explored. The current model predicts the uncertainty for the matched particles between frames. However, for an experimental case, without the knowledge of true pairing, the false reconstructions contribute to the tracked velocity uncertainty. This aspect needs to be further explored for both pairwise tracking as well as for temporal particle trajectory predictions in methods like STB.

Finally, as a natural extension of the knowledge presented in this dissertation, the uncertainty for a 3D PIV measurement should be quantified and is considered as a part of the future work. The uncertainty in the calibration process has already been quantified. For the intensity-based MART reconstruction, an uncertainty model needs to be developed to estimate the uncertainty in the reconstructed voxel intensities. For the 3D PIV correlation step, the direct methods, such as IM, CS and MC can be directly extended to the volumetric correlation, however, the models need to be extensively tested for different cases to determine its performance and applicability.